MODULATION OF VERY LOW FREQUENCY WHISTLER WAVES BY ULTRA LOW FREQUENCY WAVES

by

Zhiyang Xia

APPROVED BY SUPERVISORY COMMITTEE:

Lunjin Chen, Chair

Fabiano Rodrigues

Fan Zhang

Phillip Anderson

Roderick Heelis

Dedicated to my parents.

MODULATION OF VERY LOW FREQUENCY WHISTLER WAVES BY ULTRA LOW FREQUENCY WAVES

by

ZHIYANG XIA, BS, MS

DISSERTATION

Presented to the Faculty of

The University of Texas at Dallas

in Partial Fulfillment

of the Requirements

for the Degree of

DOCTOR OF PHILOSOPHY IN

PHYSICS

THE UNIVERSITY OF TEXAS AT DALLAS

August 2019

ACKNOWLEDGMENTS

This dissertation is completed with the guidance, assistance, and support of many outstanding faculties, scientists, students and staff members. I am pleased to express my gratitude to all of them:

First, I want to appreciate my supervisor, Professor Lunjin Chen, for his teaching of space physics knowledge, guidance on my research work and other help in my daily life. He is responsible and patient with me, and he always excites my interest in space sciences and helps me solve problems in my research.

I also appreciate the excellent faculty members in our department, including Professor Roderick Heelis, Professor Phillip Anderson, Professor Fabiano Rodrigues, Professor David Lary, Professor Fan Zhang, etc., for their great teaching in classes and assistance on my research work. The staff members in our department also helped me a lot with my academic affairs. I want to thank all of them, especially Ms. Barbara Burbey, Ms. Julie Welch and Ms. Amanda Hunter.

This dissertation also benefits a lot from collaborations with colleagues outside our department. Thanks to Professor Anthony Arthur Chan for his contribution to the eigenmode analysis of field line resonance, to Professor Wen Li for providing the THEMIS data of chorus modulation events, to Dr. Zeren Zhima for providing the data of DEMETER satellite, to Dr. Vania Jordanova for the usage of RAM-SCB code, to Dr. Ondrej Santolík for the waveform analysis of DEMETER data.

I have learned a lot from communicating with colleagues in my group, including Xu Liu, Liheng Zheng, Hui Zhu, Zhaoguo He, Si Liu, Xiang Xu, Zhenxia Zhang, Ying Xiong, Armando Maldonado, Wenyao Gu, Jicheng Sun and Yangguang Ke. Thanks for their discussion and help.

Finally, my family and friends, such as Xun Liu, Xiaoyuan Liu, and Daji Wu, have supported me a lot and helped me overcome many difficulties in my life. I am very pleased and fortunate to have met and associated with them.

June 2019

MODULATION OF VERY LOW FREQUENCY WHISTLER WAVES BY ULTRA LOW FREQUENCY WAVES

Zhiyang Xia, PhD
The University of Texas at Dallas, 2019

Supervising Professor: Lunjin Chen, Chair

This dissertation focuses on the study of the modulation of very low frequency (VLF) whistler mode waves in the Earth's magnetosphere by ultra low frequency (ULF) waves. First, I provide an in-situ observation of chorus wave modulated by ULF waves deep in the inner magnetosphere. The observed ULF wave can modulate the distribution of both protons and electrons and amplify the intensity of chorus waves. Then I build a two-dimensional self-consistent magnetic field (SCB) model to analyze the eigenmode of ULF field line resonance (FLR) with the effect of the anisotropic ring current pressure included. The results show that the eigenfrequency is reduced at the negative radial pressure gradient while increases at the positive pressure gradient. The compressional component of FLR magnetic field perturbation can be found in both the positive and negative gradient regions of the pressure and enhanced by larger plasma β and smaller anisotropy. Using about 2 years' observations of three THEMIS satellites and over 5.5 years of observations of two Van Allen Probes satellites, I perform a statistical study of the chorus wave modulation events. The results indicate that in most of the modulation events, the intensity of chorus wave correlates to the background magnetic field negatively and plasma density positively. The intensity of chorus wave strongly depends on the amplitude of the background magnetic field perturbation but weakly depends on the amplitude of plasma density perturbation.

Besides the work on VLF whistler mode waves modulated by ULF waves, I also perform two other relevant studies. The first one is using the two-dimensional self-consistent magnetic field (SCB) model to study the effects of localized thermal pressure on the magnetic field configuration and the formation of magnetic dip structure. The modeling results demonstrate that the magnetic perturbation increases with increasing plasma β and decreasing width of pressure distribution. The formation of magnetic dip requires a critical β value that increases with increasing width of pressure distribution and decreasing L shell. The other study is using the observations of DEMETER satellite to investigate propagation characteristics of low altitude ionospheric hiss. The ionospheric hiss can propagate from the high latitude regions to the equator within a waveguide near the region of cutoff frequency and plasma density peak, which results in the narrow frequency banded spectrum of ionospheric hiss waves with the central frequency around the local proton cyclotron frequency. The power of ionospheric hiss is stronger on the dayside than the nightside, under higher geomagnetic activity, in local summer and confined near the region where the local proton cyclotron frequency is equal to the wave frequency.

TABLE OF CONTENTS

LIST OF FIGURES

CHAPTER 1

INTRODUCTION

1.1 Earth's Magnetosphere

The solar system comprises the Sun, which is the center of the system, and eight large planets, including the Earth. The space between the sun and other parts within the solar system is called the interplanetary space. The interplanetary space is not vacuum; instead, there exists ionized gas consisting of positive and negative charged particles in the interplanetary space with low particle number density ($\sim$5 particles per cubic centimeter around the Earth). This ionized gas is also known as plasma, which is usually in quasi-neutral charge state. Besides the low density background plasma, there are also some bulks of higher density plasma traveling within the interplanetary space. The Sun continuously blows plasma at a supersonic speed (known as solar wind) to the interplanetary space and influences the other planets.

The Earth's magnetic field, also called the geomagnetic field, can interact with the solar wind and prevent the solar wind from reaching the surface of the Earth. As a result, the shape of the geomagnetic field changes and a cavity structure named magnetosphere is formed. The Earth's magnetosphere is a huge cavity surrounding the Earth and dominated by the Earth's magnetic field. Its outer boundary is called the magnetopause. Above the magnetopause, a bow shock is formed because of the supersonic solar wind. Between the bow shock and the magnetopause is the magnetosheath, a region where the solar wind flow becomes subsonic and the plasma is heated. Most of the plasma comes from the solar wind and the magnitude of the magnetic field varies erratically.

The detailed structures of the magnetosphere are shown in Figure 1.1. At dayside, the magnetosphere is compressed by the solar wind, while at nightside, the magnetosphere is stretched and appears as a long tube with a length of about 100-200 R_E (R_E is the radius

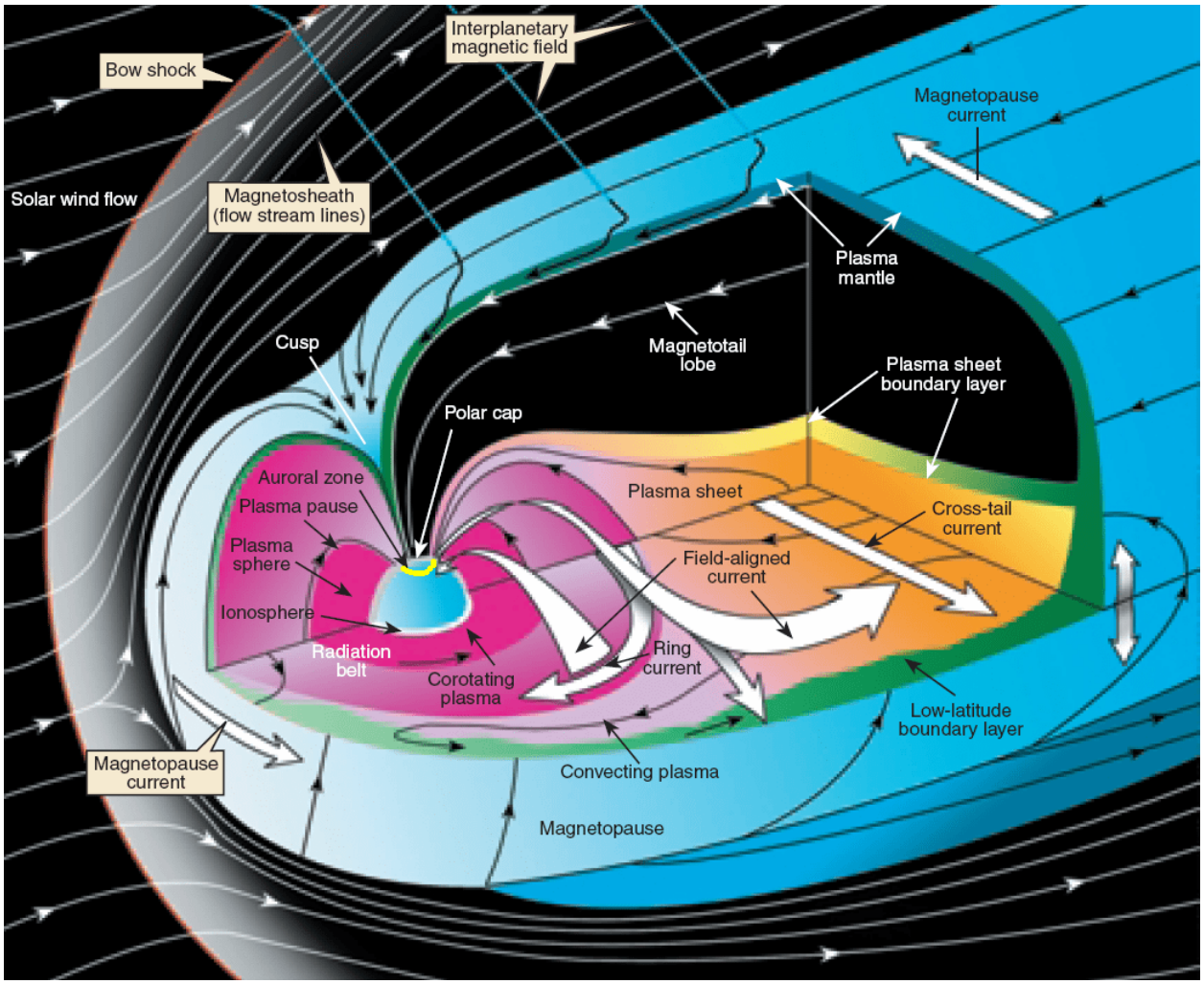

Figure 1.1. The illustration of the Earth's magnetosphere's structures [C. Brandt et al., 2005].

of the Earth), which is called the Earth's magnetotail. Near the magnetic equatorial plane in the Earth's magnetotail is the plasma sheet, a flat region with hot plasma extending from 5 R_E to about 45 R_E. The plasma in the plasma sheet is a mixture of the ionospheric and solar wind plasma with a high β value of about 5-10 (β is the ratio between the plasma thermal pressure and magnetic pressure). The electron number density in the plasma sheet is about $0.1 - 1\ cm^{-3}$ and the energy of ions is typically of a few keV. The region between the magnetopause and the plasma sheet in the magnetotail are the tail lobes with a very low β value. Totally, the magnetotail is a region for the energy storage of the magnetosphere and provides energy and plasma sources for the inner magnetosphere.

The region within 8 R_E from the Earth is called the inner magnetosphere, where the magnetic field is nearly dipolar. The inner magnetosphere includes three particle populations: plasmasphere, radiation belts and ring current. The plasmasphere typically extends from 2 to 8 R_E and looks like a torus. The plasmaspheric plasma is cold ($\sim$1 eV) and dense ($10 - 10^3\ cm^{-3}$). The outer boundary of the plasmasphere is called the plasmapause and is correlated with the inner boundary of the outer radiation belt [Goldstein et al., 2005; Li et al., 2006; Pierrard and Benck, 2012]. The radiation belts are regions of relativistic electrons (>100 keV) trapped by the Earth's magnetic field and orbiting surrounding the Earth. The radiation belts include two zones: the inner belt and the outer belt. The inner belt locates at about 1.5 -2 R_E and contains high concentrations of electrons of hundreds of keV energy and energetic protons with energies over 100 MeV, while the outer belt locates at 3-6 R_E and consists mainly of relativistic electrons (0.1 to 10 MeV). Near the geomagnetic equator between 2 and 7 R_E, the ring current circulates around the Earth, carrying westward current. The ring current is caused by the longitudinal drift motion of charged particles (eastward for electrons and westward for ions) and its energy density is mainly carried by the ions over the 10s-100s keV energy. The ring current can produce a southward magnetic field at the equator near the Earth's surface, leading to magnetic field depression.

1.2 Dynamics in the Magnetosphere

The dynamics in the magnetosphere are directly controlled by the solar wind which carries with a highly varying interplanetary magnetic field (IMF). Near the sub-solar point of the magnetosphere (the intersection point between the Sun-Earth line and the magnetopause), if the direction of the magnetic field in the solar wind is southward(opposite to the direction of Earth's magnetic field), the magnetic reconnection process occurs. The reconnection can change the topology of field lines, where a portion of the Earth's closed field lines connect to the field lines in the solar wind and become open field lines. The open magnetic field lines together with the plasma frozen within are swept away by the solar wind and move from the dayside into the magnetotail. In the magnetotail, another reconnection occurs and the open magnetic field lines become closed again and move back to the dayside. This process is called Dungey circle [Dungey, 1961] and allows the particles in the solar wind penetrate into the magnetosphere, which is a replenishment of particles in the magnetosphere balancing with the particle loss due to the precipitation into the ionosphere.

Magnetospheric activity, such as geomagnetic storms and magnetospheric substorms, can occur under a strong solar wind driver. The geomagnetic storms usually take place under a long time period of high solar wind speed and southward interplanetary magnetic field (IMF), which is an effective condition for magnetic reconnection as well as the accompanying energy transfer from the solar wind into the Earth's magnetosphere. Geomagnetic storms usually last from several hours to days and are divided into three phases (Figure 1.2): the initial phase, the main phase and the recovery phase. Geomagnetic storms can result in intense current in the magnetosphere, particle precipitation from the magnetosphere into the ionosphere, heating of the ionosphere and the thermosphere. The enhanced ring current can decrease the horizontal magnetic field at the Earth's surface due to its diamagnetic effect. Thus the Dst (disturbed storm time) index, describing the magnetic perturbation near the

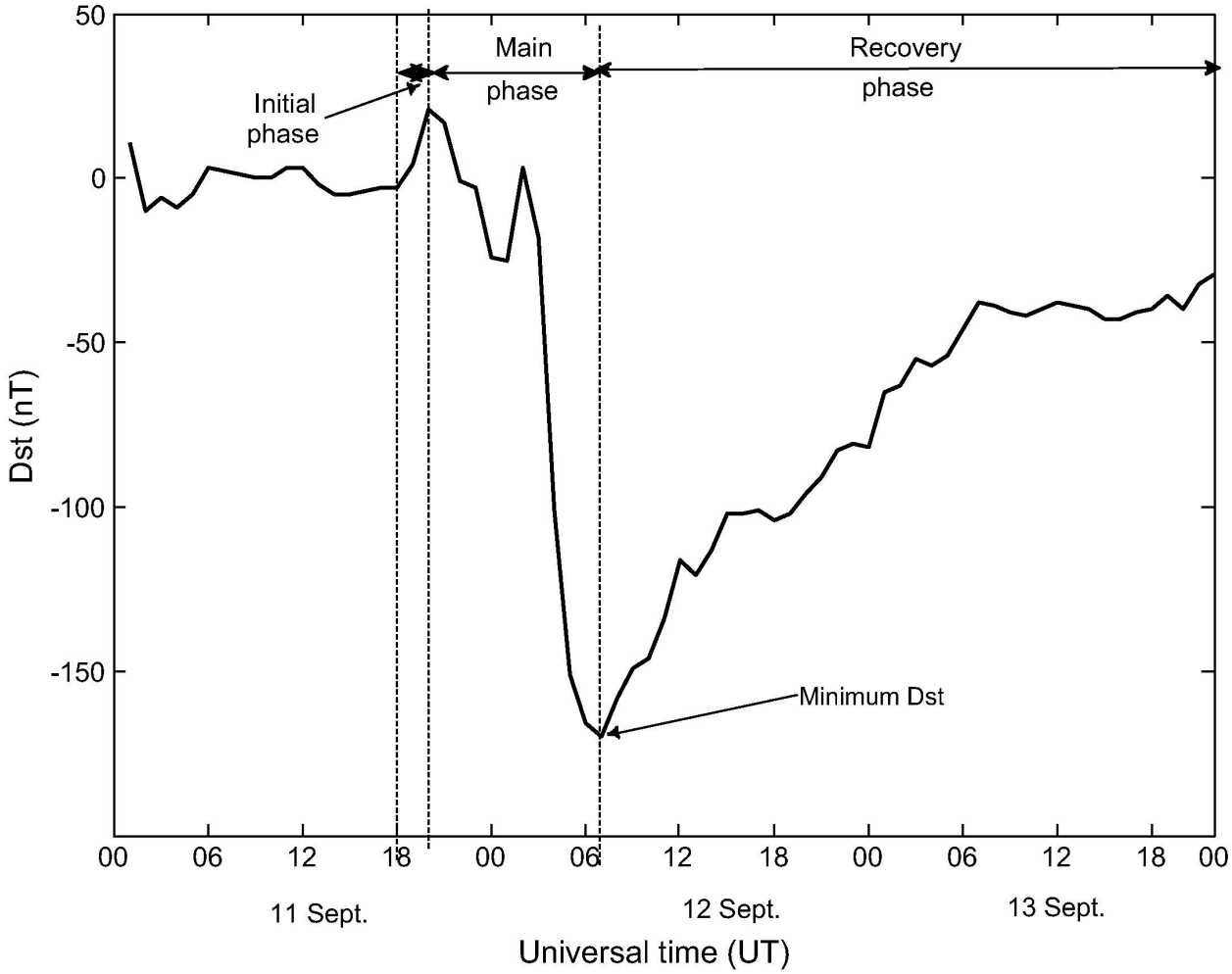

Figure 1.2. A geomagnetic storm and its three phases identified by Dst index [Okpala and Ogbonna, 2018].

equator at the Earth's surface, is used to identify and characterize the geomagnetic storms (Figure 1.2).

The magnetospheric substorm is another important magnetospheric dynamic that usually corresponds to geomagnetic storms but is not a "smaller storm" or a part of the storm. The duration of a substorm is generally a few hours including three distinct phases (Figure 1.3): the growth phase, the expansion phase and the recovery phase. The growth phase usually starts after a southward turning of the interplanetary magnetic field, which enhances

the dayside magnetic reconnection and transfers large amounts of magnetic flux together with plasma to the magnetotail. Energy accumulates in the magnetotail to a substantial quantity and then is quickly released and deposited into the inner magnetosphere, which triggers the expansion phase [Rostoker et al., 1980; Rostoker, 1996]. After the expansion phase, the magnetosphere returns to the previous steady state in a duration of about 1 hour which is called the recovery phase [Akasofu, 1964]. During the expansion phase, there exist multiple phenomena such as particle energization in the plasma sheet, particle injection at geostationary orbit, enhanced particle precipitation and increased corresponding auroral luminosity. The particle injection is caused by the earthward motion of magnetic field lines dragging plasma from the geomagnetotail into the inner magnetosphere and is usually observed as abrupt enhancements of particle fluxes with energies from tens to hundreds of keV [Parks et al., 1980; Sandholt and Farrugia, 2001]. The particle injection can cause perturbations of the magnetic field with a duration of 10s of minutes to several hours due to the diamagnetic effect. Also, ULF (ultra low frequency) magnetic field perturbations with short duration (about 10s of seconds) can be excited during the expansion phase. The substorm level is usually characterized by the AU, AL and AE indices (Figure 1.3) which are related to the magnetic activity in the auroral zone produced by the enhanced ionospheric currents flowing below and within the auroral oval.

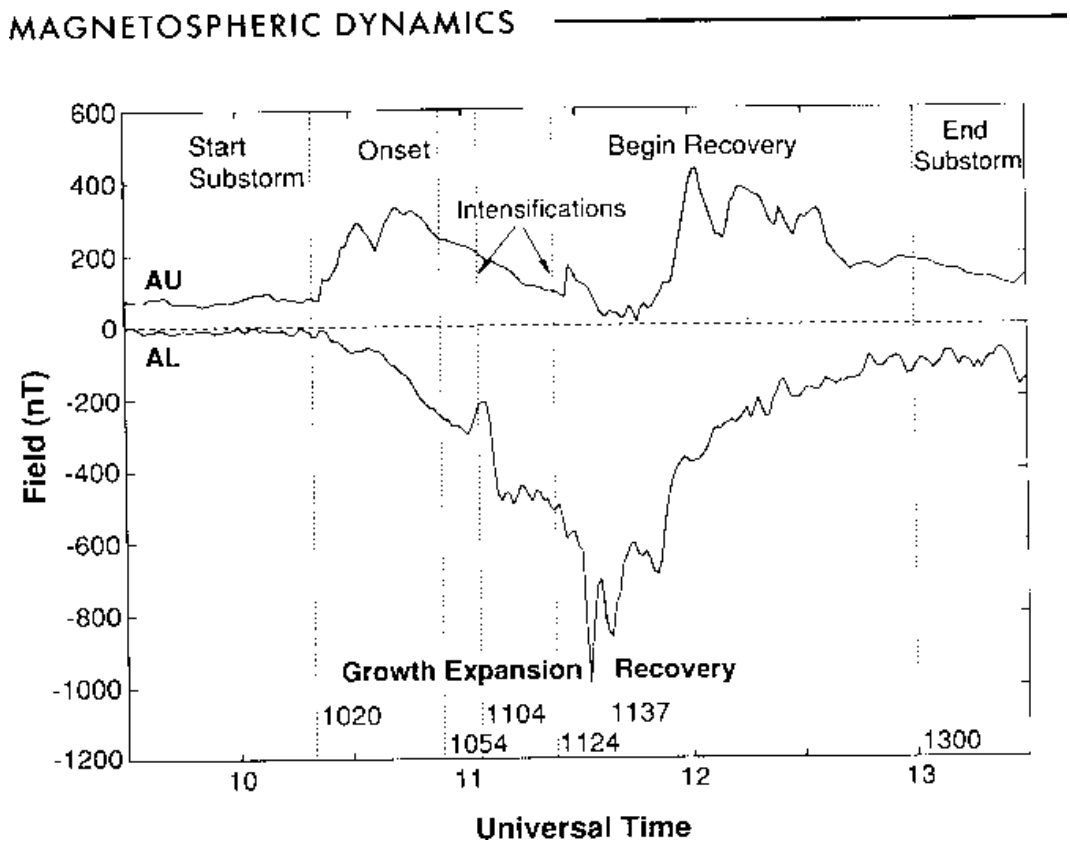

Figure 1.3. Definitions of the three phases of a magnetic substorm in terms of two auroral activity indices AU and AL [McPherron, R. L., 1995].

1.3 Particle Motions in the Magnetosphere

The motion of charged particles without collision in given electric field E and magnetic field $\mathbf{B}$ can be described by the relativistic momentum equatons:

$$\mathbf{p} = \gamma m \mathbf{v}, \tag{1.1}$$

$$\frac{d\mathbf{p}}{dt} = q(\mathbf{E} + \mathbf{v} \times \mathbf{B}), \tag{1.2}$$

where $\mathbf{p}$ is the particle's momentum, $\mathbf{v}$ is the particle's velocity, m is the rest mass of the particle, q is the particle's charge and $\gamma = 1/\sqrt{1 - v^2/c^2}$ is the Lorentz factor (c is the

speed of light in vacuum). Assuming that the radius of particles' gyro motion r_g is much smaller than the spatial scale of magnetic field $B/|\nabla B|$, the motion of charged particle can be decomposed into a fast gyro motion around the guiding center and a slow motion of the guiding center. This assumption is true for most particles in the Earth's magnetosphere with energy lower than 100 MeV [Young et al., 2002; Selesnick et al., 2007]. For the fast gyro motion, the radius r_g and period τ_g are:

$$r_g = \frac{p \sin \alpha}{|q|B}, \tag{1.3}$$

$$\tau_g = \frac{2\pi\gamma m}{|q|B}, \tag{1.4}$$

where α is the pitch angle (the angle between $\mathbf{v}$ and $\mathbf{B}$).

The motion of the guiding center can be described as [Northrop, 1963]:

$$\mathbf{V}_{GC} = \frac{\mathbf{E} \times \mathbf{B}}{B^2} + \frac{\gamma m v_\perp^2}{2qB^2}(\mathbf{b} \times \nabla B) + \frac{\gamma m v_\parallel^2}{qB^2}(\mathbf{B} \times (\mathbf{b} \cdot \nabla)\mathbf{b}) + \mathbf{v}_\parallel, \tag{1.5}$$

where $v_\perp$ and $v_\parallel$ are the speed components perpendicular and parallel to the ambient magnetic field, respectively, and $\mathbf{b} = \mathbf{B}/B$ is the unit vector of the magnetic field. At the right-hand side of Equation (1.5), the first three terms are the electric drift motion, magnetic gradient drift motion and magnetic curvature drift motion respectively, which are all perpendicular to the background magnetic field. The last term is the motion parallel to the background magnetic field and the parallel velocity is governed by:

$$\frac{d\mathbf{v}_\parallel}{dt} = -\frac{v_\perp^2}{2B^2}(\nabla B \cdot \mathbf{B}) \tag{1.6}$$

The right-hand side term of Equation (1.6) is known as "mirror force", which can accelerate the particle in the direction opposite to the gradient of the magnetic field. Along a magnetic field line with stronger magnetic field strength at the two ends (for example, the Earth's magnetic field), the particles will be reflected at two mirror points as a result of the "mirror force". Thus a periodic bounce motion of particles between the two mirror points follows.

However, for the Earth's magnetic field, if the mirror point is too close to the Earth's surface (i.e. altitude less than 100 km), the charged particle may penetrate into the atmosphere and collide with dense atmospheric particles (neutrals and ions), which makes the charged particle quickly absorbed by the atmosphere and fail to bounce back to the magnetosphere. The altitude of the mirror point decreases as the particle's equatorial pitch angle decreases, thus particles with small enough equatorial pitch angles will be lost to the atmosphere and the range of these small pitch angles is termed as the "loss cone".

To sum up, the motion of charged particles trapped in the magnetosphere includes three kinds of quasi-periodic motions with distinct time periods: the gyro motion around the guiding center on the magnetic field line with smallest period, the bounce motion along magnetic field line and the drift motion around the Earth with largest period, which are shown by Figure 1.4. Each of the three kinds of motion is also associated with one corresponding adiabatic invariant that is conserved if the change of electric and magnetic fields can be ignored over the period of the corresponding motion. The first adiabatic invariant corresponding to the gyro motion is:

$$J_1 = \frac{p_\perp^2}{2qB}. \tag{1.7}$$

The second adiabatic invariant corresponding to the bounce motion is:

$$J_2 = 2p \int_{s_{m1}}^{s_{m2}} \sqrt{1 - B(s)/B_m} ds, \tag{1.8}$$

where s_{m1} and s_{m2} are the two mirror points, $B_m = p^2 B/p_\perp^2$ is the magnetic field strength at the mirror point, ds is an element of distance along magnetic field line. The third adiabatic invariant corresponding to the drift motion is:

$$J_3 = q \oint \mathbf{B} \cdot d\mathbf{S}, \tag{1.9}$$

where $d\mathbf{S}$ is an element of the surface enclosed by the equatorial drift shell.

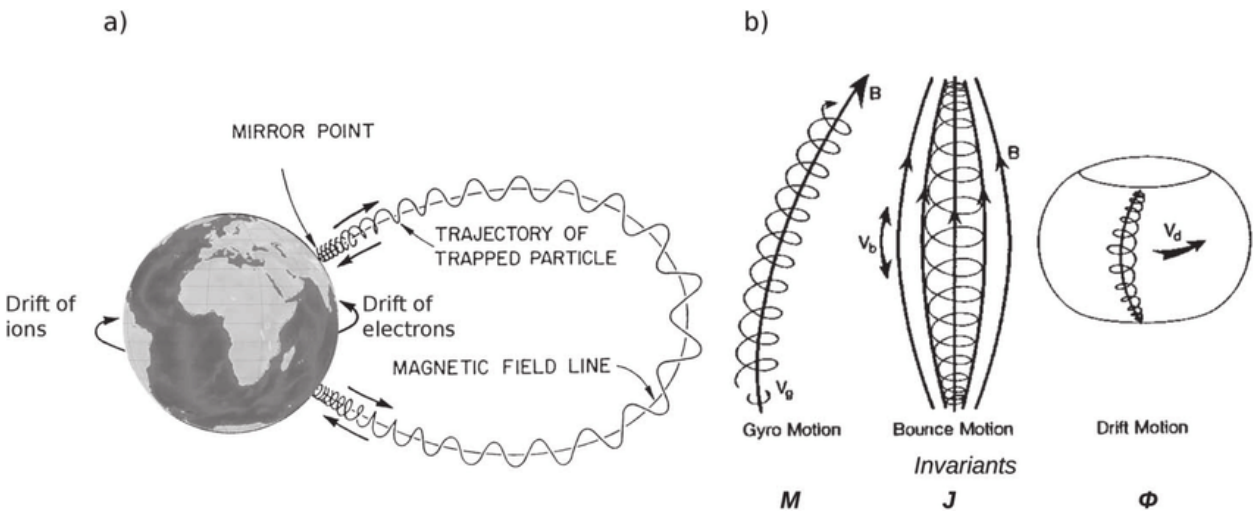

Figure 1.4. Schematic representation of the three motions of a magnetically trapped charged particle in the magnetosphere [Regi, 2016].

1.4 Very Low Frequency (VLF) Whistler Mode Waves in the Magnetosphere

In the Earth's magnetosphere, the charged particles can interact with a variety of electromagnetic waves. The interactions include wave damping (wave loses energy to particles) and wave growing (wave gains energy from particles and can be amplified by the particles). One type of the commonly amplified electromagnetic waves is the whistler mode wave. It is a right-hand circularly polarized electromagnetic wave with the frequency range between the local electron cyclotron frequency f_{ce} and the lower hybrid resonance frequency f_{LHR}. It is believed [Contel et al., 2016; Wilder et al., 2017; Yoo et al., 2018] that the whistler mode waves are typically amplified under an anisotropic electron temperature condition of $T_\perp > T_\parallel$ (subscript $\perp$ and $\parallel$ represent the direction perpendicular and parallel to the background magnetic field respectively). Examples of whistler mode waves in the magnetosphere include plasmaspheric hiss inside the plasmasphere and chorus waves that typically occur outside the plasmasphere. Figure 1.5 and Figure 1.6 show the spatial distribution and observed spectra of some important plasma waves (including the whistler mode waves) in the magnetosphere respectively.

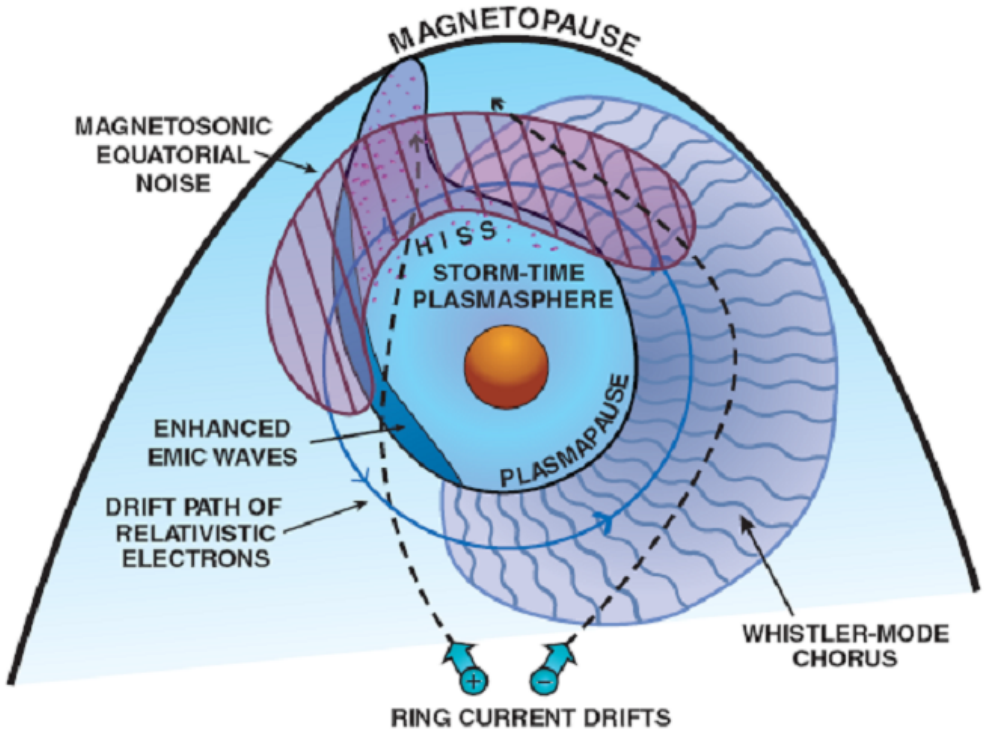

Figure 1.5. Schematic diagram showing the spatial distribution of important waves in the inner magnetosphere [Thorne et al., 2010].

Chorus emission occurs in the Earth's magnetosphere in the typical frequency range between 0.1 to 0.8 f_{ce}, with two separate frequency bands [Tsurutani and Smith, 1977; Koons and Roeder, 1990]. One band is from 0.1 to 0.5 f_{ce} (the lower band) and the other is above 0.5 f_{ce} (the upper band), with a power spectral density gap near 0.5 f_{ce} [Tsurutani and Smith, 1974; Burtis and Helliwell, 1976, 1969]. Figure 1.7 shows the magnetic field spectrogram of chorus waves, which often appears as a series of rising tone elements (frequency increasing with time). The chorus waves originate near the geomagnetic equator outside the plasmapause [LeDocq et al., 1998; Lauben and Others, 2002; Santolík et al., 2003a] due to the cyclotron resonant interaction with anisotropic plasma sheet electrons injected into the inner magnetosphere in the 10-100 keV energy range [Li and Others, 2009, 2010]. Recent studies indicate that the intensity and occurrence of chorus waves are associated with geo-

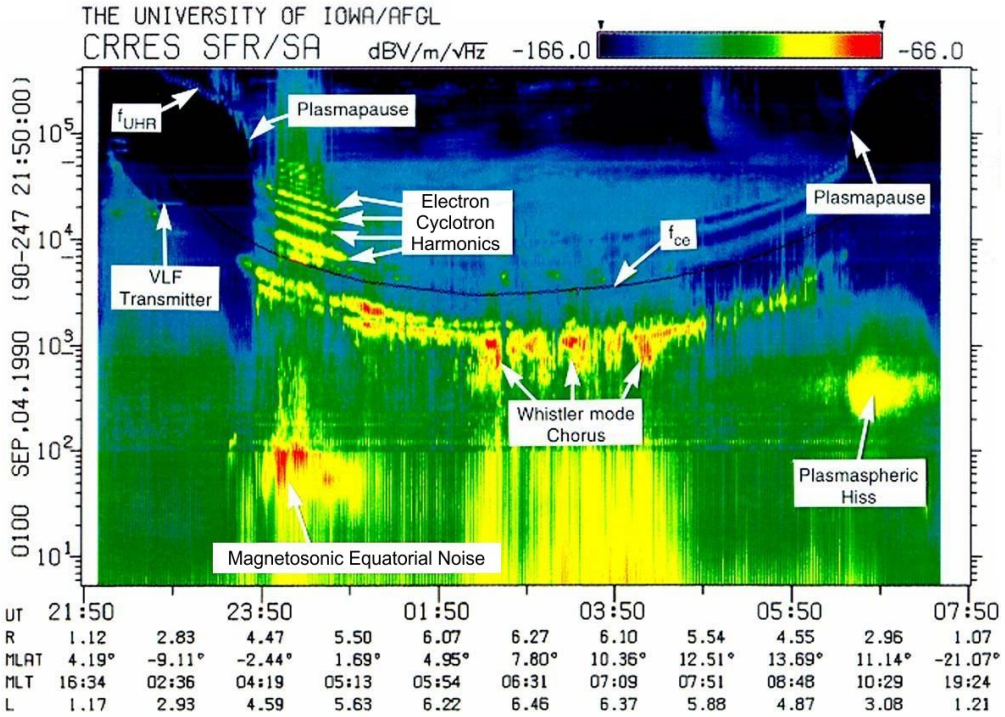

Figure 1.6. Spectrogram of waves in the magnetosphere observed by Combined Release and Radiation Effects Satellite (CRRES) [Kletzing and Others, 2013].

magnetic activity [Tsurutani and Smith, 1974; Meredith et al., 2001; Meredith and Others, 2003b,a; Miyoshi and Others, 2003; Lyons and Others, 2005], and most of the chorus waves occur during geomagnetic disturbances. The chorus emissions play an important role in the dynamics of the outer radiation belt by causing electron scattering in pitch angle and energy, which leads to electron acceleration in the heart of the outer radiation belt and precipitation loss into the atmosphere. This process is also believed to be the dominant mechanism responsible for the global distribution of the pulsating [Nishimura et al., 2011] and diffuse auroral [Thorne et al., 2010] precipitations, which provides important energy input for the ionosphere.

Plasmaspheric hiss is confined to high-density plasmasphere and dayside plumes [Thorne et al., 1973; Meredith et al., 2004]. It is broadband, structureless, and incoherent electromagnetic emission with a frequency range from ∼100 Hz to several kHz [Meredith et al.,

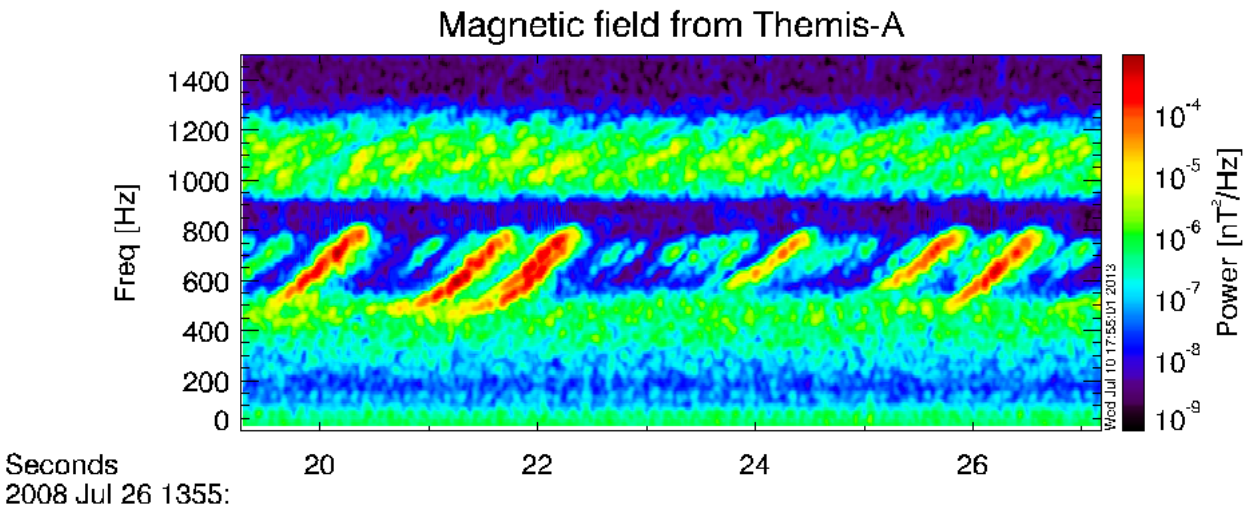

Figure 1.7. Spectrogram of magnetic field data from THEMIS for Whistler mode Chorus wave [University of Calgary Website, https://www.ucalgary.ca/above/science/chorus].

2004]. The amplitude of this broadband hiss can vary from ∼10 pT or less under quite condition [Thorne et al., 1973] to ∼100 pT during geomagnetic active times [Smith et al., 1974]. One main embryonic source of hiss has been verified to be the lower band chorus generated outside the plasmasphere [Bortnik et al., 2009; Meredith et al., 2013]. Lightning-generated whistler may also contribute to the plasmaspheric hiss [Green et al., 2005]. Previous simulation studies indicate that hiss emission is the main driver of the formation of the slot region between the inner and outer radiation belts [Lyons and Thorne, 1973; Abel and Thorne, 1998a,b]. Also, hiss waves can result in the loss of energetic electrons in the outer radiation belt. Recent studies illustrate that the plasmaspheric hiss can propagate nearly along the magnetic field line into the ionosphere and become the low altitude ionospheric hiss [Santolík and Parrot, 1999; Santolík et al., 2006a; Chen et al., 2017].

1.5 ULF Waves and Field Line Resonance

Ultra low frequency (ULF) MHD plasma waves have been observed throughout the Earth's magnetosphere and on the ground. The frequency range of the ULF wave is 1 mHz$\leq f \leq$ 10

Table 1.1. The period bands of Continuous Pulsations and Irregular Pulsations.

Continuous Pulsations		**Irregular Pulsations**	
Class	**Period (s)**	**Class**	**Period (s)**
Pc1	0.2-5	Pi1	1-45
Pc2	5-10	Pi2	45-150
Pc3	10-45		
Pc4	45-150		
Pc5	150-600		

Hz. According to the waveform observation, the ULF can be classified into two types: (1) waves with quasi-sinusoidal waveform are called pulsations continuous (Pc), (2) waves with irregular waveforms are pulsations irregular (Pi). According to the observed period, the Pc is subdivided into 5 period bands Pc1-5 and Pi is subdivided into 2 period bands Pi1-2. The period bands of Pc1-5 and Pi1-2 are shown in Table 1.1.

The ULF wave can be generated by both external sources (solar wind, shocks, etc.) and internal sources inside the magnetosphere (substorm injection, plasma instability, etc.). The external generated ULF waves always have low azimuthal wave number $m_\phi \sim O(1)$ and the m_ϕ of internal excited ULF waves is much higher ($\sim O(100)$). Both kinds of waves can couple with the field line resonance (FLR) when the frequency of the wave is close to the eigenfrequency of the magnetic field line. The FLR is the oscillation of the Earth's magnetic field line which behaves like a vibrating string with two ends frozen in the ionosphere. There are three typical modes of FLR: 1. the poloidal mode with oscillating B_r and E_ϕ components, where subscripts r and ϕ denote the radial and azimuthal directions respectively; 2. the toroidal mode with oscillating B_ϕ and E_r; 3. the compressional mode with the oscillating $B_\parallel$, B_r and E_ϕ, where subscript $\parallel$ represents the direction of the background magnetic field. FLR modes in the inhomogeneous plasma can recover Alfvénic mode in a uniform background when inhomogeneity in the magnetic field and plasma vanishes. The descriptions of ULF wave modes and FLR under magnetohydrodynamics (MHD) assumption are provided

in Appendix A. All three types may have fundamental and harmonic oscillations. The harmonics are named according to the number of electric field nodes ($E = 0$). For fundamental modes, only two nodes exist at the two ends of the field lines. The second harmonic mode has one additional node at the equator (electric field vanishes at the equator). The third harmonic mode has two extra nodes off the equator. Figure 1.8 gives examples of fundamental harmonics and 2nd harmonics for poloidal and toroidal modes. Different harmonics may be simultaneously excited if the source is broadband.

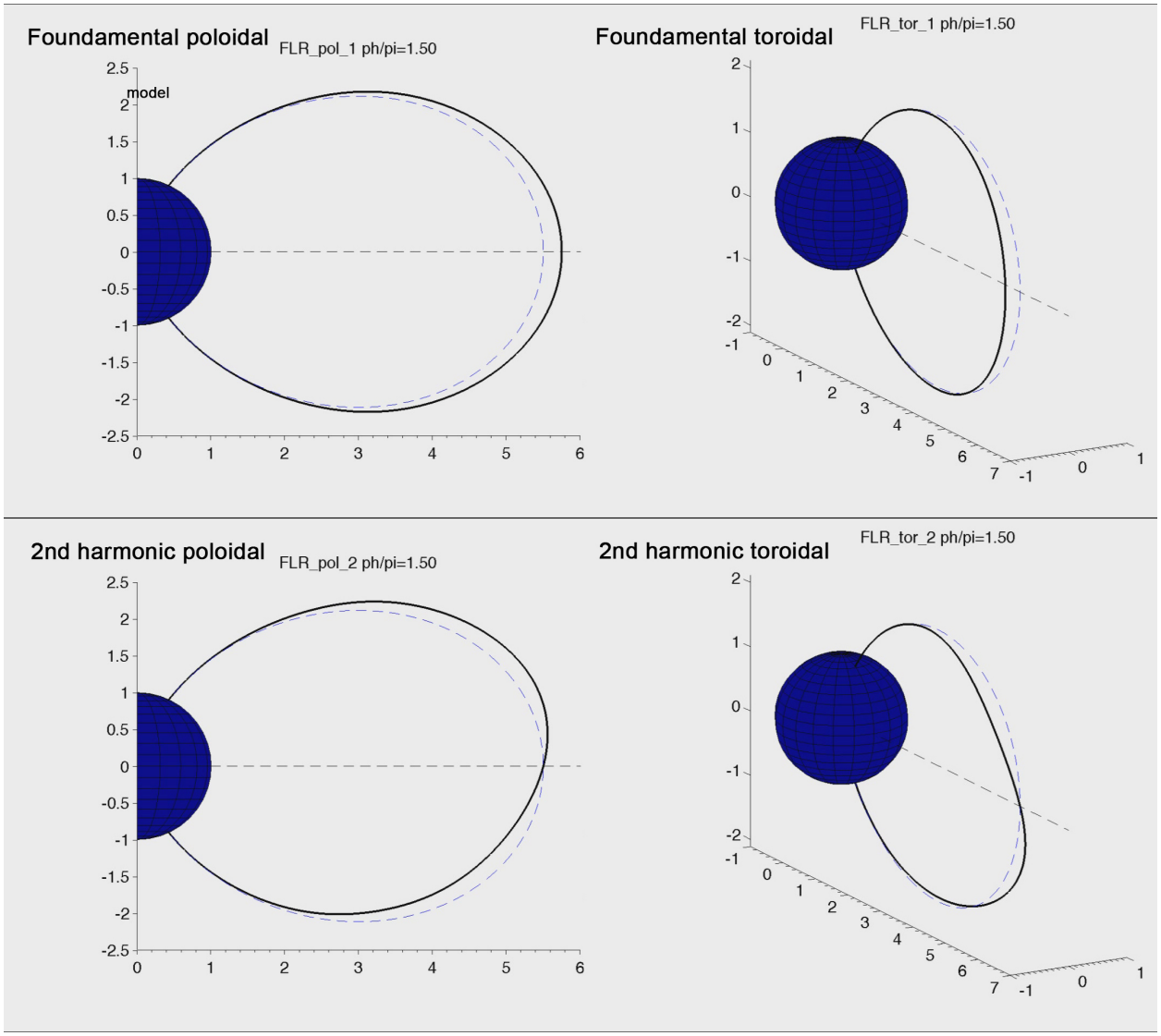

Figure 1.8. Fundamental harmonic (top row) and 2nd harmonic (bottom row) for poloidal mode (left panels) and toroidal mode (right panels) FLRs.

1.6 Modulation of VLF Whistler Waves

The observed spectra of chorus waves usually exhibit discrete structures with a time duration of about a tenth to a few tenths of seconds [Santolík et al., 2003a]. The emission elements usually gathered together and modulated on a timescale between a few seconds and a few minutes, which corresponds to the period of Pc4-5 ULF waves. This period matching indicates a close relationship between the VLF waves and ULF waves. Observations since several decades ago [Kimura, 1974; Sato et al., 1974; Sato and Fukunishi, 1981] have indicated that the intensity of whistler waves can be modulated by the compressional component of ULF waves. This modulation of whistler waves by ULF waves is considered as a subsequent effect of modulation of energetic electron flux by ULF waves because chorus waves are generated by cyclotron resonant interaction with anisotropic energetic electrons. However most of these observations are from ground-based high latitude stations, which makes the observations very indirect due to the equatorial spatial confinement of whistler waves' excitation [LeDocq et al., 1998; Lauben and Others, 2002; Santolík et al., 2003a], the damping effect (such as Landau damping) in the propagation of whistler waves from the magnetic equator to the ionosphere [Bortnik et al., 2007a; Li et al., 2008], as well as the shielding of compressional waves in the magnetosphere by the ionosphere [Hughes and Southwood, 1976]. Recently, Li et al. [2011a] performed simultaneous observations of chorus waves, ULF waves and particle distributions near the magnetic equator in the magnetosphere by the Time History of Events and Macroscale Interactions during Substorms (THEMIS) [Sibeck and Angelopoulos, 2008] satellites to investigate the modulation between chorus and ULF waves. Figure 1.9 is one of the representative events in [Li et al., 2011a], in which compressional Pc4-5 pulsations with an anticorrelation between the total electron density and the background magnetic field. The intensity of chorus emission varied nearly in-phase with electron density and out-of-phase with background magnetic field. The following statistical analysis in this study indicates that most modulation events relevant to the ULF waves occur in the outer magnetosphere

(L=8-12) and near the dawn sector as shown by Figure 1.10. Besides the compressional ULF waves, the perturbation of only plasma density can also modulate the intensity of chorus waves either in-phase or out-of-phase, which both can be explained by the linear theory of whistler waves [Li et al., 2011b].

The intensity of hiss can also be modulated by the variation of background plasma density with high wave intensity in high density regions, which may be caused by either local amplification or propagation effect [Chen et al., 2012]. Recently, Shi et al. [2018] reported an in-situ event in which injected energetic electrons drifted from the nightside to the dayside and were modulated by ULF waves via drift resonance [Dai and Others, 2013; Hao et al., 2014; Chen et al., 2017; Zhou et al., 2015, 2016; Li et al., 2017]. The modulated electrons consequently modulated the intensity of hiss waves through local amplification, which is observed by Van Allen Probe B satellite. An illustration of this event is shown in Figure 1.11 below.

In summary, previous studies indicate that the modulation effects of ULF waves on VLF whistler waves can be explained by either the concentration of VLF whistler waves during propagation due to the plasma density variation or the local amplification caused by the variations of plasma density, energetic particle flux and background magnetic field which can be modulated by the ULF waves.

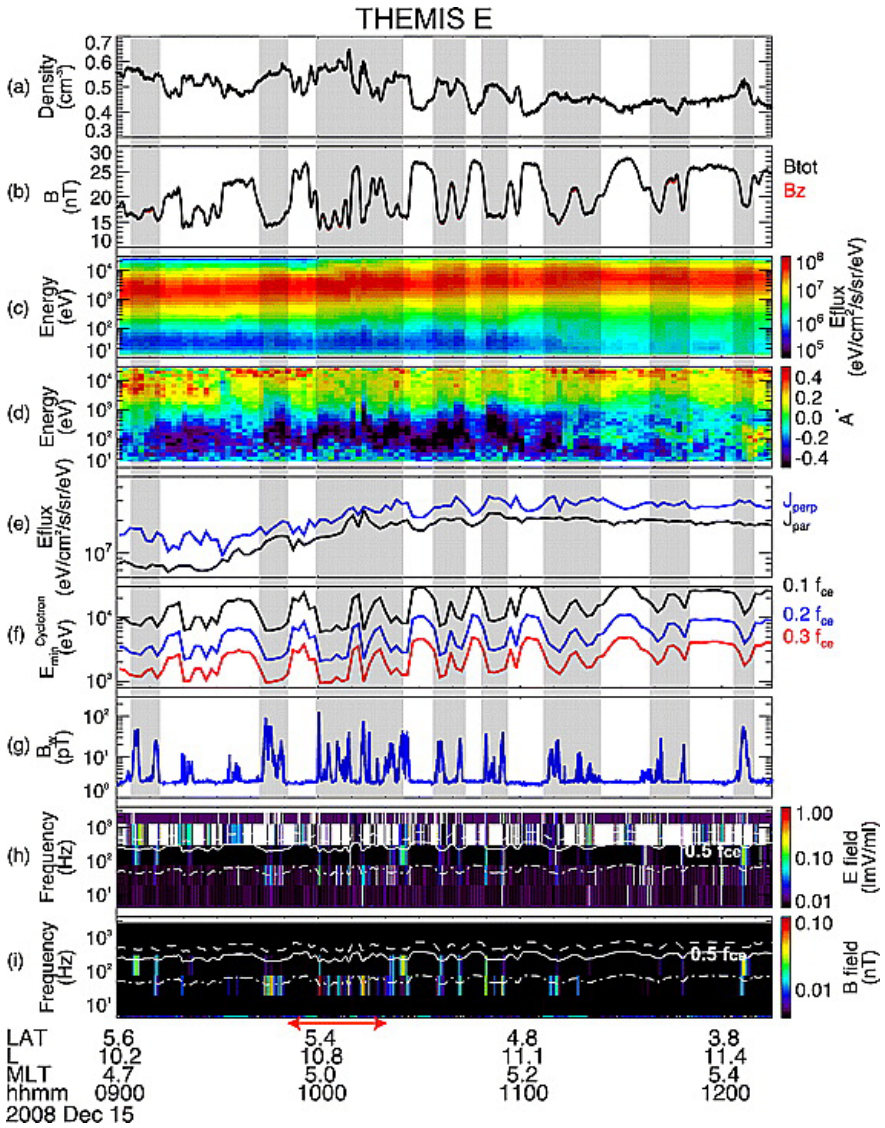

Figure 1.9. Chorus modulation event observed by THEMIS E satellite[Li et al., 2011a]. (a) Total electron density, (b) total magnetic field (black) and magnetic field in the z direction in the SM coordinate (red). (c) Omnidirectional electron energy flux and (d) electron anisotropy (A) (e) Electron energy flux (3-30 keV) perpendicular (blue) and parallel (black) , (f) Minimum resonant energy of electrons interacting with waves of three normalized frequencies through the first-order cyclotron resonance, (g) root mean square of wave magnetic field amplitude (0.05-0.8 f_{ce}), and time-frequency spectrograms of (h) wave electric and (i) magnetic fields. The three white lines in Figures 1.9h and 1.9i represent 1 f_{ce} (dashed), 0.5 f_{ce} (solid), and 0.1 f_{ce} (dash-dot).

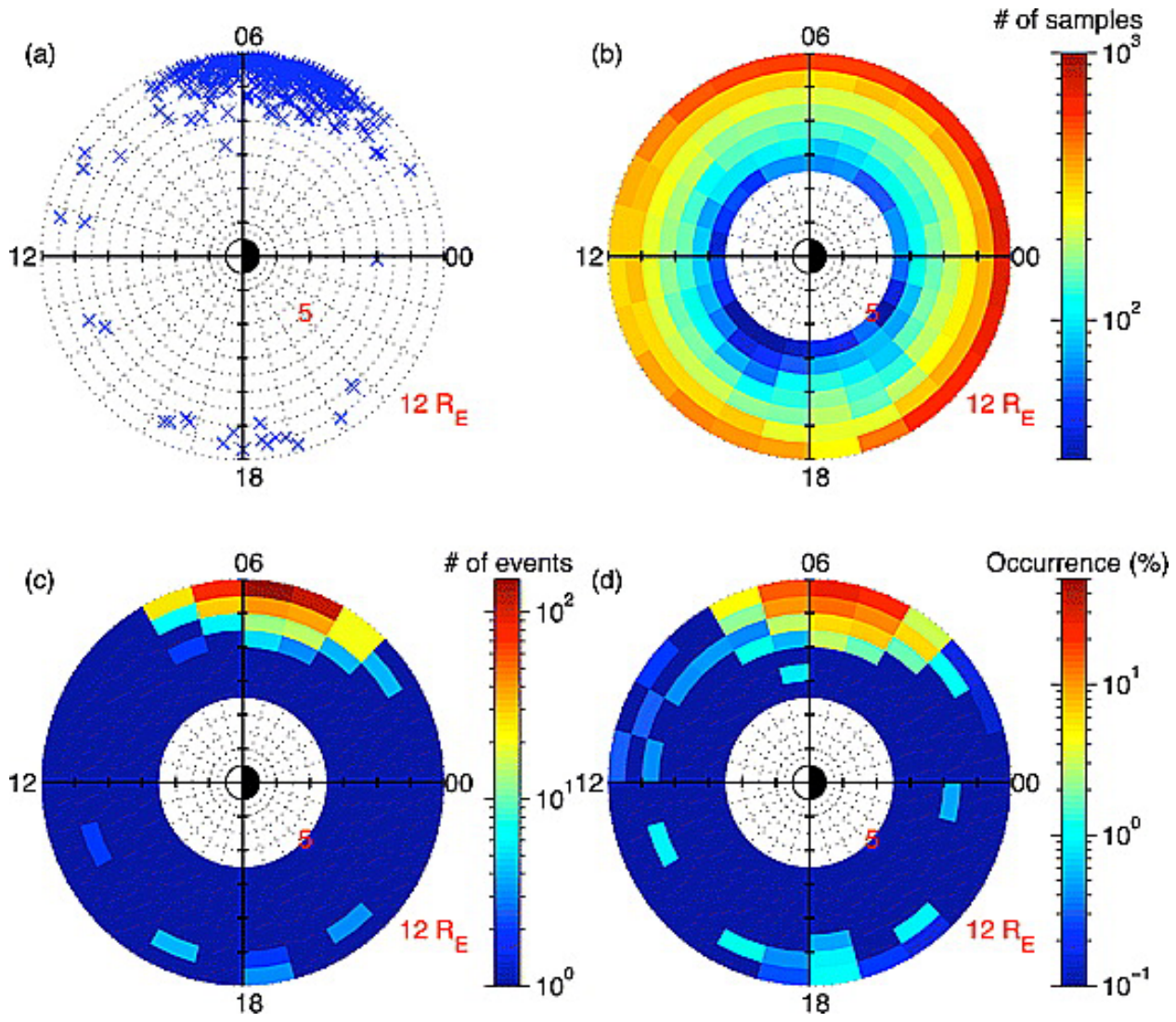

Figure 1.10. Global distributions of (a) the location of events, (b) number of samples, (c) number of events, and (d) the occurrence rate (%) of the events in regions of 5 and 12 R_E at all MLTs.[Li et al., 2011a].

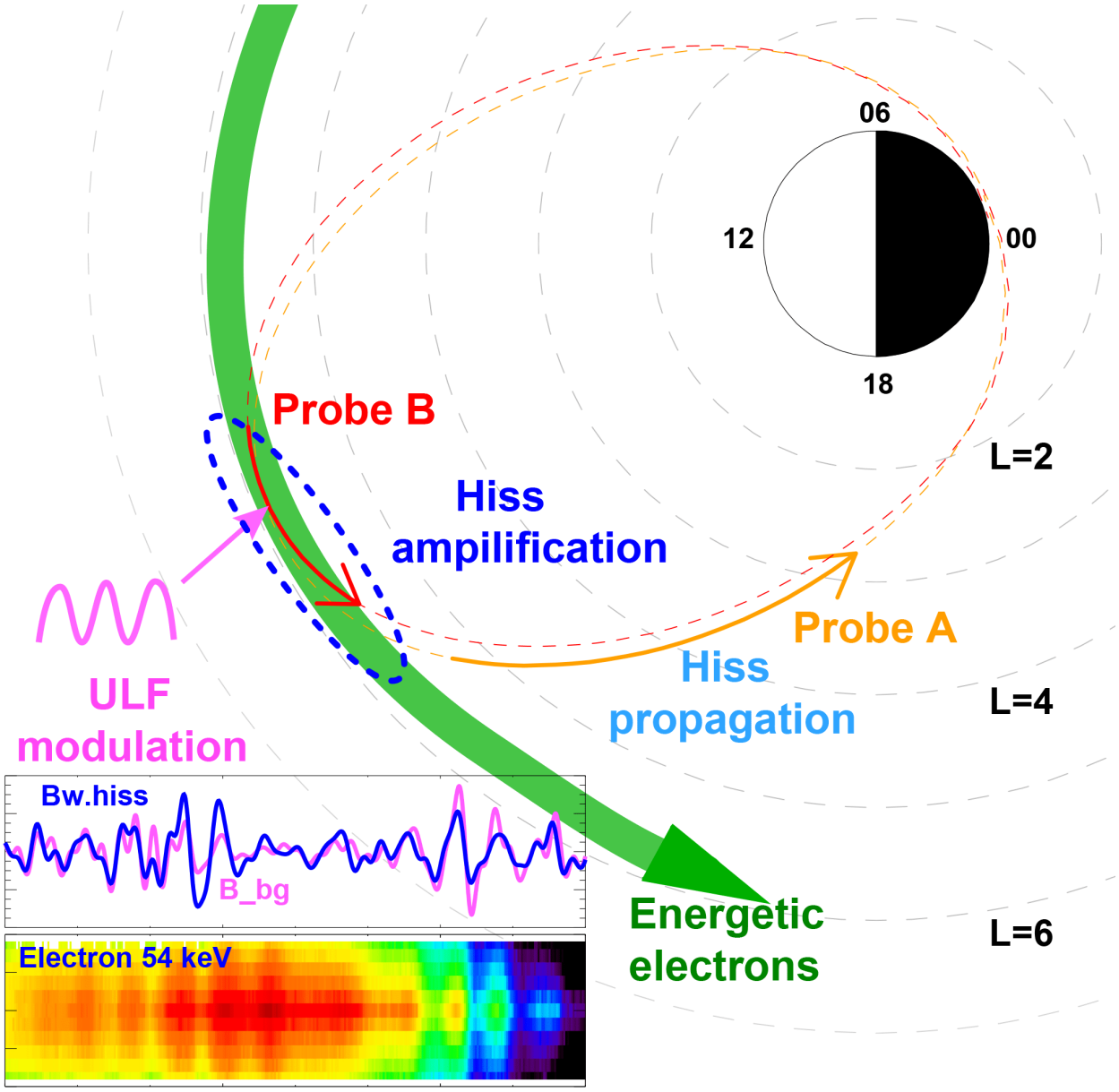

Figure 1.11. An illustration showing the energetic electron trajectory (green), ULF waves (pink) and hiss intensity modulation (blue) [Shi et al., 2018].

1.7 Dissertation Outline

This dissertation focuses on the modulation of VLF whistler waves by ULF waves. The outline of this dissertation is as follows. In Chapter 2, an in-situ observation of chorus modulation by ULF wave in the inner magnetosphere is presented and analyzed. In Chapter 3, I built a two-dimensional (2D) self-consistent magnetic field (SCB) model and applied it to the eigenmode analysis of the ULF field line resonance. In Chapter 4, I performed a statistical study of chorus modulation by perturbations of background magnetic field and plasma density and analyzed the relationship between the chorus intensity and the amplitudes of the perturbations. Besides the above works about the chorus modulation by ULF waves, two other relevant works led by myself are also included in this dissertation as Chapters 5 and 6. In Chapter 5, I used the 2D SCB model to analyze the effects of ring current pressure on magnetic field configuration, particle drift motions as well as the formation of the magnetic dip structure. In Chapter 6, I use in-situ measurements to statistically study the distribution of ionospheric hiss power and explain its propagation mechanism with a ray tracing model. Finally, I summarize the results presented and discuss future works relevant to my dissertation study in Chapter 7.

CHAPTER 2

MODULATION OF CHORUS INTENSITY BY ULF WAVES DEEP IN THE INNER MAGNETOSPHERE[1]

The work shown in this chapter has been published as "**Xia, Z.**, L. Chen, L. Dai, S. G. Claudepierre, A. A. Chan, A. R. Soto-Chavez, and G. D. Reeves (2016), **Modulation of chorus intensity by ULF waves deep in the inner magnetosphere**, *Geophys. Res. Lett.*, 43, 9444-9452, doi:10.1002/2016GL070280".

2.1 Introduction

Chorus emission is one of the whistler-mode waves occurring in the Earths magnetosphere in the typical frequency range between 0.1 to 0.8 f_{ce} (f_{ce} is the equatorial electron gyrofrequency) [Tsurutani and Smith, 1977; Koons and Roeder, 1990]. Chorus usually occurs in two separate frequency bands within the frequency range mentioned above, one is 0.1 to 0.5 f_{ce} (the lower band) and the other is above 0.5 f_{ce} (the upper band) [Tsurutani and Smith, 1974; Burtis and Helliwell, 1976, 1969]. The chorus waves originate near the geomagnetic equator outside the plasmapause [LeDocq et al., 1998; Lauben and Others, 2002; Santolík et al., 2003a] due to the cyclotron resonant interaction with anisotropic plasma sheet electrons injected into the inner magnetosphere in the 10-100 keV energy range [Li and Others, 2009, 2010]. It is generally believed that the intensity and occurrence of chorus are associated with geomagnetic activity, and most of the chorus waves take place during geomagnetic disturbances [Tsurutani and Smith, 1974; Meredith et al., 2001; Meredith and Others, 2003b,a; Miyoshi and Others, 2003; Lyons and Others, 2005].

[1]©2016 Amercian Geophysical Union. Portions Adapted, with permission from, Z. Xia, "Modulation of chorus intensity by ULF waves deep in the inner magnetosphere," Xia, Z., L. Chen, L. Dai, S. G. Claudepierre, A. A. Chan, A. R. Soto-Chavez, and G. D. Reeves, Geophys. Res. Lett., 43.

Ultralow frequency (ULF) oscillation of geomagnetic field lines can be excited, in general, by sources external or internal to the magnetosphere. Solar wind dynamic pressure fluctuations can be a substantial source for magnetosphere ULF wave power [Kessel, 2008; Takahashi and Ukhorskiy, 2007; Dai and Others, 2015]. ULF waves generated by external sources are compressional waves of fast-mode nature and characterized by a global-scale azimuthal wavelength (or small azimuthal wave number). In contrast, internal instabilities excite more localized ULF waves with a small azimuthal wavelength. The instabilities could be drift or drift-bounce instability [Southwood, 1976; Dai and Others, 2013] or drift mirror instability [Cheng and Lin, 1987; Chen and Hasegawa, 1991]. These two instabilities, which generally are coupled, are more effective in low-β and high-β plasma, respectively.

The time scale of the chorus elements is about a tenth to a few tenths of seconds [Santolík et al., 2003a]. Previous studies have shown that the intensity of chorus waves can be modulated by ULF waves on a few seconds to a few minutes timescale [e.g., Tixier and Cornilleau-Wehrlin, 1986; Manninen et al., 2010]. Li et al. [2011a] have analyzed several events where the intensity of chorus waves can be modulated by the compressional Pc4-Pc5 ULF waves with antiphase correlation between the magnetic field and electron density which is inferred from spacecraft potential. They found that the chorus intensity enhances with increased electron density and with depletion of magnetic field and is weaker when the electron density reaches its valley and magnetic field reaches its crest. This kind of modulations occurs in the large L shell area (8 to 12) where external solar wind sources are likely the driver. In this paper, we present Van Allen Probes observation of a modulation of chorus wave intensity by ULF waves event, which is excited internally deep in the magnetosphere during a strong geomagnetic storm and also shows many other modulating signatures. The Van Allen Probes (formerly known as the Radiation Belt Storm Probes (RBSP)) [Mauk and Others, 2013] are capable of detecting the upper hybrid resonance line, which enables calibration of density inferred from spacecraft potential and better captures the density variation associated with ULF waves. The organization of this paper is as follows: Van Allen

Probes instrumentation is described in Section 2.2, followed by the observation and the interpretation of the modulation event in Sections 2.3 and 2.4.

2.2 Van Allen Probes Instrumentation

The Electric and Magnetic Field Instrument Suite and Integrated Science (EMFISIS) [Kletzing and Others, 2013] carries two sensors, a tri-axial fluxgate magnetometer (MAG) and a trixaxial AC magnetic search coil magnetometer (MSC), which provide comprehensive wave magnetic field measurements in a 10 Hz to 400 kHz frequency range. The Electric Field and Waves Suite (EFW) [Wygant and Others, 2013] is used to study the electric fields in near-Earth space; it provides not only the components of electric field, but also a spacecraft potential estimate covering cold plasma densities of 0.1 to 100 cm^{-3}. The empirical density-potential formula has been calibrated according to EMFISIS Upper Hybrid resonance (UHR) lines, which provides more accurate characterization of density variation associated with ULF waves than previous studies [e.g., Li et al., 2011a]. The Energetic Particle, Composition, and Thermal Plasma Suite (ECT) [Spence and Others, 2013] is made up of three separate components: Helium Oxygen Proton Electron (HOPE) for the energy range 0.001 to 50 keV [Funsten and Others, 2013]; Magnetic Electron Ion Spectrometer (MagEIS), for three different particle populations (ring current electrons $\sim$20 to $\sim$200 keV and radiation belt electrons $>\sim$200 keV to $\sim$3 MeV, ring current protons and radiation belt protons 60 keV to 1 MeV) [Blake and Others, 2013]; and the Relativistic Electron Proton Telescope (REPT) for the proton energy range $\sim$17 to $>$100 MeV and electron energy range $\sim$1.6 to $>\sim$19 MeV [Baker and Others, 2013].

The Van Allen Probes are two robotic spacecrafts equipped with identical instruments and move on nearly identical orbits near the Earths equatorial plane.

The Electric and Magnetic Field Instrument Suite and Integrated Science (EMFISIS) [Kletzing and Others, 2013] carries two sensors, a triaxial fluxgate magnetometer (MAG)

and a triaxial AC magnetic search coil magnetometer, which provide comprehensive wave magnetic field measurements in the frequency range of 10 Hz to 400 kHz. The Electric Field and Waves Suite (EFW) [Wygant and Others, 2013] is used to study the electric fields in near-Earth space; it provides not only the components of electric field but also a spacecraft potential estimate covering cold plasma densities of 0.1 to 100 cm^{-3}. The empirical density-potential formula has been calibrated according to EMFISIS upper hybrid resonance (UHR) lines, which provides more accurate characterization of density variation associated with ULF waves than previous studies [e.g., Li et al., 2011a] using spacecraft potential alone. The Energetic Particle, Composition, and Thermal Plasma Suite (ECT) [Spence and Others, 2013] is made up of three separate components: Helium, Oxygen, Proton, and Electron (HOPE) for the energy range 0.001 to 50 keV [Funsten and Others, 2013]; Magnetic Electron Ion Spectrometer (MagEIS), for three different particle populations (ring current electrons $\sim$20 to $\sim$200 keV and radiation belt electrons $>\sim$200 keV to $\sim$3 MeV, ring current protons, and radiation belt protons 60 keV to 1 MeV) [Blake and Others, 2013]; and the Relativistic Electron Proton Telescope for the proton energy range $\sim$17 to $>$100 MeV and electron energy range $\sim$1.6 to $>\sim$19 MeV [Baker and Others, 2013].

2.3 ULF Wave Observation

The ULF event of interest observed by Van Allen Probes occurs during a storm between 13:40 UT and 14:30 UT on 6 July 2013. Figures 2.1a-2.1g show the variations of geomagnetic indexes and solar wind parameters over 3 days of 5-8 July. The red vertical line labeled t_0 marks the time when RBSP B detected the modulation event, and the green and blue vertical lines labeled t_- and t_+, respectively, are the last and next time periods when RBSP A passes near the location where the modulation event was observed at t_0. Figures 2.1h and 2.1i show the orbits of the RBSP A and RBSP B projected on the equator plane along the field line in solar magnetic (SM) coordinate. The projection of the RBSP B orbit in t_0 is around x=-4

R_E, y=3 R_E in the SM equatorial plane, while RBSP A traveled nearby (x=1 R_E, y=3 R_E). RBSP A moved through the event location at the two nearest time periods, about 09:24 UT to 10:14 UT (denoted as t_-) and 17:50 UT to 18:40 UT (denoted as t_+) on 6 July 2013, both of which are about 4 h away from t_0. We note that all the three time periods are within the storm period which lasts for a whole day on 6 July. In these three time periods, the Kp, AE, and Dst indexes all have high absolute values; the number density, and velocity of solar wind remain nearly constant at about 10 cm^{-3} and 340 km/s; and the interplanetary magnetic field B_z component remains negative (as low as -10 nT) over the entire day of 6 July, leading to a moderate geomagnetic storm with Dst minimum ∼-80 nT.

This geomagnetic storm results in the generation of ULF waves deep inside the magnetosphere ($L \sim 5$) and the corresponding modulation of chorus wave intensity, which will be the topics of this study. Figure 2.2 focuses on the modulation event observed from RBSP B. Figures 2.2a and 2.2b show the variations of the plasma density from spacecraft potential with calibration by the UHR line from EMFISIS and the three components of magnetic field fluctuation in the mean magnetic field aligned coordinate, radial component B_r, azimuthal component B_a, and parallel component B_p. The magnetic field fluctuation data are obtained from the original MAG magnetic field data after detrending with a smooth time window of 300 s. From Figures 2.2a and 2.2b, we can clearly see the variation of density is out of phase with the variation of B_p, while the B_a and B_r fluctuations are weaker comparing to the Bp fluctuation, indicating that this ULF wave is a mostly compressional wave with rather large amplitude Bp up to 10 nT. The period of the variation is about 150 s, which tells us that this is a Pc4-Pc5 ULF wave. The observed ULF wave is consistent with the wave generation through a drift mirror instability. In a pure drift mirror mode, $B_p >> B_r$ [Chen and Hasegawa, 1991], and in our event, the compressional component B_p is about 2-3 times larger than the poloidal component B_r (Figure 2.2b). Additional consistent characteristics of the drift mirror mode [Hasegawa, 1969] include the followings: (1) the variation of the

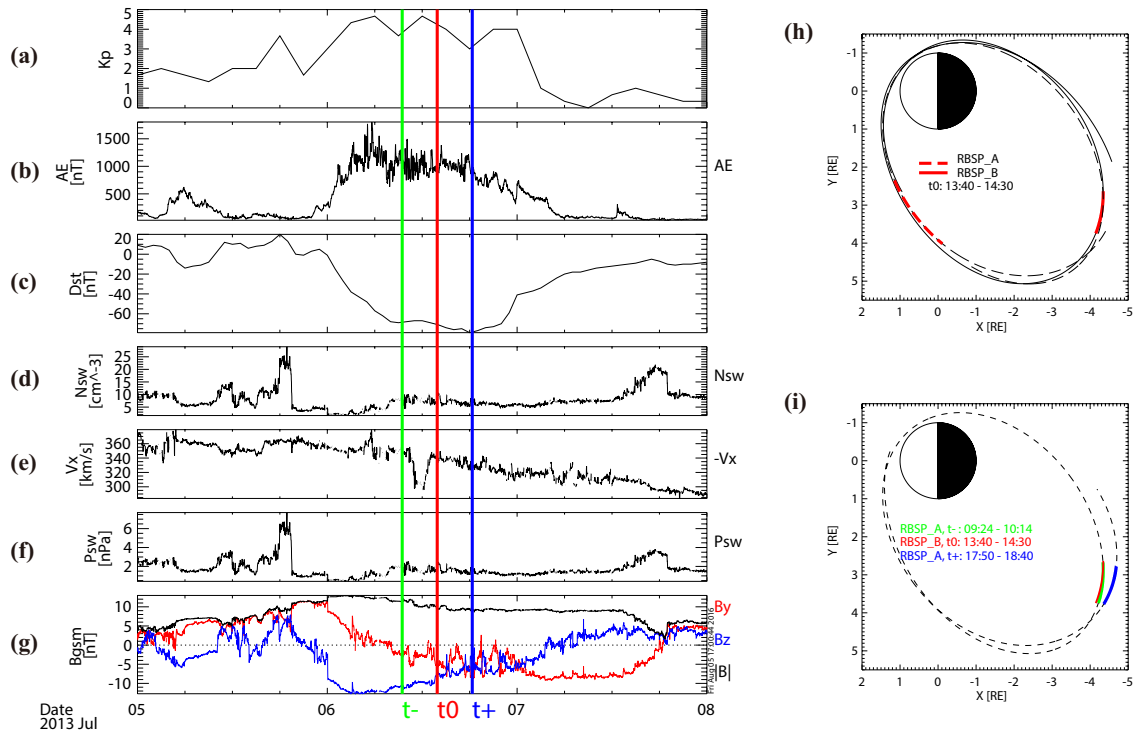

Figure 2.1. Overview of geomagnetic indexes and solar wind parameters from OMNI for the modulation event.
(a) Kp, (b) AE, (c) Dst index, (d) the solar wind density, (e) velocity, (f) pressure, and (g) magnetic field through the period of the storm event. The green, red and blue vertical lines denote the times t_-, t_0, and t_+, respectively (see text). (h and i) The orbits projected on the equator plane along a dipole field line for the satellites RBSP A and RBSP B. Red lines in Figure 2.1h highlight satellite orbits near t_0, and green, red, and blue lines in Figure 2.1i highlight the orbits near t_-, t_0, and t_+.

magnetic pressure and the variation of the plasma pressure are out of phase and comparable (Figure 2.2c), (2) the variation amplitude of perpendicular pressure is greater than that of parallel pressure (Figure 2.2c), (3) plasma beta is large (β_{perp} up to 2) and (4) the electric field perturbation at the ULF wave frequency is rather weak (not shown). In addition, the pressure of electrons exhibits similar characteristics but with much smaller variations (not shown) than that of protons (Figure 2.2c). Such large β (β_{perp} up to 2) closely approaches, but not exceeding, that required by the linear instability of drift mirror mode expressed

by the formula (24) in [Hasegawa, 1969]. Possible reasons for this are the relaxation by nonlinear saturation due to the large magnetic amplitude and the consideration of HOPE measurement ($<\sim$50 keV) only.

Because of the presence of finite radial magnetic field perturbation (B_r), we also check frequencies for pure poloidal modes. We solve for the eigenperiods in a dipole magnetic field using Equation (6) of Cummings et al. [1969] (see Appendix B) with L=5.5 (observation location), and adopting latitudinal dependence of mass density along a field line, $\rho(\lambda) = M_i N_{\rm eq} \cos^{-2m} \lambda$, where observed equatorial electron density $N_{\rm eq}$ =10 cm^{-3}, λ is the magnetic latitude, m is the density index, and M_i is the average ion mass. Figure 2.3 shows calculation of fundamental, second harmonic, and third harmonic poloidal mode periods as a function of M_i from 1 (all H^+ ions) to 16 (all O^+ ions) and a function of m over a typical range from 1 to 6. The observed period (150 s) is close to the fundamental period of the poloidal mode with $M_i \sim 1.5$, with little dependence on the m value. HOPE data provide H^+, He^+ and O^+ density measurements in the energy range above 30 eV, which are about 1.75, 0.07, and 0.35 cm^{-3}, respectively, over the event period. Based on those ion densities, M_i is about 3.5. Because thermal H^+ ions ($\sim$ eV) tend to be the dominant ion species, the value of M_i can be lower when taking in account ion populations below 30 eV, which is not available due to positive spacecraft charge. The second harmonic period is much shorter than the fundamental period and can match the observed period for a high value of m = 6 if nearly half ions are O^+, which is unlikely for our case. Comparison is even worse for second harmonic period with lower m and also for the period of the third harmonic. If it were second or third harmonic, it would need an unrealistically high-O^+ concentration (requiring dominant ions should be O^+ ions). We conclude that the observed ULF wave is a coupling between a drift mirror and fundamental poloidal mode.

The observed ULF wave closely modulates both electron and proton pitch angle distributions. Figures 2.2d-2.2i show electron phase space density (PSD) versus pitch angle at energy

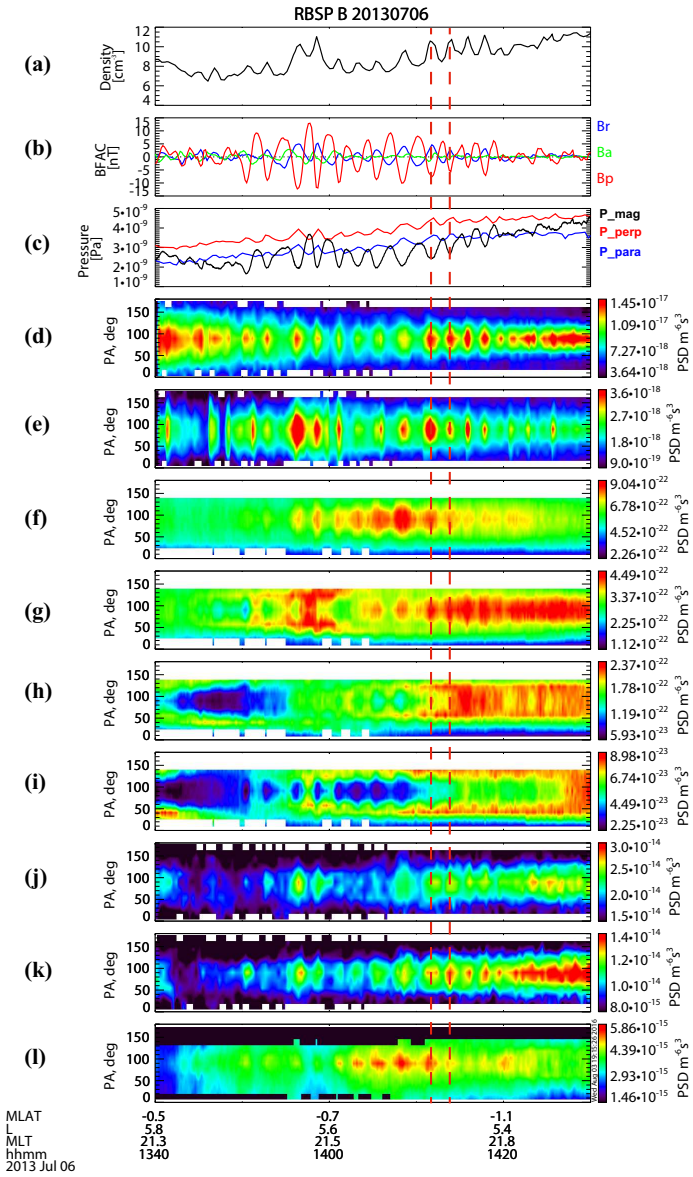

Figure 2.2. Relationship between particle distribution and ULF waves from RBSP B observations.
(a) the variation of plasma density from EFW s/c potential; (b) the variation of three components of magnetic field; (c) the variations of the magnetic pressure (black) and the perpendicular (red) and parallel (blue) pressures of protons; pitch angle distribution of electron phase space density at energies (d) 1046.67 eV, (e) 2620.96 eV, (f) 31.9 keV, (g) 54.4 keV, (h) 75.1 keV, and (i) 101.6 keV; and pitch angle distribution of proton phase space density at energies (j) 9631.9 eV, (k) 15,236.9 eV, and (l) 62.74 keV. The two vertical red-dotted lines denotes ULF wave phases corresponding to plasma density peaks.

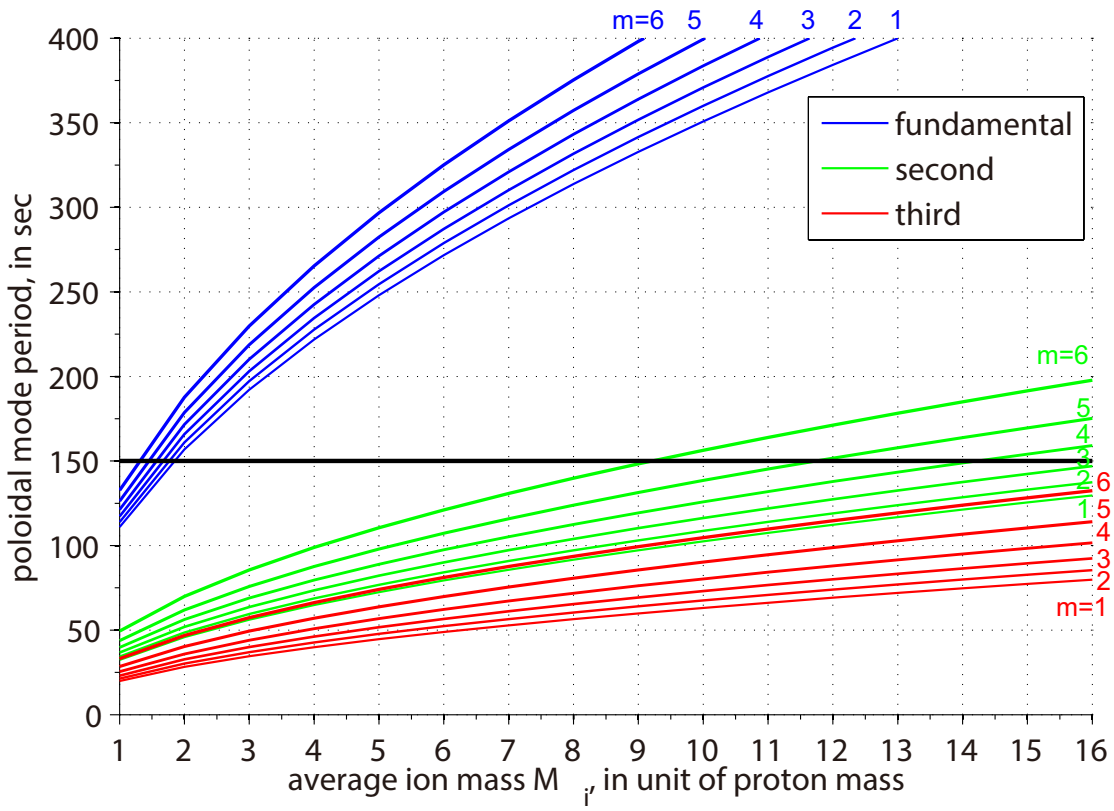

Figure 2.3. Calculation of poloidal mode periods as a function of average ion mass and field-aligned density index m.
Fundamental, second harmonic, and third harmonic poloidal modes are denoted by blue, green, and red lines, respectively. The horizontal black line denotes the period of the observed ULF wave. The numbers next to the lines represent the value of the density index m from 1 to 6.

channels 1047 and 2621 eV from the ECT-HOPE instrument and 32, 54, 75, and 102 keV from the ECT-MagEIS instrument. Figures 2.2j-2.2l show proton PSD at energy channels 9632 and 15,237 eV from ECT-HOPE and 62.74 keV from ECT-MagEIS. The distributions of both electrons (Figures 2.2d-2.2f) and protons (Figures 2.2j-2.2l) are modulated by the ULF wave in a similar fashion. The phase space densities of both protons and electrons increase especially near 90°pitch angle when the plasma density reaches its crest and B_p reaches its valley, while the phase space densities decrease at the plasma density valley and B_p crest. This feature is highlighted by the area between the two vertical red-dotted lines.

After checking electron and proton distributions at other energies we note that the electron energy ranging from 0.2 to 54 keV and the proton energy ranging from 5 to 63 keV are involved in this kind of ULF modulation and that these modulation signatures are not present clearly beyond these two energy ranges for electrons and ions respectively. Moreover, over a higher electron energy range 54.4 keV-101 keV (Figures 2.2g-2.2i), the electron distribution shows a different response at B_p valleys where electron PSD at 90°tends to reduce and peak PSD goes to lower pitch angle. The transition of electron PSD at 90°from out-of-phase with B_p to in-phase occurs over a relatively narrow energy range of 54-75 keV (Figures 2.2g and 2.2h). Note that there is no clear signature of such a transition in the response of proton distribution in our event. The phase-jump transition of electron PSD reported here is somewhat different from the transition of electron energy in drift-resonance response to ULF wave phase reported by Claudepierre and Others [2013], where modulated electron flux variation shows a clear energy of peak variation amplitude and the phase difference between electron flux variation and the ULF wave phase varies slowly as a function of energy. If one assumes the phase-jump transition reported by our event is another kind of electron drift resonance signature, then it can be estimated, using $f = nf_d$, that the ULF wave azimuthal number $n \sim 56$, where wave frequency $f = 1/150$ Hz and drift frequency f_d is calculated for electrons at energy 60 keV and equatorial pitch angle 90°at L = 5.5. The value of n is a reasonable value for an internally or kinetically excited magnetohydrodynamic wave. Further investigation of such electron behavior is beyond the scope of our current study.

2.4 Chorus Wave Observation

Figure 2.4 shows the relationship between ULF and VLF waves. Figures 2.4a and 2.4b show the B_p variation and the electron spectrum of 1046.67 eV, respectively, which are the same as Figures 2.2b and 2.2d. Figures 2.4c-2.4f show, respectively, the spectra of wave electric field, wave normal angle, ellipticity, and wave magnetic field from the EMFISIS measurement. At

the valley of B_p and the crest of the electron phase space density, there exists intense chorus wave magnetic and electric power below and above 0.5 f_{ce} with about 0°wave normal angle and ellipticity near 1. Chorus waves turn on and off quasiperiodically over 14:10 UT to 14:20 UT with time period close to the period of the ULF waves. Close examination shows that both upper and lower band chorus waves are intensified at the valleys of B_p (showed by the two vertical lines in Figure 2.4) corresponding to the increase of electron phase space density (Figure 2.4b), while chorus waves diminish at the crests of B_p. This relation is in part similar to the modulation event Li et al. [2011a] found, but our event occurred deep inside the magnetosphere where ULF wave is internally excited by ring current population. The set of ULF waves, VLF waves, and particle distributions provides strong support that ULF waves can modulate chorus wave intensity and that the variation of the electron distribution causes the chorus waves to turn on and off. We should make following two notes. First, there is no clear chorus modulation prior to 14:10 UT, although with variation of electron phase space density and linear growth rate. Second, some lower band chorus bursts (∼14:14 UT and 14:19 UT) can occur closer to density valleys (B_p crests) rather than density crests (B_p valleys). Those inconsistencies might be attributed to two physical processes other than local linear growth. First, nonlinear wave growth shows dependence on magnetic field topology, in particular the field-aligned variation of the ambient magnetic field [Tao, 2014; Katoh and Omura, 2011], which varies with ULF wave phases and depends on field line resonance (FLR) eigenmode structures. Second, propagation effect may also lead to wave refraction toward both lower and higher-density ducts [Katoh, 2014]. This is especially true for fine-scale density variation associated with ULF wave of high azimuthal wave number.

Variations of electron pitch angle distribution are the response to ULF waves, rather than the consequence of chorus waves scattering; this is supported by the following observations: (1) protons respond in similar fashion to electrons while chorus can not effectively scatter protons and (2) the presence of the electron variations already began at about 13:50 UT

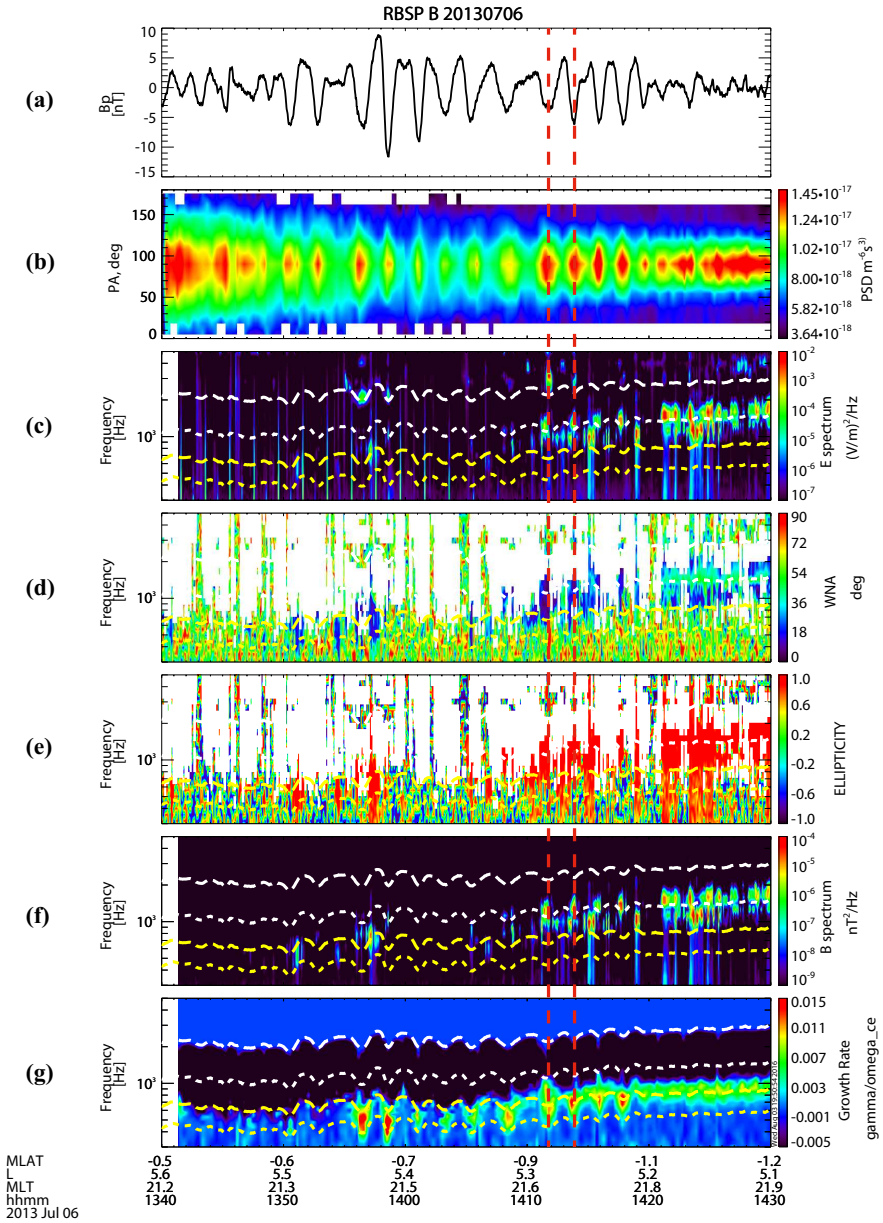

Figure 2.4. Relationship of magnetic perturbation and VLF chorus waves.
(a) the parallel magnetic field fluctuation (same as the red line in Figure 2.4b), (b) pitch angle distribution of electron phase space density at energy 1046.67 eV, (c) power spectrum density of wave electric field, (d) wave normal angle, (e) ellipticity, (f) wave magnetic field, and (g) the linear growth rate calculated. The white long dashed and short dashed lines represent f_{ce} and 0.5 f_{ce}, respectively, and the yellow long dashed and short dashed lines represent 0.3 f_{ce} and 0.2 f_{ce}, respectively.

(Figures 2.2d-2.2f), before the chorus wave variation (14:10 UT to 14:20 UT). Based on parameters typical for this observation event, electron minimum gyroresonant energy for the lower band chorus is several keV (not shown) and even lower for the upper band chorus. Thus, the phase jump near 50 keV mentioned above is unlikely a consequence of gyroresonance interaction.

To test the idea that electron variation is indeed responsible for chorus wave generation, linear instability analysis based on observed plasma condition is performed. The linear growth rate of whistler-mode waves can be calculated by using the linear theory equation [Kennel and Petschek, 1966] (see Appendix C) and using measured parameters, including plasma density (calibrated from upper hybrid resonant lines), background magnetic field, and observed electron velocity distribution from the HOPE instrument. These measurements from Van Allen Probes provide unambiguous parameters to make possible a definite test of the linear theory.

Figure 2.4g shows the growth rate as a function of time and frequency for parallel propagation. We also did calculations for other wave normal angles up to the whistler-mode resonance cone angle and found that the growth rate maximizes for parallel propagation. The result of linear growth rate analysis shows the coincidence between the maximum of the growth rate and the occurrence of intense chorus waves at $<\sim 0.3 f_{\mathrm{ce}}$, which is consistent with the variation of electron flux changing the plasma instability and thus generating the chorus waves. However, the frequency range of the growth rate enhancement and that of the chorus wave do not always match, especially for higher-frequency portions. The growth rate above 0.5 f_{ce} is very low all the time. This indicates that higher-frequency chorus waves, including upper band chorus, should be due to a mechanism other than linear instability.

With twin Van Allen Probes we can infer whether this modulation is local or global by examining two simultaneous observations and estimate its time duration. Temporal and spatial scales of this modulation event are checked using the Van Allen Probes pair. We

checked the RBSP A data at t_0, t_- and t_+ (indicated by Figure 2.1). No clear signatures of ULF waves and particle and chorus waves modulation are found at the t intervals, indicating that the event we analyzed only lasts no longer than a few hours. We also check RBSP A observation at t_0, which is about 2-3 R_E from RBSP B, and find no clear signature of ULF wave activity, either suggesting that the event captured by RBSP B is not a global ULF wave. Such spatially local and temporal natures are consistent with internally excited ULF waves. This localized phenomenon, occurring at premidnight during the main phase, might be associated with the westward edge of partial ring current (indicated by Figure 2.2c where thermal pressure increases with magnetic local time) developed from fresh injection.

2.5 Conclusions and Discussion

In summary, in this chapter we present an event of chorus modulation by ULF waves deep inside the magnetosphere. Using Van Allen Probes observations, we analyzed the relationships between the intensity of chorus wave and the magnitude of plasma density, magnetic field variation and the distribution of electrons and protons. Moreover, we also calculate the linear whistler-mode growth rate to help understand the mechanism of the modulation of chorus waves. Then we combined the observations of both RBSP A and B to estimate the temporal and spatial scales of this kind of modulation. Our conclusions are summarized as follows:

1. An event of ULF wave modulation of pitch angle distributions of both electrons and protons is reported deep in the magnetosphere, which occurs during a geomagnetic storm with long lasting negative interplanetary magnetic field B_z.

2. This ULF wave shows signatures of fundamental poloidal mode of field line resonance and mirror wave nature. At the crest of plasma density and the valley of the compressional component of the wave magnetic field, the phase space density near pitch angle 90°increases for protons over 5-63 keV and for electrons over 0.2-54 keV, while in contrast, the electron

pitch angle distributions are notably different (strongly field aligned) at the higher energies above 60 keV.

3. The ULF wave tends to modulate the electron distribution and thus the intensity of whistler-mode chorus waves; consistency with the linear growth rate analysis of the observed electron distribution for whistler mode at low frequency ($<\sim 0.3 f_{\mathrm{ce}}$). The linear instability, however, cannot account for the observed chorus at higher frequency (including the upper band chorus).

4. This ULF wave and modulation phenomenon is spatially local and does not last long.

Many observed modulation signatures along with our quantitative analysis, allow us to sort out the physical processes behind the event. Here is our interpretation based on the observation and the analysis performed. A local and temporal ULF wave with antiphase correlation between plasma density and compressional magnetic field component is generated internally deep in the magnetosphere, probably through a drift mirror instability. Self-consistently, the generated ULF wave causes disturbances in both electron and ion pitch angle distributions, whose anisotropy enhances in the crests of plasma density. The enhanced electron pitch angle distribution leads to enhanced chorus wave intensity at the low-frequency range ($<\sim 0.3 f_{\mathrm{ce}}$). Some other nonlinear mechanisms further trigger the chorus wave generation at higher-frequency range, including the upper band chorus. This conclusion provides strong observational support for nonlinear chorus wave generation mechanism, where linear growth rate at lower frequency is required and higher-frequency chorus can be generated nonlinearly in the form of rising tone element [Tao, 2014; Katoh and Omura, 2011].

There are a variety of ULF waves, with or without plasma density variation, compressional, or transverse wave magnetic field component, which are generated by different free energy. Besides chorus waves, there are also other types of whistler mode waves, such as plasmaspheric hiss or magnetosonic waves. Breneman and Others [2015] present an event of plasmaspheric hiss modulated by ULF waves over a global scale, leading to modulated

electron precipitation. Likewise, the modulated chorus emission might lead to modulated electron precipitation, such as the formation of pulsating aurora [Nishimura et al., 2010; Jaynes and Others, 2015]. General questions on ULF waves generation and their modulatory effect on VLF waves and electron precipitation are interesting and will be investigated with a continuing effort.

CHAPTER 3

EIGENMODE ANALYSIS OF COMPRESSIONAL POLOIDAL MODES IN A SELF-CONSISTENT MAGNETIC FIELD[1]

The work shown in this chapter has been published as "**Xia, Z.**, L. Chen, L. Zheng, and A. A. Chan (2017), **Eigenmode analysis of compressional poloidal modes in a self-consistent magnetic field**, *Journal of Geophysical Research: Space Physics*, 122, 1-13, doi:10.1002/2017JA024376".

3.1 Introduction

Ultralow frequency (ULF) waves in the magnetosphere can often be identified as standing Alfvén waves and coupled to a field line resonance (FLR) [Hughes, 1994]. They can be generated by both external sources (solar wind, shocks, etc.) and internal sources (substorm injection, plasma instability, etc.), with a characteristic azimuthal wave number m_ϕ: low m_ϕ waves ($m_\phi \sim O(1)$) for external sources and high m_ϕ waves ($m_\phi \sim O(100)$) for internal sources [Takahashi, 1988]. The FLR has three typical modes: (1) the poloidal mode with oscillating B_ψ and E_ϕ components, where subscripts ψ and ϕ denote the radial and azimuthal directions respectively; (2) the toroidal mode with oscillating B_ϕ and E_ψ; and 3) the compressional mode with oscillating $B_\parallel$, B_ψ and E_ϕ, where the subscript $\parallel$ represents the direction of the background magnetic field. Compressional poloidal waves have been observed to correspond to small m_ϕ and variations of the solar wind dynamic pressure (external source) [Dai and Others, 2015], as well as large m_ϕ and drift-bounce resonance (internal source) [Min et al., 2017], under the condition of low plasma β. The ULF waves can resonantly interact with both energetic electrons [e.g., Elkington et al., 1999; Zhou et al.,

[1]©2017 Amercian Geophysical Union. Portions Adapted, with permission from, Z. Xia, "Eigenmode analysis of compressional poloidal modes in a self-consistent magnetic field," Xia, Z., L. Chen, L. Zheng, and A. A. Chan, J. Geophys. Res. Space Physics, 122, 1-13.

2016] and ions [e.g., Ren et al., 2016] and also modulate particle distributions [Claudepierre and Others, 2013; Liu et al., 2016; Xia et al., 2016]. Thus, ULF waves play an important role in magnetospheric dynamic processes.

Many theoretical analyses of FLRs based on the Alfvén mode equation have been presented using different approaches, including magnetohydrodynamics (MHD) [e.g., Dungey, 1963; Cummings et al., 1969], kinetic theory [e.g., Southwood, 1976; Cheng and Lin, 1987], and gyrokinetic theory [e.g., Chen and Hasegawa, 1991; Chan et al., 1994]. Most previous models consider a dipole field geometry or one close to dipole for small β. Recently, advanced models have been developed for more complex magnetic fields to represent realistic magnetospheric conditions. Rankin et al. [2006] developed a fluid model of standing shear Alfvén waves that is applicable in a general magnetic field, such as the Tsyganenko 96 magnetic field [Tsyganenko and Stern, 1996; Tsyganenko and Peredo, 1994; Tsyganenko, 1995]. Cheremnykh et al. [2014, 2016] set up a two-dimensional (2-D) inhomogeneous cylinder model with hot plasma pressure and curved magnetic field and investigated the transverse structure and propagation of high m_ϕ ULF waves. Klimushkin and Mager [2015] derived an Alfvén mode equation in finite-pressure plasma using the gyrokinetic approach and found that the only wave mode from the solution is the Alfvén-ballooning compressional wave. This wave mode of high m_ϕ was investigated thoroughly by Chan et al. [1994] for a dipole field modified by a small plasma pressure perturbation. However, both studies were limited to a low β condition. The previous studies of FLR in cold plasma condition hardly produce the compressional mode whose presence is important for, e.g., modulating the distribution of particles and thus the intensity of chorus emission [Li et al., 2011a; Xia et al., 2016]. In order to study the compressional poloidal mode in the magnetosphere, it is necessary to analyze FLR under a plasma with a finite β value of $\sim O(1)$, which is the typical value for storm time ring current.

In this chapter, we solve for 2-D axisymmetric self-consistent magnetic field with a radially localized anisotropic plasma pressure with a finite β up to $O(1)$. This model is subsequently

applied to investigate compressional poloidal eigenmodes, specifically for the second harmonic. Moreover, motivated by the association of magnetic field dip and ring current [Ukhorskiy et al., 2006], we also use the self-consistent magnetic field to investigate the effect of plasma β and pressure anisotropy on the magnetic field dip formation.

3.2 Axisymmetric Equilibrium Model

The theory of the equilibrium magnetosphere model used in this study is based on the previous works of Cheng [1992] and Zaharia et al. [2004], which solve the MHD force balance equation for a quasi-static equilibrium state. The basic equations for the pressure equilibrium are as follows:

$$\mathbf{J} \times \mathbf{B} = \nabla \cdot \mathbf{P} \tag{3.1}$$

$$\nabla \times \mathbf{B} = \mu_0 \mathbf{J} \tag{3.2}$$

$$\nabla \cdot \mathbf{B} = 0 \tag{3.3}$$

where $\mathbf{J}$ is the current, $\mathbf{P}$ is the anisotropic thermal pressure tensor and $\mathbf{B}$ is the magnetic field. For Equation (3.1) the thermal pressure tensor $\mathbf{P}$ can be represented as $P_\perp \mathbf{I} - (P_\perp - P_\parallel)\hat{b}\hat{b}$, where $\mathbf{I}$ is unit tensor, $\hat{b} = \mathbf{B}/B$ is the unit vector of the field line direction, and $P_\perp$ and $P_\parallel$ are the perpendicular and parallel pressure components. For such anisotropic pressure, Equation (3.1) can be rewritten as follows:

$$\mu_0 \sigma_P (\mathbf{J} \times \mathbf{B}) = \mu_0 \nabla P_\perp - (\mathbf{B} \cdot \nabla \sigma_P)\mathbf{B} + (1 - \sigma_P)\nabla(\frac{B^2}{2}) \tag{3.4}$$

where $\sigma_P = 1 + \mu_0(P_\perp - P_\parallel)/B^2$.

From Equation (3.3), the magnetic field $\mathbf{B}$ is a divergence-free vector and can be expressed in terms of two Euler potentials ψ and α as $\mathbf{B} = \nabla\psi \times \nabla\alpha$. According to this definition, $\mathbf{B}$ is perpendicular to both $\nabla\psi$ and $\nabla\alpha$ and the intersections of constant ψ and constant α

surfaces correspond to magnetic field lines. Thus, in a field-aligned coordinate system for the geomagnetic field, ψ and α are constant along the field line parallel direction, whose gradients correspond to the other two directions, namely, the radial direction pointing from the Earth to the outside and the azimuthal direction that is perpendicular to the parallel and radial direction. For axisymmetric magnetic field model with zero toroidal component, the potential α is chosen to be the azimuthal angle ϕ and ψ is defined as the magnetic flux. For the Earths dipole magnetic field, $\psi = -B_D R_E^2/L$, where B_D the equatorial dipole field on the Earths surface, R_E is the Earth's radius and L is the L shell value.

The computation coordinates ρ, ζ and θ (shown by Figure 3.1) used in the axisymmetric model are curvilinear flux coordinates related to physical coordinates ψ, α, and the field line distance s, respectively, as follows:

$$\rho = \frac{\psi - \psi_{in}}{\psi_{out} - \psi_{in}}, \rho \in [0, 1], \tag{3.5}$$

$$\zeta = \alpha = \phi, \zeta \in [0, 2\pi], \tag{3.6}$$

$$\theta = \frac{\pi s}{s_0} + C_\theta \sin(\frac{2\pi s}{s_0}), \theta \in [0, \pi]. \tag{3.7}$$

Here ψ_{out} and ψ_{in} are the ψ values at the outer and inner boundaries, s_0 is the length of a magnetic field line, C_θ is the coefficient to adjust the density of grids in the θ direction (field line direction). We set $C_\theta = 0.25$ in the simulation. ρ is chosen to be linear with ψ, while θ is a nonlinear function of s in order to achieve higher grid density at higher-latitude regions. Since our model is axisymmetric (that is, ϕ independent), after dotting $\mathbf{B} \times \nabla\alpha$ at both sides and combining with Equation (3.2) and $\mathbf{B} = \nabla\psi \times \nabla\alpha$, Equation (3.4) can be rewritten as follows (see Appendix D):

$$\mu_0 \mathbf{J} \cdot \nabla\alpha = \nabla \cdot [(\nabla\alpha \cdot \nabla\psi)\nabla\alpha - (\nabla\alpha)^2 \nabla\psi] = -\frac{\mathbf{B} \times \nabla\alpha}{\sigma_P B^2}[\mu_0 \nabla P_\perp + (1 - \sigma_P)\nabla(\frac{B^2}{2})] \tag{3.8}$$

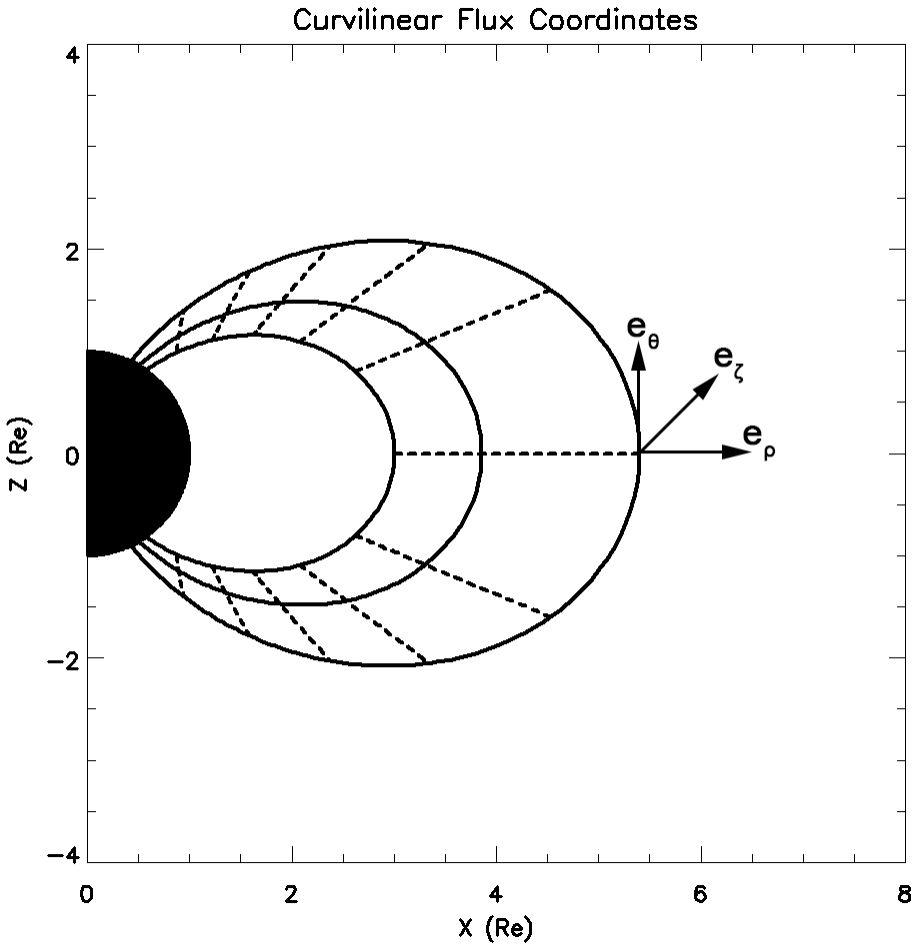

Figure 3.1. An illustration of the curvilinear flux coordinates (ρ, ζ, θ).
$\mathbf{e}_\rho$, $\mathbf{e}_\zeta$, $\mathbf{e}_\theta$ represent the three unit vectors. $\mathbf{e}_\rho$ is perpendicular to the magnetic field line, $\mathbf{e}_\zeta$ is in the azimuthal direction and $\mathbf{e}_\theta$ is parallel to the magnetic field line. The solid lines represent equal ρ (equal ψ) lines (magnetic field lines) and the dashed lines represent equal θ lines.

The simulation domain of our equilibrium model is set to be $[3R_E, 9R_E]$. The outer and inner boundaries are far enough from L_0 (the L shell of the thermal pressure peak) so that the plasma pressures at the boundaries are nearly zero. The number of ρ grid points n_ρ is set to 151, and the number of θ grid points n_θ is set to 181 to ensure sufficient accuracy. From Equation (3.8), once we know the distribution of the thermal pressure in the $\rho - \theta$ plane, we can obtain the distribution of ψ in the magnetosphere space and then calculate the magnetic field $\mathbf{B}$. We use an iteration method to solve (3.8) numerically as follows:

The initial anisotropic pressure distribution includes the perpendicular and parallel components $P_\perp$ and $P_\parallel$, whose values along the field line at arbitrary location can be given by [Tsyganenko, 2000] the following:

$$P_\perp = \frac{P_{\perp e}}{[1 + A_e(1 - S)]^2} \tag{3.9}$$

$$P_\parallel = \frac{P_{\parallel e}}{1 + A_e(1 - S)} \tag{3.10}$$

$$A = \frac{1}{1 + A_e(1 - S)} - 1 \tag{3.11}$$

where $S = B_e/B$ is the ratio between the magnitudes of the equatorial magnetic field B_e and the field at the location of interest B, $A = P_\perp/P_\parallel - 1$ is the anisotropy and A_e is the value of anisotropy at the equatorial plane, $P_{\perp e}$ and $P_{\parallel e}$ are the perpendicular and parallel pressures at the equatorial plane. The average pressure at the equatorial plane, defined as $P = (2P_{\perp e} + P_{\parallel e})/3$, assumes a Gaussian distribution as $P(\rho) = P_0 \exp\left[-(\rho - \rho_0)^2/2\sigma_\rho^2\right]$, where P_0 and ρ_0 are the pressure peak and the location of the pressure peak, σ_ρ is the width of the pressure distribution in ρ coordinate. Such pressure distribution is used to approximately represents the thermal pressure of the ring current, and we choose the location of pressure peak ρ_0 corresponding to $L_0 = 5$, near the center of the ring current. The value of P_0 is set to $\beta_0 P_{mag0}$, where P_{mag0} is the magnetic pressure of the dipole field at L_0 and β_0 is the initial β (the average β which equals to $(2\beta_\perp + \beta_\parallel)/3$) at L_0. Thus, the initial distribution

of pressure in our model can be determined by the four parameters: L_0, σ_ρ, β_0 and A_e. The $\beta_0 = 0$ case represents the cold plasma case (dipole field), and the $A_e = 0$ case represents the isotropic pressure case. We use the Earths dipole field as the initial magnetic field and the boundary magnetic field at the inner, outer, and high-latitude boundaries. For the initial condition, the thermal pressure gradient and the $\mathbf{J} \times \mathbf{B}$ force are not balanced. The magnetic field can be updated through iteration by solving Equation (3.8) for ψ in our model, in order to achieve convergence toward an equilibrium state. A criterion for the convergence is $D = \Sigma_{i,j}|[\psi_{i,j}(n) - \psi_{i,j}(n-1)]/\psi_{i,j}(n-1)| < 2 \times 10^{-5}$, where i, j are the grid indices for the ρ and θ directions, respectively, n is the step number of the calculation, and D measures the relative difference between the current step n and the previous step $(n-1)$.

Figure 3.2 shows the model result for $\beta_0 = 0.6$, $A_e = 0.4$, $L_0 = 6$, and $\sigma_\rho = 0.05$ (we choose $L_0 = 6$ here to exhibit the result more clearly). Figure 3.2a shows the topology of magnetic field lines in the meridian plane, where the blue dashed lines stand for the initial dipole field and the red solid lines stand for the final self-consistent magnetic field. The region in the black box is zoomed in. One can see that the field lines compress from L_0 to the inner boundary and expand from L_0 to the outer boundary, which is caused by the presence of plasma thermal pressure. As a result, magnetic pressure is decreased (sparser field lines) in the region with finite plasma pressure. Figure 3.2b shows the distribution of $P_\perp$. Note that equatorial pressure is initially a Gaussian function of ρ, but spatial variation of the pressure evolves as the iteration goes forward, because of the dependence of ρ on spatial position. In general, the pressure peak tends to shift outward, the extent of which depends on the value of β_{peak} (β_{peak} is the maximum average β value in the equatorial plane). For this case of $\beta_0 = 0.6$, P_{perp} still peaks near $L_0 = 6$. For each field line, the perpendicular pressure maximizes at the equator and decreases toward higher latitudes (λ) (Figure 3.2b). The variation of the parallel pressure distribution versus L and λ is similar to that of perpendicular pressure (not shown). The field line variation of $P_\perp$, $P_\parallel$ and A can

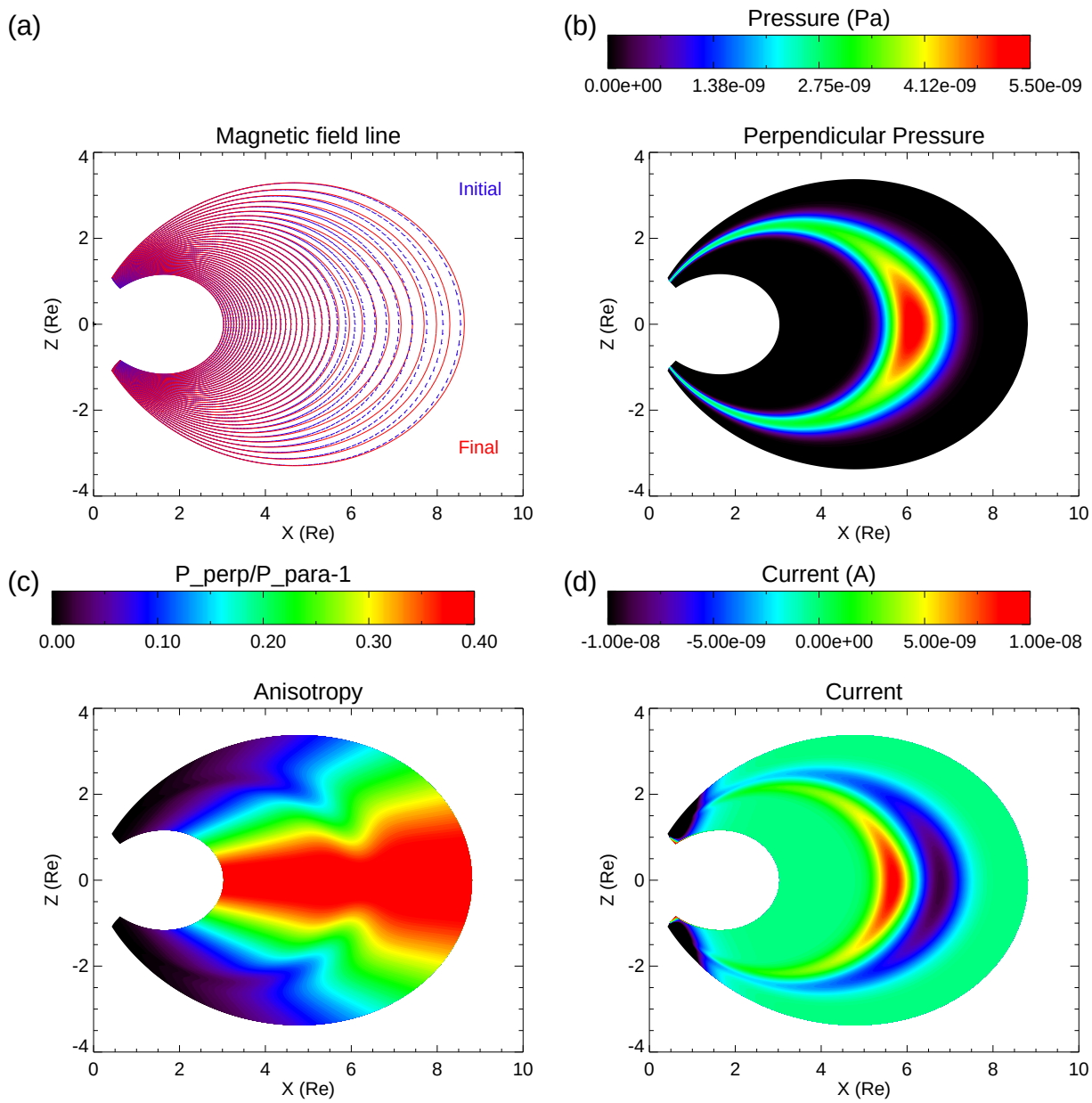

Figure 3.2. The self-consistent equilibrium model for $\beta_0 = 0.6$, $L_0 = 6$, $\sigma_\rho = 0.05$, $A_e = 0.4$. (a) The magnetic field lines in the noon-midnight meridian plane with a zoom in view of the black box region, where blue dashed lines represent dipole field lines and red solid lines represent the modeled field lines. (b) The distribution of the perpendicular thermal pressure. (c) The distribution of the pressure anisotropy. (d) The distribution of the azimuthal current (positive eastward and negative westward).

be obtained from Equations (3.9)-(3.11), respectively. S varies from 1 at the equator to a smaller positive value at higher latitudes. For $A_e > 0$, all three parameters decrease with latitude. For $A_e = 0$, $P_\perp = P_\parallel = P_{\perp e} = P_{\parallel e}$ and $A = 0$ throughout the field line. For $A_e < 0$, $P_\perp$ and $P_\parallel$ increase with latitudes and A increases toward 0 (isotropic). Figure 3.2c shows the distribution of pressure anisotropy ($A_e > 0$). Along a field line, the anisotropy approaches zero as λ increases. The contour lines of anisotropy bend toward the equator near L_0, meaning that the anisotropy approaches zero faster at the higher-pressure region. Figure 3.2d shows the distribution of azimuthal current, which exhibits a two-cell structure around the peak pressure point. This azimuthal current is given by the curl of the magnetic field, which is no longer zero for the nondipole field, and the $\mathbf{J} \times \mathbf{B}$ force is created to balance the pressure gradient force in a quasi-equilibrium condition. Note that artificial current appearing at the high-latitude regions is associated with numerical errors when evaluating field line curls there, which does not affect the calculation below.

To isolate the effect of β_0 and A_e on magnetic field dip (Section 3.3) and compressional poloidal mode (Section 3.4.2), we create a pool of equilibria with fixed $L_0 = 5$, $\sigma_\rho = 0.05$ and different β_0 and A_e. The values of β_0 vary from 0.1 to 0.7, with a spacing of 0.1 for $0.1 \leqslant \beta_0 \leqslant 0.5$, 0.05 for $0.5 \leqslant \beta_0 \leqslant 0.6$, and 0.02 for $0.6 \leqslant \beta_0 \leqslant 0.7$. The values of A_e vary from -0.5 to 2.0 with a spacing of 0.1 for $-0.5 \leqslant A_e \leqslant 0.0$ and 0.2 for $0.0 \leqslant A_e \leqslant 2.0$. The pool of the model results is shown by Figure 3.3 with equilibria categorized into two groups: stable equilibria (circles) and unstable equilibria (triangle and diamond symbols). The diamond and triangle symbols indicate cases unstable to the firehose and mirror instabilities, respectively, which are excluded from our equilibrium pool. These two types of instabilities are charactered by the firehose instability parameter σ and mirror instability parameter τ defined as follows:

$$\sigma = 1 + \frac{1}{2}(\beta_\perp - \beta_\parallel) \tag{3.12}$$

$$\tau = 1 + \beta_\perp(1 - \frac{\beta_\perp}{\beta_\parallel}) \tag{3.13}$$

$\sigma < 0$ and $\tau < 0$ represent Firehose and Mirror instabilities respectively [Chen and Hasegawa, 1991; Chan et al., 1994] and the boundaries of $\sigma = 0$ and $\tau = 0$ are labeled by the two dash-dotted lines (left one for σ and right one for τ). In Figure 3.3, the x axis is A_e, the y axis is peak $\beta_\perp$ of the final equilibrium state (β_{peak}). The color of the circles in Figure 3.3a represents the L shell corresponding to the β peak, and in Figure 3.3b represents the width of β_{peak} ΔL, measured by the full width at half maximum β distribution. From this pool, we find that both the β_{peak} and L_{peak} increase compared with the initial values of β_0 and $L_0 = 5$, as the result of the reduction of magnetic field strength at pressure peak. The field line with peak thermal pressure moves outward to a lower magnetic pressure region, which leads to the increase of β_{peak} and L_{peak}. Although the upper limit of β_0 is chosen to be 0.7, the largest β_{peak} can reach up to ~ 3, which is large enough to cover the usual β values in the inner magnetosphere. The variation of L_{peak} (5.1-5.4) is not significant and the variation of ΔL is also small (from $\sim$0.68 to $\sim$0.72). Therefore, the data of this pool can be used to isolate the effect of β_{peak} and A_e respectively.

$\sigma < 0$ and $\tau < 0$ represent firehose and mirror instabilities, respectively [Chen and Hasegawa, 1991; Chan et al., 1994], and the boundaries of $\sigma = 0$ and $\tau = 0$ are labeled by the two dash-dotted lines. In Figure 3.3, the x axis is A_e, and the y axis is peak average $\beta_\perp$ of the final equilibrium state (β_{peak}). The color of the circles in Figure 3.3a represents the L shell corresponding to the β_{peak} and in Figure 3.3b represents the full width (ΔL) of half β_{peak}, measured by the full width at half maximum of the β distribution. From this pool, we find that both the β_{peak} and L_{peak} increase compared with the initial values of β_0 and $L_0 = 5$, as the result of the reduction of magnetic field strength at the pressure peak. The field line with peak thermal pressure moves outward to a lower magnetic pressure region, which leads to the increase of β_{peak} and L_{peak}. Although the upper limit of β_0 is chosen to be 0.7, the largest β_{peak} can reach up to $\sim$3, which is large enough to cover the usual β values in the inner magnetosphere. The variation of L_{peak} (5.1 to 5.4) is not significant, and the

variation of ΔL is also small ($\sim$0.68 to $\sim$0.72). Therefore, the data of this pool can be used to isolate the effect of L_{peak} and A_e, respectively.

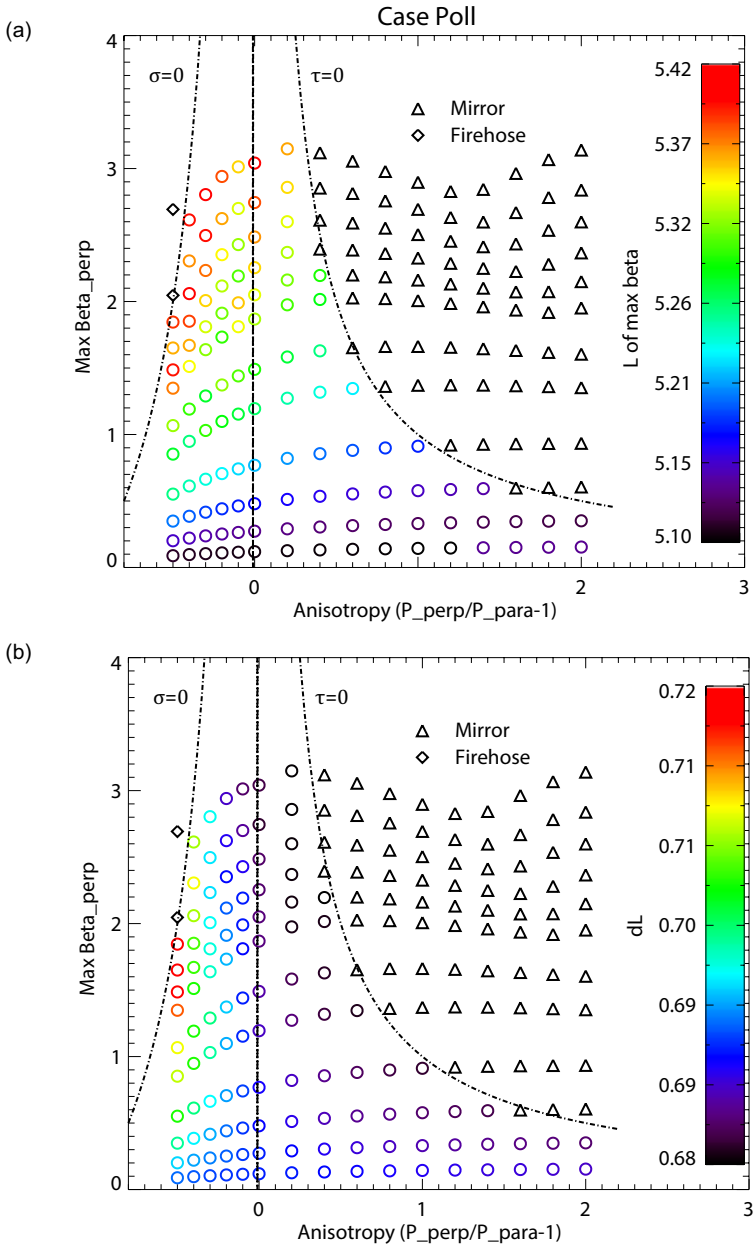

Figure 3.3. The pool of calculated self-consistent magnetic field for cases with fixed $L_0 = 5$, $\sigma_\rho = 0.05$ but different combination of β_0, A_e.
The x axis is equatorial anisotropy A_e, and the y axis is the maximum plasma average β. The color of the circles denotes the location L_{peak} of the peak β in Figure 3.3a and the full width ΔL at half maximum of β in Figure 3.3b. The diamond and triangle symbols represent the equilibria unstable to firehose and mirror instabilities, respectively.

3.3 Magnetic Field Dip Formation

Here we investigate the effects of plasma β and plasma anisotropy on the ambient magnetic field variation and the condition of the magnetic dip formation. The calculated self-consistent magnetic field is compared with the dipole field near the pressure peak region. The comparison at the equatorial plane for isotropic ($A_e = 0$) cases with different values of β_{peak} is shown by Figure 3.4. Figure 3.4a shows the variations of magnetic field strength for different cases and Figure 3.4b shows the corresponding β variations. The magnetic field strength decreases compared to the dipole field at the inner edge of the pressure peak and reaches a minimum near the pressure peak then starts to increase to approach the strength of dipole field at the large L region. The reason for the decrease of the magnetic field strength has been explained by the "diamagnetic" effect of finite plasma pressure, that is, the magnetic field lines expand near the center of the plasma pressure peak. The magnetic field strength larger than dipole field at large L ($L > 5.7$) is caused by the fixed dipolar field at the outer boundary, which leads to accumulation of field lines outside the high-pressure region. In reality, the field strength in this region should be smaller than the dipole field. Nonetheless, this unrealistic part of the magnetic field is not critical in our analysis. When the thermal pressure is large enough, a magnetic field strength dip with reversed field strength gradients nearby is formed near the peak pressure location. For a uniform magnetic field, the dip will exist whenever there is a localized thermal pressure that produces the magnetic field gradient. But in this dipolar-like model, the formation of the dip needs a critical value of β because the dipole field itself has a magnetic gradient and the gradient caused by the additional thermal pressure must be large enough to overcome the gradient of dipole field in order to produce the dip. For isotropic cases, the critical β for the dip formation is about 0.77 and the depth of the dip (the maximum difference between the dipole field strength and the dip strength) increases with β (Figure 3.4).

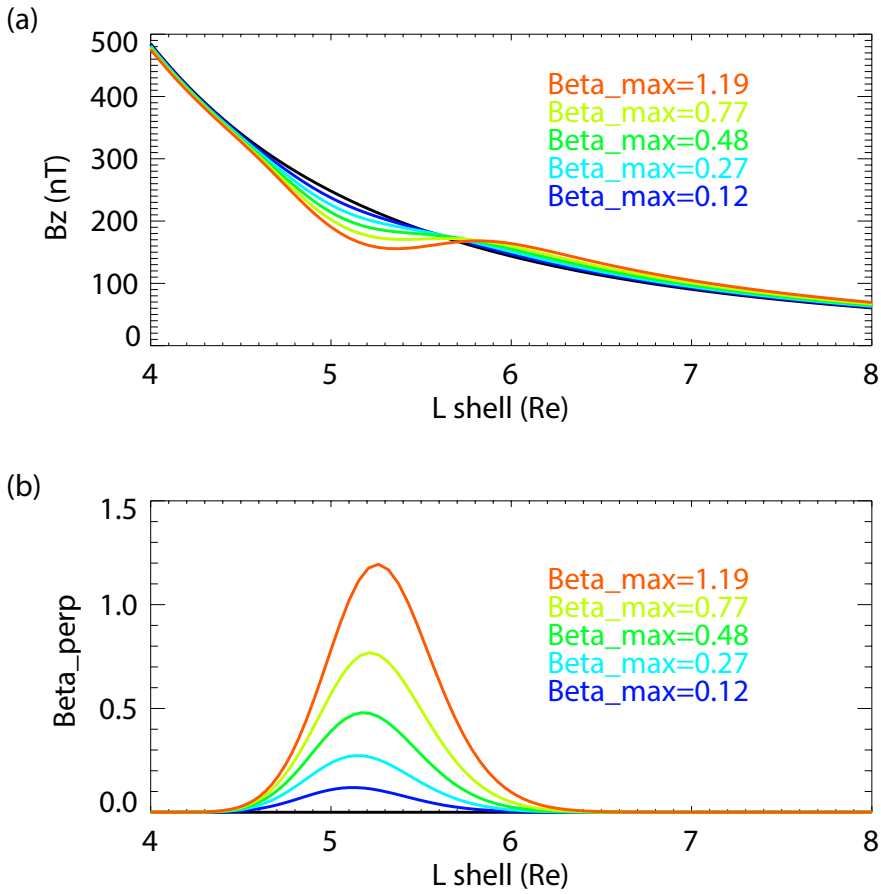

Figure 3.4. The variation of (a) magnetic field and (b) average β on the equator as a function of L shell for isotropic equilibrium ($A_e = 0$) with $L_0 = 5$ and $\sigma_\rho = 0.05$.
Different colors denote different values of maximum β. The black line in Figure 3.4a shows the dipole magnetic field variation.

Now we analyze the effect of the pressure anisotropy A_e on the magnetic dip and plot the depth of magnetic field dip versus A_e and β_{peak} in Figure 3.5. In order to increase the accuracy of the critical β estimation, we add additional cases between $\beta_0 = 0.3$ and $\beta_0 = 0.5$, which are not included in our pool (Figure 3.3). One can see that a larger value of β_{peak} tends to produce a larger magnetic dip. A critical value of β ($\sim 0.6 - 0.7$) is required for the magnetic dip formation. The β threshold to form a dip is almost independent of A_e, although the magnetic dip increases slightly for a more positive A_e. The effect of A_e can be explained

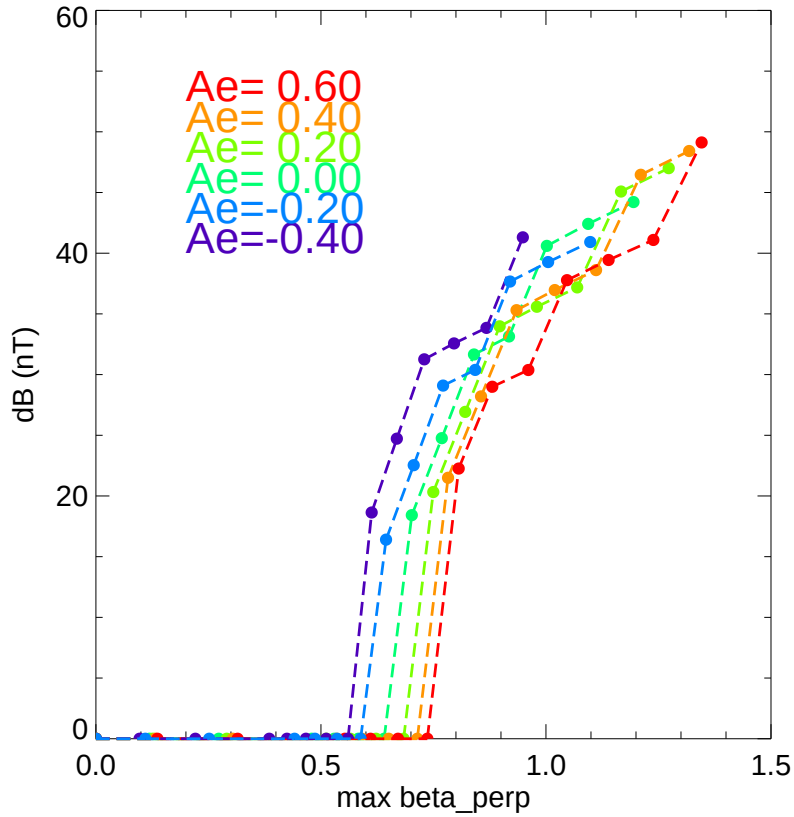

Figure 3.5. The effects of the maximum average β and the equatorial anisotropy A_e on depth of the magnetic field dip dB.
Different colored lines denote the different values of A_e.

by the right-handed side of Equation (3.8), where the contribution of perpendicular pressure to the diamagnetic current is greater than that of parallel pressure.

3.4 Eigenmode Analysis of FLR

3.4.1 Fundamental Equation for Second Harmonic

As concluded by Chen and Hasegawa [1991] and observed by Takahashi [1988], the most unstable mode or the most easily excited mode FLR is the second harmonic, which is the lowest-frequency antisymmetric mode. For this mode, the $\delta E_\perp$ and $\delta B_\parallel$ components have

odd symmetry with respect to the equator, while the $\delta B_\perp$ components have even symmetry. For this study, we focus on analyzing the second harmonic of the compressional poloidal mode. We adopt the simple variation $\exp(im_\phi\phi - i\omega t)$ for the eigenmode as in Equation (48) of Chan et al. [1994]:

$$B\frac{\partial}{\partial l}(\frac{\sigma^2}{B}\frac{\partial\delta\psi}{\partial l}) + \frac{\omega^2 k_\perp^2}{V_A^2}\delta\psi + \frac{\mu_0}{B^2}\Omega_\kappa \mathbf{e_k}\cdot\widetilde{\nabla}(P_\parallel + \frac{\sigma}{\tau}P_\perp)\delta\psi = 0, \tag{3.14}$$

where l is the length along the field line. The boundary condition is assumed to be $\delta\psi(l_{min}) = \delta\psi(l_{max}) = 0$, where l_{min} and l_{max} stand for the two ends of the field line. The first term represents field line bending, the second term represents the cold plasma inertia, and the third term is the effect of thermal pressure gradients. Note that when thermal pressure is ignored and the variations of magnetic field and Alfvén speed vanishes, the Alfvénic mode can be recovered. $k_\perp$ is the perpendicular wave number, ω is the wave angular frequency, $\widetilde{\nabla} = \nabla\psi(\partial/\partial\psi)$ is the gradient along ψ, $\mathbf{e_k} = \mathbf{k}_\perp \times \mathbf{b}$, $\Omega_k = \mathbf{e_k}\cdot\kappa$. $\kappa = \mathbf{b}\cdot\nabla\mathbf{b}$ is the curvature of the magnetic field, and $V_A = B/\sqrt{\mu_0\rho}$ is the Alfvén speed, where ρ is the mass density and σ and τ are parameters for the firehose and mirror instabilities. The first-order quantity $\delta\psi \sim \exp[(im_\phi\phi - i\omega t)]$ is interpreted as the potential function for the Alfvénic wave components, where ϕ is azimuthal angle and m_ϕ is the azimuthal mode number. This equation has neglected the kinetic resonant effects and is derived under the following assumptions: (1) the gyrokinetic orderings $\omega \ll \omega_{ci}$ (ion cyclotron frequency) and $k_\perp \gg k_\parallel \sim 1/R_E$, (2) drift and bounce resonant effects are ignored, and (3) $\delta E_\parallel = 0$, as in the ideal MHD approximation. In order to analyze the most unstable modes, another assumption $k_\phi^2 \gg k_\psi^2$ or $k_\perp^2 \approx k_\phi^2 \equiv m_\phi^2/R^2$ is added in the following analysis, where R is the radial distance from the Earth in a cylindrical coordinate system. The third term on the left-hand side is the anisotropic ballooning-interchange term, and the direction of the factor $\Omega_k\mathbf{e_k}$ is always earthward, which is independent of the coordinate system.

The eigenmode equation for the linearized quantity $\delta\psi$ requires the operator $\partial/\partial l$ along a field line and zeroth-order quantities B, $\widetilde{\nabla}(P_\parallel + (\sigma/\tau)P_\perp)$ and $\Omega_k\mathbf{e_k}$ and V_A are needed. We

can adopt the result of our pressure equilibrium model calculation to analyze the eigenmode of the second harmonic poloidal mode. The pressure equilibrium model outputs the magnetic field $\mathbf{B}$ and thermal pressure $P_\perp$ and $P_\parallel$ distributions along each magnetic field line and thus the instability parameters σ and τ, the magnetic field curvature $\Omega_k \mathbf{e_k}$ and pressure gradient $\widetilde{\nabla}(P_\parallel + (\sigma/\tau)P_\perp)$ terms. For the Alfvén speed term, the distribution of mass density ρ_m along the field line is assumed to be $\rho_m(\lambda) = n_0 m_i \cos^{-2m}(\lambda)$ [Cummings et al., 1969], where n_0 is the number density and is set to be $10^7 m^{-3}$, m_i is the average ion mass and is set to be twice the proton mass, and m is the plasma density index which is chosen to be 4 for our analysis. The factor $k_\perp$ has been approximated to be equal to $k_\phi = m_\phi/R$, and m_ϕ is chosen to be 100 according to the observations of the transverse wavelengths of magnetospheric hydromagnetic waves [Takahashi, 1988]. As noted by Chan et al. [1994], the results of eigenvalues become independent of m_ϕ when $k_\phi \gg k_\psi$.

After calculating all the zeroth-order quantities, we can solve the eigenmode equation for the eigenfrequency f $(= \omega/2\pi)$ for each field line resonance and obtain the potential function $\delta\psi$ variation along each field line. Then the components of magnetic and electric fields can be obtained as follows [Chan et al., 1994]:

$$\delta B_\parallel = \frac{\mu_0 c}{\tau \omega B^2}(\mathbf{e_k} \cdot \widetilde{\nabla} P_\perp)\delta\psi, \tag{3.15}$$

$$\delta B_\psi = \frac{k_\phi c}{\omega}\frac{\partial \delta\psi}{\partial l}, \tag{3.16}$$

$$\delta B_\phi = \frac{B}{k_\phi}\frac{\partial}{\partial l}\frac{\delta B_\parallel}{B}, \tag{3.17}$$

$$\delta E_\parallel = 0, \tag{3.18}$$

$$\delta E_\psi = -\frac{\omega}{k_\phi c}\delta B_\parallel, \tag{3.19}$$

$$\delta E_\phi = -i k_\phi \delta\psi. \tag{3.20}$$

where c is the light speed.

3.4.2 The Effect of Plasma β and Anisotropy on Second Harmonic Compressional Poloidal Mode

Applying the self-consistent magnetic field obtained from the pressure equilibrium model to the eigenmode analysis of compressional poloidal modes for the second harmonic, we can solve the eigenfrequency and the complex amplitudes of magnetic and electric field components for each field line resonance. Figure 3.6 shows the result of eigenmode analysis for the case with $\beta_0 = 0.4$ and $A_e = 0.4$. Figure 3.6a shows the solution of f^2 (the blue line) from $L = 4.5$ to $L = 6.5$, while the black line represents the square of eigenfrequency for the dipole field (f_0^2) without thermal pressure for comparison. Figure 3.6b shows the variation of equatorial average P ($P = (2P_\perp + P_\parallel)/3$) in the same L range. The peak location of P is at about $L = 5.2$. The eigenfrequency tends to decrease as L increases for both cold and thermal plasma cases as expected from a longer field line length at larger L. The frequency f for the thermal case is larger than f_0 at the inner edge of the pressure peak then becomes equal to f_0 at the pressure peak and becomes smaller than f_0 at the outer edge of the pressure peak. Over the region of very low thermal pressure ($L >\sim 6$), the eigenfrequency is about f_0. This change in eigenfrequency across the pressure peak is caused by the pressure gradient in the anisotropic ballooning-interchange term of Equation (3.14). At the inner edge, the pressure gradient factor $\widetilde{\nabla}(P_\parallel + (\sigma/\tau)P_\perp)$ points outward ($+\mathbf{r}$) direction so the anisotropic ballooning-interchange term is negative, which results in the enhancement of f^2. Conversely, the pressure gradient at the outer edge points inward, leading to a decrease of f^2. At the peak thermal pressure and over low thermal pressure regions, the pressure gradient is negligible and the frequency difference vanishes. Figures 3.6c-3.6e show the variations of three magnetic field components versus the latitude along field lines at the inner edge, the peak, and the outer edge of the pressure distribution, respectively. The red, green, and blue lines denote the parallel ($\delta B_\parallel$), azimuthal (δB_ϕ) and radial (δB_ψ) components of the magnetic field, respectively. The components are normalized by the amplitude of radial

component (the $|\delta B_\psi|$ at the end of field line). The compressional mode (parallel) component exists at the inner and outer edges, where large thermal pressure gradients exist, while the compressional component vanishes at the peak point and very low thermal pressure regions (not shown), where the thermal pressure gradient is small. The amplitude of the parallel component is comparable to the radial component near the equatorial region, especially at the outer edge. The parallel component $\delta B_\parallel$ is related to the pressure gradient $\mathbf{e_k} \cdot \widetilde{\nabla} P_\perp$ as shown by Equation (3.15), from which we expect that the parallel component only exists at the inner and outer edges with nonnegligible pressure gradients. It should be noted that the phase of the parallel component shifts by 180°across the pressure peak. This is caused by the opposite signs of $\mathbf{e_k} \cdot \widetilde{\nabla} P_\perp$ at these two regions.

In order to isolate the effects of β_{peak} and A_e on the second harmonic compressional poloidal mode, respectively, we compare the results from multiple cases. For the effect of β_{peak} we choose three different β_{peak} values 0.12, 0.48, and 1.19 and the same $A_e = 0.4$. Figures 3.7a and 3.7b show the effects of β_{peak} on the difference between f^2 and f_0^2 (normalized by f_0^2 as $(f^2 - f_0^2)/f_0^2$) and the maximum amplitude of compressional component along a field line (normalized by the radial component amplitude at the ionospheric foot points). From Figure 3.7a, eigenfrequency increases at the inner edge and decreases at the outer edge. The eigenfrequency difference from f_0 increases as β_{peak} increases. For a large $\beta_{peak} = 1.19$ as shown by the red line, $(f^2 - f_0^2)/f_0^2 \sim -0.75$ at the outer edge, that is, $f \sim 0.5 f_0$, meaning that the second harmonic eigenfrequency is close to the frequency of fundamental harmonic using cold plasma in a dipole field. This frequency change due to finite pressure is significant and should be taken into account when determining the harmonic number of field line resonance in the observations. Figure 3.7b shows that a larger value of β_{peak} can increase the magnetic field compressional component amplitude. One can also see that the compressional amplitude is larger at the outer edge than inner edge in all cases. To isolate the effect of A_e, we choose among the equilibrium pool three cases having similar β_{peak}

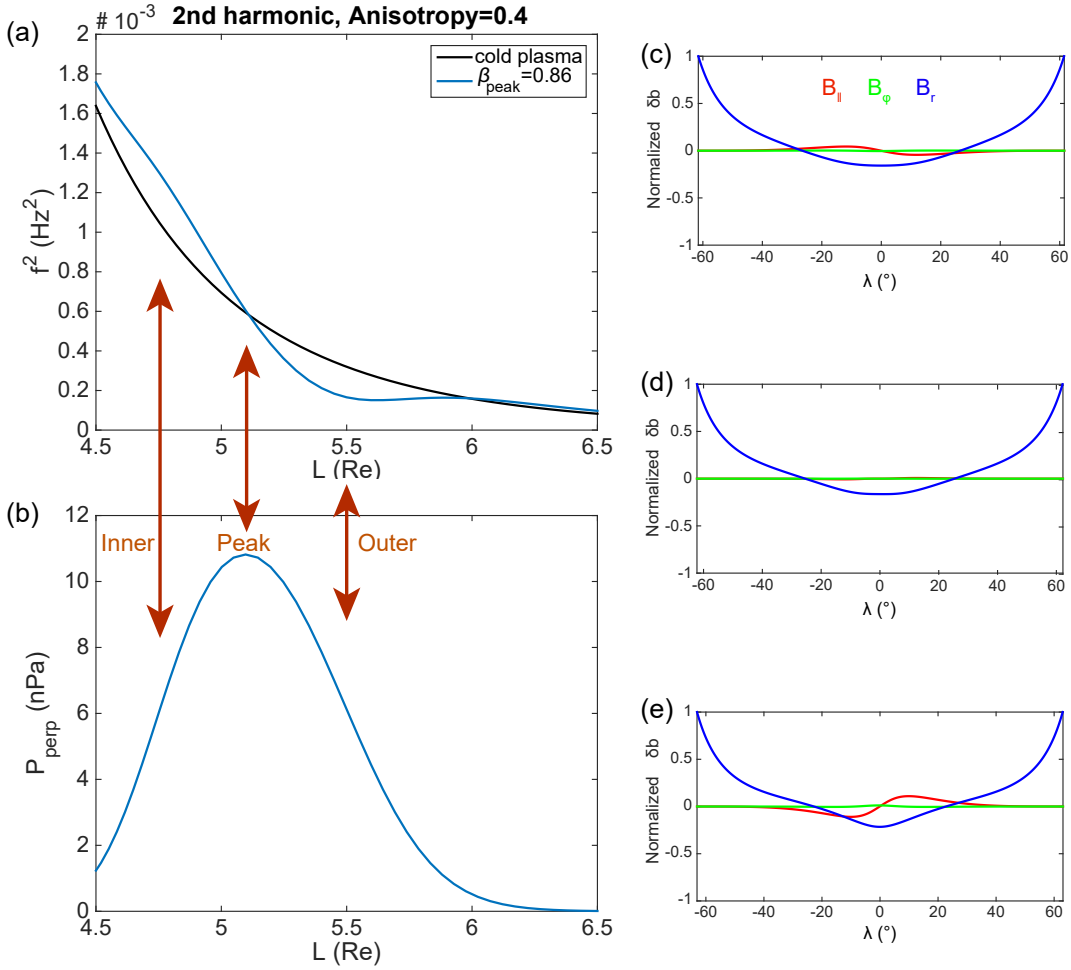

Figure 3.6. The result of eigenmode analysis for the case with $L_{peak} = 5$, $\sigma_\rho = 0.05$, $\beta_0 = 0.4$, and $A_e = 0.4$.
(a) The eigenfrequency squared variation as a function of L shell of second harmonic field line resonance for the modeled equilibrium with $L_{peak} = 5$, $\sigma_\rho = 0.05$, $\beta_0 = 0.4$, and $A_e = 0.4$. The black line stands for the cold plasma solution. (b) The average pressure variation versus L shell. (c-e) The variation of the three magnetic field components of the eigenmodes versus the latitude (λ) along the field line at the inner edge (Figure 3.6c), at the pressure peak (Figure 3.6d), and at the outer edge (Figure 3.6e), respectively. The red, blue, and green lines represent the parallel ($\delta B_\parallel$), radial (δB_ψ), and azimuthal (δB_ϕ) components, respectively. All the components are normalized by the radial component amplitude at the foot point of the field line.

($\sim 0.76 - 0.77$) but different A_e values: -0.2, 0, and 0.4. The comparison of eigenmode analysis is shown in Figures 3.7c and 3.7d. The decrease of A_e leads to a larger deviation of eigenfrequency from the cold plasma value f_0 (Figure 3.7c), in particular, at the outer edge. As A_e decreases, f^2 tends to decrease at the outer edge (toward instability) but the increase at the inner edge (more stable). The decrease in A_e also leads to the enhancement of the compressional component at the inner edge and a weaker enhancement of the compressional component amplitude at the outer edge (Figure 3.7d).

3.4.3 Critical Condition of Alfvén-Ballooning Instability

We have demonstrated that at the outer edge of the thermal pressure peak, the eigenfrequency square f^2 is smaller than that of cold plasma condition, and this difference can be enlarged by larger β_{peak} and smaller A_e. When the difference is large enough, f^2 will become negative and f becomes imaginary, which allows waves to grow in time (instability). Therefore, $f^2 = 0$ is the instability condition due to the pressure gradient in the high $k_\perp$ limit, and this instability is known as the Alfvén-ballooning instability. The dependence of the critical condition ($f^2 = 0$) on β_{peak} and A_e are investigated using our equilibrium pool (Figure 3.3). For each case in the pool except those subject to firehose and mirror instabilities (marked by diamond and triangle symbols in Figure 3.3), linear eigenmode analysis is performed for every field line. When there is a solution for second harmonic mode with $f^2 < 0$ for any field line, we mark the corresponding case as the equilibrium subject to Alfvén-ballooning instability. Otherwise, the case is stable to that instability. We mark each case in the pool in Figure 3.8 in the domain of the pressure anisotropy A_e (horizontal axis) and $\beta_{peak}/\Delta L$ (vertical axis, a measure of the pressure gradients) using four different categories: diamond symbols for firehose instability, triangle symbols for mirror instability, red circles for Alfvén-ballooning instabilities, and blue circles for stability. Note that the ratio $\beta_{peak}/\Delta L$ is primarily determined by β_{peak} in our pool because the ΔL value is approximately constant at $\Delta L \simeq 0.7$.

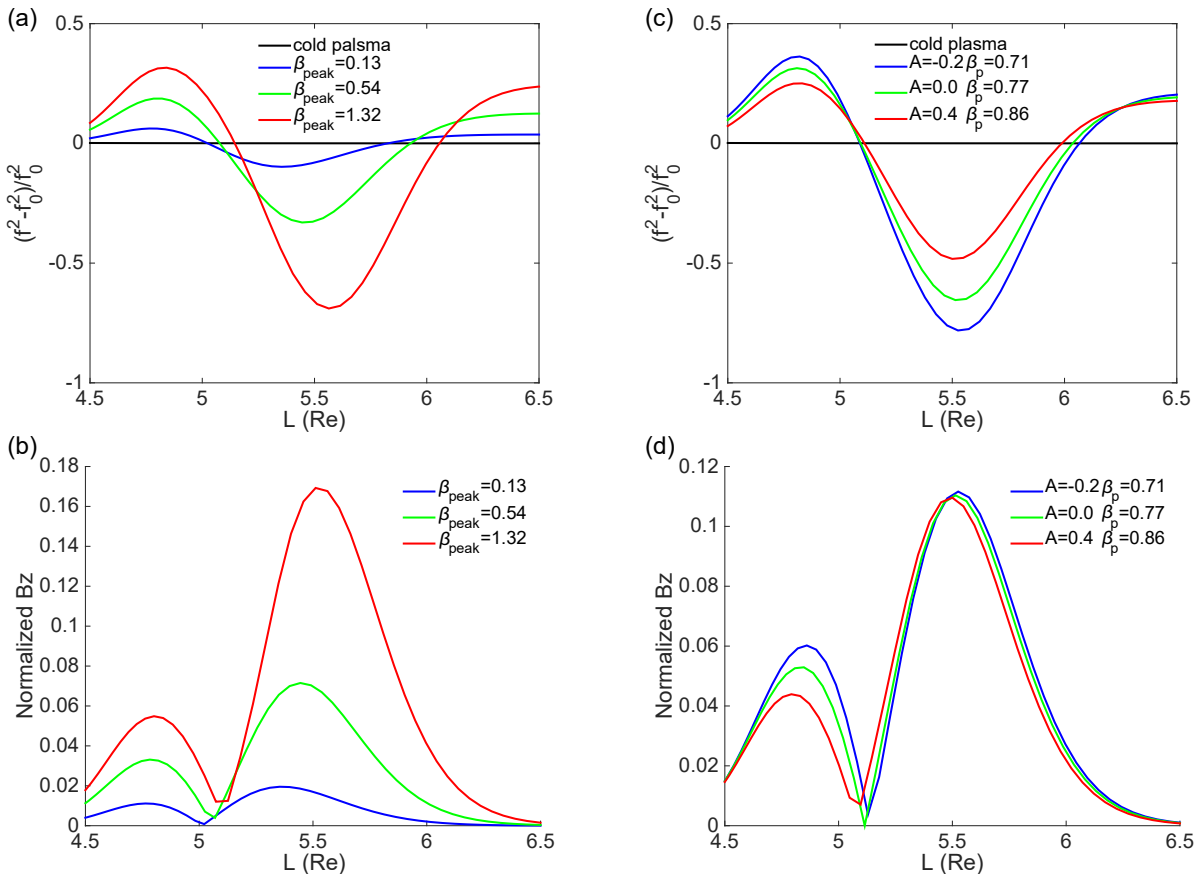

Figure 3.7. The effects of β_{peak} and A_e on relative difference of eigenfrequency and normalized B_z component for second harmonic field line resonance.
(a and c) The variation of normalized frequency difference $(f^2 - f_0^2)/f_0^2$, f_0 (f_0 is the frequency for cold plasma case) versus L shell. (b and d) The variation of normalized $B_{\|}$ (normalized by the max B_ψ component at the ionospheric foot point) from the inner edge to the outer edge of the thermal pressure. Figures 3.7a and 3.7b show the effects of different β_{peak}. Figures 3.7c and 3.7d show the effects of A_e.

A clear boundary between blue and red circles is marked by the black line, representing the criteria for the Alfvén-ballooning instability. At very low $\beta_{peak}/\Delta L$ ($\ll 1$), the plasma is stable for all A_e values. The instability occurs when $\beta_{peak}/\Delta L$ reaches a value larger than 1 for the smallest anisotropy value $A_e = -0.5$. As A_e increases, the $\beta_{peak}/\Delta L$ threshold for the instability increases gradually and requires at least $\sim$2.5 for $A_e = 0.2 - 0.4$. Over the regime of $A_e > 0.4$ the mirror instability takes over, while the firehose instability dominates over the regime of large β ($\beta_{peak}/\Delta L > 3.5$) and small A_e ($\sim$-0.5). The instability criteria exhibit a similar trend to Chan et al. [1994]'s results in that the threshold β increases as A_e increases, although their results are applicable only for low β conditions.

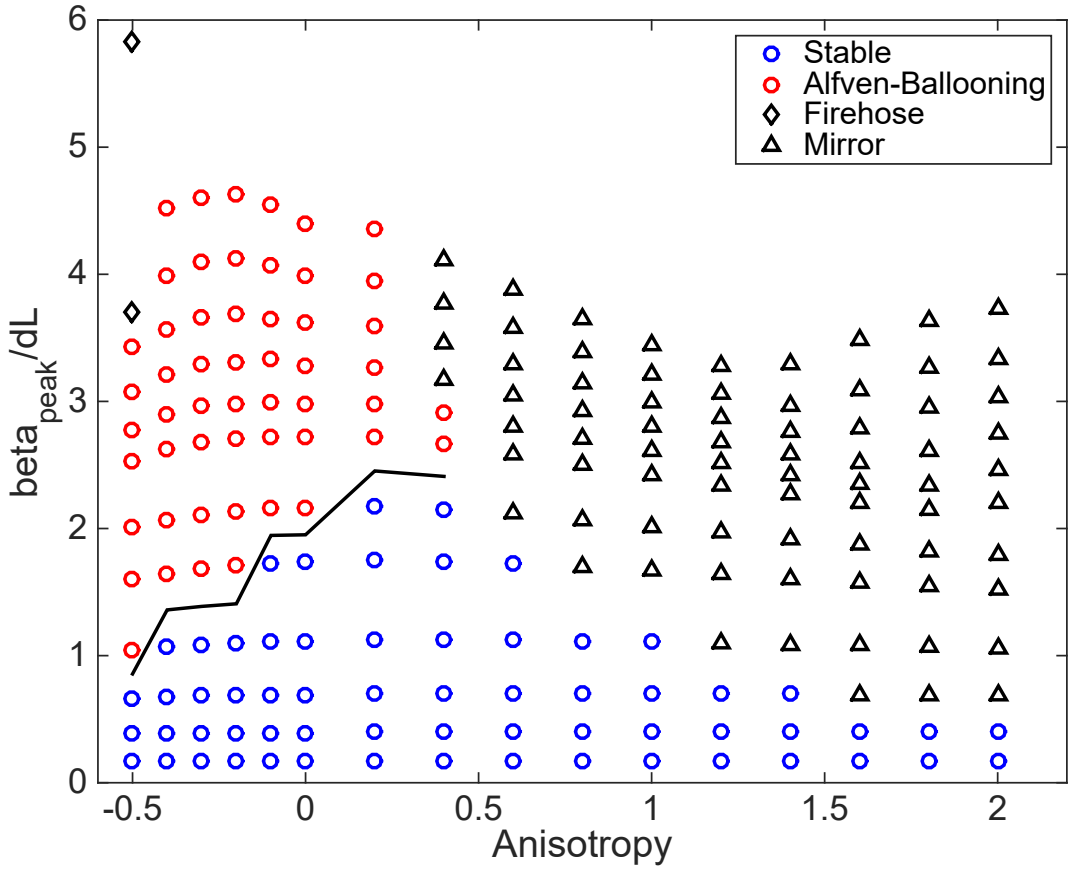

Figure 3.8. Instability in the regime of $\beta_{peak}/\Delta L$ (ΔL is full width at half maximum β) and the equatorial anisotropy A_e.
The blue circles denote stable equilibrium, and the red circles denote the equilibria unstable to Alfvén-ballooning instability. Diamond and triangle symbols denote equilibria unstable to firehose and mirror instabilities, respectively.

3.5 Conclusions and Discussion

In this study, we apply a self-consistent equilibrium model to simulate an axisymmetric magnetospheric magnetic field with a radially localized plasma pressure with a given pressure anisotropy. We create a pool of self-consistent magnetic field equilibria for cases with different combinations of maximum plasma β and anisotropy, which is later used to analyze the compressional second harmonic poloidal mode. We investigate the magnetic field change due to the localized plasma pressure and the effect of plasma pressure peak value and anisotropy on the eigenfrequency and the compressional component of second harmonic compressional poloidal modes. Finally, the critical condition for Alfvén-ballooning instability is evaluated for a range of β and A_e. Our results and conclusions are as follows.

1. The magnetic field dip forms near the high plasma pressure region with $\beta >\sim 0.6$. The formed magnetic dip becomes deeper for a larger plasma β. The threshold value of β for the magnetic dip formation is almost independent of A_e.

2. The eigenfrequency of the second harmonic compressional poloidal mode increases at the inner edge of the plasma pressure peak and decreases at the outer edge, compared with the eigenfrequency of the dipole field. At the pressure peak and over low-pressure regions, where the pressure gradient is small, the results are consistent with cold plasma theory.

3. The compressional component of the second harmonic compressional poloidal mode exists in both the inner and outer pressure edges but vanishes at the negligible pressure gradient regions. The amplitude of the compressional component at the outer edge is generally larger than that at the inner edge.

4. The β and anisotropy tend to have opposite effects on the second harmonic compressional poloidal mode. Higher β and smaller anisotropy tend to enlarge the compressional component amplitude at both inner and outer edges and increase (decrease) the eigenfrequency at the inner (outer) edge.

5. The critical condition for Alfvén-ballooning instability is calculated, and we find that a higher $\beta_{peak}/\Delta L$ threshold is required for higher A_e. The threshold value varies from $\beta_{peak}/\Delta L \sim 1$ when $A_e = -0.5$ to $\beta_{peak}/\Delta L \sim 2.5$ when $A_e = 0.2 - 0.4$ (with $\Delta L =\sim 0.7$).

A magnetic dip structure has been reported by Ukhorskiy et al. [2006], as a local magnetic minimum followed by a magnetic island (maximum) at larger L, which is caused by storm time ring current obtained from the TS05 model [Tsyganenko and Sitnov, 2005]. Further observational studies are needed to confirm the condition for the magnetic dip formation.

The FLR model in our study ignores wave-particle resonance and concentrates on the unstable modes corresponding to the Alfvén-ballooning instability. To analyze more general eigenmodes of a field line, we need to go back to the original gyrokinetic eigenmode equations of Chen and Hasegawa [1991], where the wave particle interactions are included. Significant deviation of the eigenfrequency from the cold plasma solution is found in a finite β plasma. Pressure anisotropy also influences the eigenfrequency. When using observed ULF periods to infer the mode number of a field line resonance, one should consider the effect of plasma β and anisotropy, especially during storm time when both are enhanced. A future study is planned to couple the FLR eigenmodes analysis with the 3-D kinetic ring current model RAM-SCB (Ring current-Atmosphere interaction Model with Self-ConsistentMagnetic field (B)) [Jordanova et al., 2010], which can help us make predictions for internally driven ULF waves of high azimuthal number in a global 3-D magnetosphere geometry including the storm time ring current.

CHAPTER 4

STATISTICAL STUDY OF CHORUS WAVES MODULATIONS BY BACKGROUND MAGNETIC FIELD AND PLASMA DENSITY

This chapter is based on a manuscript led by myself, L. Chen and W. Li, which is currently under preparation and will be submitted in July 2019.

4.1 Introduction

Whistler-mode chorus emissions in the magnetosphere are right-hand polarized electromagnetic waves originating near the geomagnetic equator outside the plasmapause [Tsurutani and Smith, 1977; Koons and Roeder, 1990; LeDocq et al., 1998; Lauben and Others, 2002; Santolík et al., 2003a]. The frequency range of chorus waves is usually separated into two bands: the lower band from 0.1 to 0.5 f_{ce} and the upper band from 0.5 to 0.8 f_{ce}, where f_{ce} is the equatorial electron cyclotron frequency [Tsurutani and Smith, 1974; Burtis and Helliwell, 1976, 1969]. The excitation of chorus waves are generally believed to involve with cyclotron resonance with anisotropic electrons that are usually injected from the plasma sheet into the inner magnetosphere during geomagnetic active times [Li and Others, 2010; Gao et al., 2014; Fu et al., 2014]. The interactions between chorus waves and particles are very important to the magnetospheric dynamics, including acceleration of electrons to relativistic energy level through energy diffusion [Horne and Thorne, 1998; Summers et al., 2002; Meredith et al., 2002; Horne and Others, 2005; Bortnik and Thorne, 2007b; Li et al., 2007] and precipitations of energetic electrons through pitch angle scattering [Lorentzen et al., 2001; O'Brien et al., 2004; Bortnik and Thorne, 2007b]. The precipitating electrons can penetrate into the atmosphere and produce both diffusive [e.g., Horne et al., 2003; Ni et al., 2008] and pulsating auroras [e.g., Davidson, 1990; Miyoshi et al., 2010; Nishimura et al., 2010; Jaynes et al., 2013].

Statistical studies indicate that the intensity and occurrence of chorus waves usually increase under higher geomagnetic activity level [Li et al., 2011c; Meredith et al., 2012; Agapitov et al., 2013] and around the dawn sector (between midnight and noon) [Tsurutani and Smith, 1974; Meredith et al., 2001; Meredith and Others, 2003a,b; Miyoshi and Others, 2003; Lyons and Others, 2005]. A recent study also shows a strong dependence of chorus intensity on the solar wind parameters: the intensity increases during the periods of higher solar wind speed and southward interplanetary magnetic field [Aryan et al., 2014]. The intensity of chorus waves is often observed as on-off discrete elements with a time scale about a tenth to a few tenths of seconds [Santolík et al., 2003a] and gathered together on a timescale from a few seconds to a few minutes, which can be modulated by the variations of background magnetic field and plasma density. One primary source of the oscillations of background magnetic field and plasma density is the Pc 4-5 ULF waves, which can be observed to modulate the chorus intensity in both large L-shell (8 to 12) region Li et al. [2011a] and inner magnetosphere [Xia et al., 2016]. In these two studies, the intensities of chorus waves show a positive correlation with plasma density and a negative correlation with the background magnetic field. Also, the negative correlation between chorus intensity and plasma density in the absence of ULF waves has also been observed Li et al. [2011b]. The modulated chorus emission could lead to modulated electron precipitation and the consequent pulsating aurora [Nishimura et al., 2010; Jaynes and Others, 2015]. Learning the chorus modulation is important to understand the excitation of whistler mode waves and the characteristics of pulsating aurora.

Despite previously existing studies on the chorus wave modulation, two important questions remain to be investigated. One is what kinds perturbations of background magnetic field and plasma density can modulate the chorus emission and the occurrences of different types of modulations. Another one is whether the intensity of modulated chorus is related to the amplitudes of the perturbations of background magnetic field and plasma density.

In this study, we use about 2 years' observations of three THEMIS satellites and 5.5 years' observations of two Van Allen Probes satellites to build a database of chorus modulation events and statistically study the relationships between the chorus emissions and perturbations of background magnetic field and plasma density. Section 4.2 introduces the THEMIS and Van Allen Probes satellites and corresponding instruments used. Section 4.3 describes the method to automatically identify the chorus modulation events and the rules to sort the events into different categories. Section 4.4 shows the proportions and spatial distributions of different types of modulation events and Section 4.5 gives a quantitative analysis of the relationship between the chorus intensity and amplitudes of background magnetic field and plasma density perturbations.

4.2 Spacecrafts and Instruments

The Time History of Events and Macroscale Interactions during Substorms (THEMIS) mission is a constellation of five identically-instrumented satellites with its mission started in February 2007. Three of the satellites (THA, THD, and THE) are inner probes in nearly equatorial orbits with apogees of 10-13 R_E and perigees below 2 R_E [Sibeck and Angelopoulos, 2008], which is suitable to observe chorus waves outside the plasmapause. The Fluxgate Magnetometer (FGM) [Auster et al., 2008] can provide the measurements of background magnetic fields and their low-frequency fluctuations (up to 64 Hz). The Electric Field Instrument (EFI) measures three components of electric fields [Bonnell et al., 2008] as well as individual sensor potentials, providing onboard and ground-based estimate of spacecraft floating potential and plasma density [Bonnell et al., 2008]. Also, waveforms and three-axis spectral measurements of ambient electric fields from DC up to 8 kHz can be measured by the EFI. The Search Coil Magnetometer (SCM) [Roux et al., 2008; Le Contel et al., 2008] provides the measurements of three components wave magnetic fields with a frequency range from 0.1 Hz to 4 kHz. The waveforms measured by EFI and SCM are digitized and processed

by the Digital Fields Board (DFB) [Cully et al., 2008] and finally transformed into two types of spectral products: filter bank data (FBK) and Fourier power spectra (FFT). The filter bank data are meant for survey-type monitoring of wave power, which has broad frequency bands and relatively low time resolution. The THEMIS wave data used in this study is the FBK spectra.

The Van Allen Probes (or Radiation Belt Storm Probes (RBSP)) [Mauk and Others, 2013] consist of two satellites with identical instruments and move along nearly similar near-equatorial highly elliptical orbits with perigee about 620 km and apogee about 5.8 R_E. The Electric and Magnetic Field Instrument Suite and Integrated Science (EMFISIS) [Kletzing and Others, 2013], equipped with a tri-axial fluxgate magnetometer (MAG) and a triaxial AC magnetic search coil magnetometer (MSC), can provide the measurement of wave magnetic field in frequency range between 10 Hz and 400 kHz as well as the background magnetic field. The Electric Field and Waves Suite (EFW) [Wygant and Others, 2013], consisting of 4 spin-plane electric field antennae and 2 spin-axis tubular extendable booms, can provide not only the measurement of the electric field but also estimation of cold plasma densities from 0.1 to 100 cm^{-3} from spacecraft potential. Also, the EMFISIS Upper Hybrid resonance (UHR) lines can help to calibrate empirical plasma density-potential formula and improve the measurement of plasma density [e.g., Li et al., 2011a].

4.3 Identification of Modulation Events

In this section, we first introduce automatic detection of the modulation events from the observations of THEMIS and Van Allen Probes. This process is achieved by calculating the correlation coefficient C_B between background magnetic field B_0 and logarithm value of chorus wave root mean square amplitude $\log B_w$ as well as the correlation coefficient C_N between plasma density N_0 and $\log B_w$. The value of B_w is the square root of the integration of the wave magnetic field spectral density over the frequency band from 0.1 to 0.8 electron

cyclotron frequency f_{ce}. Calculation of the correlation coefficients is only down over time intervals with high chorus wave amplitude outside the plasmapause. First, we only select data outside the plasmapause, which can be achieved by excluding the data points with corresponding plasma density larger than 10 cm^{-3}. Second, we select time intervals when the wave magnetic field B_w is at least twice the background value which is obtained from the median value of B_w. Third, for the intervals whose duration T_e is longer than 36 seconds, we calculate the two correlation coefficients C_B and C_N in the time window of $2T_e$ (extending the high B_w time interval backward and forward by 0.5 T_e respectively). Finally, the time intervals with absolute value of either C_B or C_N larger than 0.6 are recognized as modulation events.

According to the values of C_B or C_N, we sort the modulation events into 3 types and 8 subtypes. The three types are Type B with only high C_B absolute value; Type N with only high C_N absolute value; Type NB with both high C_B and C_N absolute values. For Type B and Type N, there are subtypes B+ and N+ with positive C_B and C_N values respectively and subtypes B- and N- with negative C_B and C_N respectively. For Type NB, the four subtypes are N+B+ with both positive C_B and C_N; N-B+ with positive C_B and negative C_N; N+B- with negative C_B and positive C_N; N-B- with both negative C_B and C_N. Eight representative events of the eight subtypes of modulation events observed by THEMIS are shown in Figures 4.1a-4.1h. For each subplot, the upper panel shows the variations of B_0 (blue line) and N_0 (red line) while the lower panel shows the magnetic power spectrum density (colored spectrum) and the variation of B_w (red line). The white solid, dashed and dot-dash lines denote the variations of f_{ce}, $0.5f_{ce}$ and $0.1f_{ce}$, respectively.

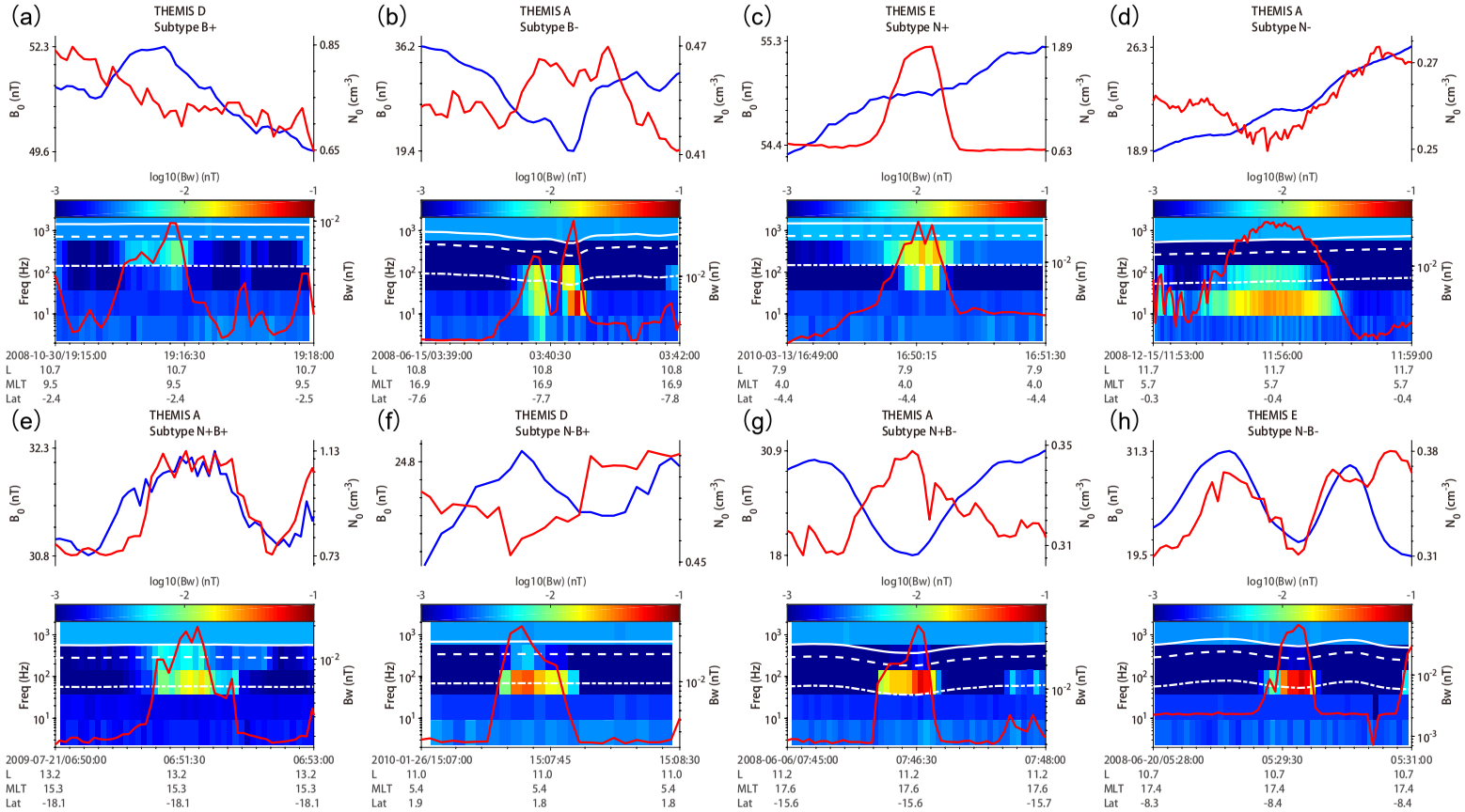

Figure 4.1. Representative events of the eight subtypes of chorus modulation events from the observations of THEMIS satellites.

For each subplot, the upper panel shows the variations of the background magnetic field (blue line) and plasma density (red line) and the lower panel shows the magnetic wave spectrum overplotted with the variation of chorus wave root mean square amplitude B_w (red line) as well as the variations of f_{ce}, $0.5f_{ce}$ and $0.1f_{ce}$ (white solid, dashed, dash-dot lines).

4.4 Distribution of Modulation Events

After surveying THEMIS observation from June 2008 to May 2010, totally 5338 modulation events are identified. For Van Allen Probes observation from September 2012 to May 2018, 3798 modulation events are identified. Now we sort these events into three types and eight subtypes and analyze the spatial distribution of the modulation events and the proportions of different types of modulation events. The panels on the left side of Figure 4.2 show those statistical results of the 5338 modulation events from the THEMIS observation. Figures 4.2a - 4.2d exhibit the spatial distribution of event numbers in the logarithm scale for all the modulation events, type B, type N and type NB events respectively. For the MLT distribution of type B and NB events which both involve the modulation effect of the background magnetic field, the modulation event number is the largest at the dawn sector and is the smallest near the midnight. There also exists a secondary peak in the dusk sector. However, for the type N events that involve only the modulation by plasma density, the MLT distribution is more uniform compared with that of type B and NB events. The radial distribution peaks at L = 11-12 and decreases as L decreases for type B and NB events, while for type N event, the radial dependence is weaker. For the region outside $L = 12$, few observations due to the limit of THEMIS orbit are made and thus information about the distribution of modulation events cannot be reliably obtained. Figure 4.2e shows the proportions of different types of events. The portions of the three types of events are 39.5%, 37.5% and 23% for type B, N and NB events respectively. Most of the type B events are subtype B- with negative C_B (34.8%) while most of the type N events are subtype N+ with positive C_N (30.8%). For type NB events, the main subtype is N+B- (19%), which can be treated as the combination of subtype B- and N+. Those proportions suggest that the chorus wave amplitude is more likely modulated by background magnetic field with negative correlation and by the plasma density with positive correlation (totally 84.7%). These modulation relations are consistent

with those of the ULF wave modulation events reported in outer Li et al. [2011a] and inner magnetosphere [Xia et al., 2016].

Besides the statistical study of THEMIS data, we also perform a similar analysis on the measurements of Van Allen Probes from September 2012 to May 2018. The statistical results of Van Allen Probes data are plotted in the right column of Figure 4.2. Due to the orbit of Van Allen Probes, most of the 3798 events are detected within $L =\sim 6$. From the distribution of the proportions of different types of events shown by Figure 4.2j, we can see that most of the modulation events (64.1%) are type N+, with positively correlated plasma density only. Also, there is a considerable portion of type N- (12.8%) while the portion of the other types that corresponding to the background magnetic field is about 23%. This proportion distribution is due to the fact that in the Van Allen Probes traveling region which is not far from the plasmapause, the variation of plasma density is more significant and occurs more frequently than the variation of background magnetic field. Looking into the MLT distribution of event numbers, most of the events occur uniformly over a broad region from pre-midnight to pre-dusk region. For the radial distribution, most of the events occur at $L =\sim 6$ and the event number decreases as L decreases.

Combining the results of both THEMIS and Van Allen Probes measurements, at larger L shell region ($L > 10$), most of the modulation events take place around the dawn sector while for regions of small L shell ($L < 10$), the MLT distribution of the modulation events become more uniform. Both THEMIS and Van Allen Probes measurements indicate that the number of modulation events decreases as L decreases. However, we can not directly compare the event number from THEMIS satellites at larger L shell region with that from Van Allen Probes at smaller L shell since the numbers of orbits are quite different for these two data sets.

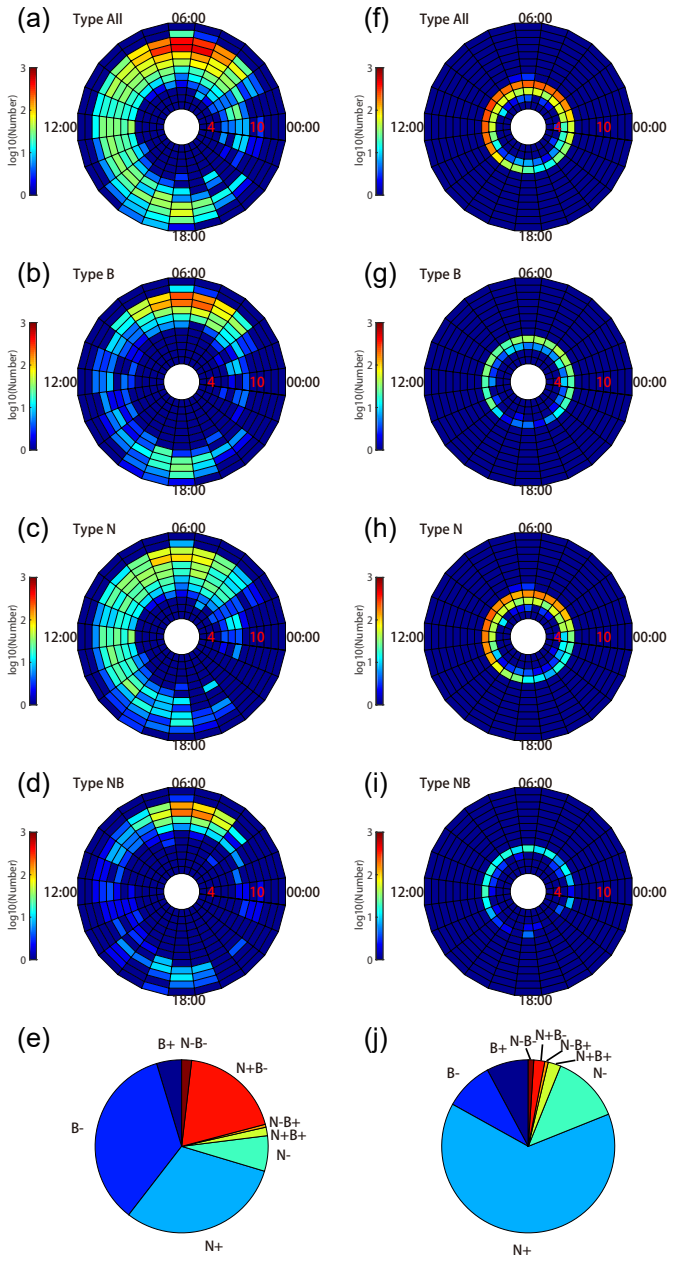

Figure 4.2. Spatial distribution of the numbers of different modulation types and the proportions of different subtypes.
The spatial distribution of modulation events numbers for all types (a), type B (b), type N (c) and type NB (d) respectively from THEMIS observation. (e): the proportion of different subtypes of events from THEMIS observation. (f) - (j) show similar content to (a) - (e) except for Van Allen Probes observation of modulation events.

4.5 Effects of the Modulator's Perturbation Amplitudes

We have learned that the intensity of the chorus wave can be modulated by the oscillations of the background magnetic field and plasma density. For the modulation events, the relation between the intensity of chorus wave and the amplitudes of the oscillations also needs to be investigated quantitatively in order to better understand the mechanism of the modulation events. Thus we find out the maximum amplitudes of the chorus waves for all the modulation events and calculate the standard deviations of corresponding variations of background magnetic field and plasma density, which are then used to study how the amplitudes of oscillations can affect the chorus intensity.

Figures 4.3a and 4.3b show the relationship between the logarithm values of chorus intensity and the logarithm values of standard deviations of background magnetic field for events observed by THEMIS satellites with positive C_B (subtypes B+, N+B+ and N-B+) and negative C_B (subtypes B-, N+B- and N-B-) respectively. The values of chorus intensity and magnetic field standard deviation are normalized by the mean background magnetic field over the event interval. The blue dots stand for type B events with only background magnetic field modulation (subtype B- in 4.3a and B+ in 4.3b) while the black dots are type NB events with both background magnetic field and plasma density modulations (subtypes N+B+ and N-B+ in 4.3a; N+B- and N-B- in 4.3b). The blue and black solid lines are linear fitting lines for dots with corresponding colors and the dashed lines outline the boundaries of the corresponding 95% predicting intervals. In Figure 4.3b, the dots center around the fitting lines with correlation coefficients of 0.66 (blue dots) and 0.69 (black dots), which indicates strong positive correlations between the intensity of chorus wave and the standard deviations of background magnetic field. The correlations in Figure 4.3a are slightly weaker with correlation coefficients of 0.44 (blue dots) and 0.31 (black dots). These positive correlations suggest that stronger oscillations of the background magnetic field tend to result in more intense chorus waves, especially for the events with negative C_B. Figures 4.3c and 4.3d

show the relationship between the logarithm values of normalized chorus intensity and the logarithm values of normalized standard deviations of plasma density (normalized by the mean plasma density over the event interval) for events observed by THEMIS satellites with positive C_N (subtypes N+, N+B+ and N+B-) and negative C_N (subtypes N-, N-B+ and N-B-) respectively. The red dots stand for type N events with only plasma density modulation (subtype N+ in 4.3c and N- in 4.3d) while the black dots are type NB events with both background magnetic field and plasma density modulations (subtypes N+B+ and N+B- in 4.3c; N-B+ and N-B- in 4.3d). The effect of plasma density oscillation amplitude on chorus intensity is not as significant as that of background magnetic field since the data dots distribute uniformly and the correlation coefficients for Figures 4.3c and 4.3d are all very low (absolute values $<\sim 0.1$).

Figures 4.3e-4.3h show in the same format as Figures 4.3a-4.3d but for observations of the Van Allen Probes. The effect of magnetic field oscillation is noticeable (Figures 4.3e and 4.3f) but not as significant as that in Figure 4.3b due to lack of measurements of events with large magnetic field oscillation. The effect of plasma density is still very weak (Figures 4.3g and 4.3h) from the results of Van Allen Probes' observations. Totally, the results from these two magnetospheric satellites missions indicate the chorus intensity increases when the amplitude of background magnetic field perturbation increases, but does not show a clear dependence on the amplitude of plasma density perturbation.

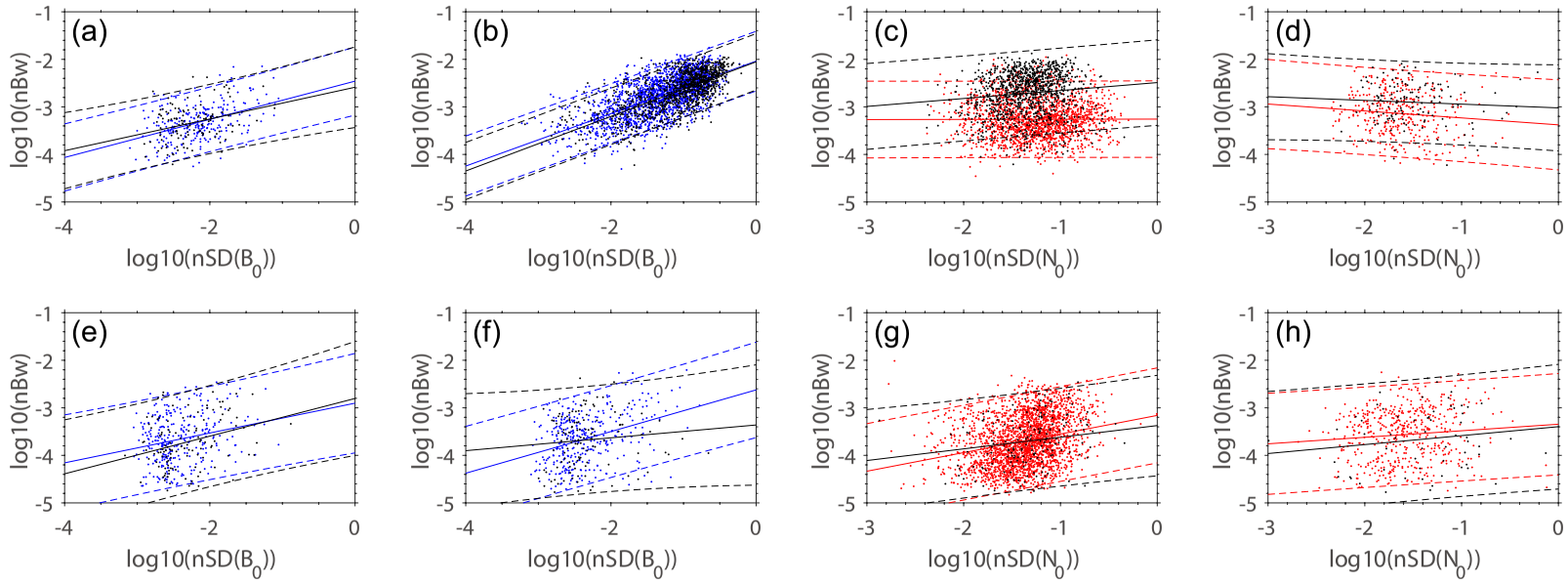

Figure 4.3. Relationship between the chorus intensity and the amplitudes of the perturbations of background magnetic field and plasma density for different types of chorus modulation events.
(a) and (b) show relation between normalized chorus wave intensity (y axis) and normalized amplitude of background magnetic field perturbation (x axis) for events observed by THEMIS (blue: type B, Black: type NB) with (a) positive and (b) negative correlations, respectively. (c) and (d) show relation between normalized chorus wave intensity (y axis) and normalized amplitude of plasma density perturbation (x axis) for events observed by THEMIS (red: type N, Black: type NB) with (c) positive and (d) negative correlations , respectively. (e) - (f) show similar content to (a) - (d) except for Van Allen Probes observation.

4.6 Conclusions and Discussion

In this chapter, we use nearly 2 years of observations of three THEMIS satellites (A, D, E) and over 5.5 years' observations of two Van Allen Probes (A, B) to statistically study the modulations of chorus emissions by background magnetic field and plasma density. The modulation events are identified automatically by calculating the correlation coefficients between the magnetic field strength (or plasma density) and the chorus emission intensity (calculated by integrating the magnetic wave power spectrum density through 0.1 to 0.8 electron cyclotron frequency f_{ce}). The modulation events are divided into three types according to whether the chorus intensity is highly correlated to the variations of magnetic field strength (type B), plasma density (type N), or both (type NB). The three types are also sorted into eight subtypes according to the sign of correlation coefficients. Finally, we analyze the relationships between chorus intensity and amplitudes of the magnetic field and plasma density perturbations. The conclusions are listed below:

1. The proportions of types B and N are comparable ($\sim 1/3$) and slightly larger than that of type NB ($\sim 1/5$) for the THEMIS observations, while for the Van Allen Probes observations at relatively smaller L-shell most of the events are type N.

2. The chorus intensity is mostly correlated to the magnetic field strength negatively and plasma density positively.

3. The spatial distribution of modulation events matches that of the chorus emissions well, resulting in most modulation events at the dawn sector for all the three types and decreasing occurrence as L shell decreases.

4. For the modulation events, chorus intensity is larger when the amplitude of the magnetic field perturbation is larger but has no clear dependence on the amplitude of plasma density perturbation.

The linear theory can partially explain the excitation of chorus waves especially for the small amplitude chorus waves and the early stage of strong chorus wave generation. In

the study of Li et al. [2011a], the mechanism of chorus modulation by compressional ULF waves corresponding to the linear growth rate can be decomposed as the changes of the ratio between the resonant electrons and the total electrons $R(V_R)$ as well as the electron anisotropy $A(V_R)$, and most modulation events are caused by the variations of $R(V_R)$. The effects of density variation on the linear growth rate were also discussed in Li et al. [2011b]. In this study, both density enhancement (DE) and depletion (DD) can increase the value of $R(V_R)$ and consequently the linear growth rate. The DE can increase $R(V_R)$ by reducing the minimum energy of resonant electrons (increasing the resonant electrons) while the DD increased $R(V_R)$ by the decreasing the denominator of $R(V_R)$. Thus the relationship between the density variation and the linear growth rate can not be approximated monotonically. In the study of *Wu et al.* [2013], the growth rate of whistler-mode waves is more monotonic to background magnetic field than to the cold plasma density, which coincides with the effects of modulator's amplitudes in our study. The effects of cold plasma density are quite different for different hot plasma anisotropy values and different wave modes. To better understand the effects of background magnetic field and plasma density, more detailed studies involving the wave modes and other plasma parameters are needed and left as possible future works.

CHAPTER 5

THE EFFECTS OF LOCALIZED THERMAL PRESSURE ON EQUILIBRIUM MAGNETIC FIELDS AND PARTICLE DRIFTS IN THE INNER MAGNETOSPHERE[1]

The work shown in this chapter has been published as "**Xia, Z.**, Chen, L., Artemyev, A. V., Zhu, H., Jordanova, V. K., and Zheng, L. (2019). **The effects of localized thermal pressure on equilibrium magnetic fields and particle drifts in the inner magnetosphere**. *Journal of Geophysical Research: Space Physics*, 124. https://doi.org/10.1029/2018JA026043".

5.1 Introduction

The partial ring current generated by the asymmetric azimuthal drift of energetic ions and electrons exhibits diamagnetic effect on the Earth's magnetic field due to the force balance between thermal pressure of the hot particles and the background magnetic pressure, especially in the magnetic storm time [Fukushima and Kamide, 1973] when the ring current intensity increases and the plasma β value can reach about $\sim O(1)$. Ukhorskiy et al. [2006] has reported the magnetic dip structure, which is caused by the diamagnetic effect of the storm time partial ring current, as a local magnetic minimum followed by a magnetic island (local maximum) at larger L shell region from the TS05 model [Tsyganenko and Sitnov, 2005]. This magnetic dip structure locates from midnight to post noon region in a few magnetic local time (MLT) hours and near $5-6R_E$ with a width of $\sim 2R_E$ in the radial direction. The depth of the dip (absolute value of difference between the local minimum magnetic field and the quite time magnetic field) can reach about 50 nT.

[1]©2019 Amercian Geophysical Union. Portions Adapted, with permission from, Z. Xia, "The effects of localized thermal pressure on equilibrium magnetic fields and particle drifts in the inner magnetosphere," Xia, Z., Chen, L., Artemyev, A. V., Zhu, H., Jordanova, V. K., and Zheng, L., Journal of Geophysical Research: Space Physics, 124.

The magnetic dip structure has been recently observed by the inner magnetosphere spacecraft. Xiong et al. [2017] provided a single satellite observation of magnetic dip generated by the injection of energetic ions during substorm by Van Allen Probes, with increased thermal pressure and decreased magnetic field. A butterfly pitch angle distribution of energetic electrons was found and explained as the result of inward transport of the relativistic electrons, which was caused by the magnetic gradient drift due to the magnetic dip. He et al. [2017] reported another magnetic dip event during the substorm using multiple-satellite observations. In this event, the magnetic dip together with the energetic ions moves at a speed comparable to the ion's drift velocity, which indicates that the magnetic dip structure is induced by the ring current ions. Excitation of electromagnetic ion cyclotron (EMIC) waves were also observed accompany with magnetic dip structures [He et al., 2017; Remya et al., 2018]. According to linear theory analysis, the magnetic dip accompanied with high ion β and ion temperature anisotropy can provide a favorable condition for EMIC wave generation. Moreover, the center region of magnetic dip is a kind of "minimum-B-pockets" in the equatorial plane, which can generate whistler mode waves [Santolík, 2008; Tsurutani et al., 2009; Tenerani et al., 2013]. Zhima et al. [2015] also observed whistler mode wave generating at the edges of magnetic dip, where positive temperature anisotropy and pancake distribution existed to provide free energy for growth of the whistler mode waves.

The magnetic field topology in the inner magnetosphere affects the drift motion of the energetic particles significantly because of dominant magnetic gradient and curvature drifts. The magnetic dip structure, comparing with empirical or analytic dipole magnetic fields, exhibits two significantly different features. The first one is the presence of an azimuthal magnetic field gradient, which causes radial drift. When eastward drifting energetic electrons encounter the magnetic dip structure, the azimuthal gradient of the magnetic dip causes the electrons to drift inward and results in the butterfly distribution as discussed in Xiong et al. [2017]. Another difference is the radial gradient of magnetic field becomes positive (always

negative for dipole field) at the radial outer edge of the magnetic dip. This inverse gradient may cause the inverse gradient drift motion. Although ring current protons and radiation belt electrons do not interact directly, the magnetic dip driven by the ring current provides an indirect way to affect the variability of radiation belt electron populations. Learning about the formation condition of magnetic dip structure and its influence to the energetic particles' drift motion can enhance our understanding of dynamic processes in the inner magnetosphere.

Equilibrium magnetosphere models are widely used to calculated three-dimensional (3-D) self-consistent magnetic field (SCB) that holds force balance with plasma pressure in the inner magnetosphere [Zaharia et al., 2006; Jordanova et al., 2010; Yu et al., 2012] and in the plasma sheet [Yue et al., 2013, 2014, 2015]. Both spacecraft observations and inner magnetosphere models indicate that, as L shell increases, the thermal pressure of ring current increases to a peak value and then decreases [De Michelis et al., 1999; Chen et al., 2010; Godinez et al., 2016; Imajo et al., 2018]. Thus, we can use a Gaussian distribution to approximate the radial pressure distribution. Our previous work [Xia et al., 2017] used a 2-D axisymmetric equilibrium model to calculate SCB under a radial Gaussian thermal pressure and investigated instability condition for field line resonance, which favored more negative radial gradient of plasma pressure. It also showed that sufficiently large plasma β (ratio between plasma pressure and magnetic pressure) could result in the change of magnetic field topology and even formation of the local magnetic minimum (magnetic dip). In this study, we systematically study the effects of the Gaussian thermal pressure distribution on the magnetic field configuration (and magnetic dip formation) and the resulting changes in particle magnetic gradient and curvature drifts. There are four parameters determining the pressure distribution: the location of the pressure peak L_0, the β value at the pressure peak β_0, the width of half pressure peak σ_0, and the equatorial pressure anisotropy A_e. In addition, we also use the 3-D ring current-atmosphere interactions model with SCB (RAM-SCB)

model [Jordanova et al., 2010] to study the influence of the azimuthal pressure distribution, which is characterized by the four parameters above and another parameter, the MLT width of half pressure peak in the azimuthal direction σ_{MLT}. The purpose of this study is to construct a comprehensive understanding of the relationship between the configuration of Earth's magnetic field and the ring current plasma pressure, and to estimate the relative perturbation of magnetic drift motions under this pressure and the critical condition to form the magnetic dip structure.

5.2 Axisymmetric Equilibrium Model

5.2.1 Equilibrium Magnetic Field Model Description

The axisymmetric equilibrium model used in this study is the same as that in our previous work [Xia et al., 2017], whose basic theory had been discussed in the work of Cheng [1992] and Zaharia et al. [2004]. The basic magnetohydrodynamics equations to be solved for the pressure equilibrium are

$$\mathbf{J} \times \mathbf{B} = \nabla \cdot \mathbf{P}, \tag{5.1}$$

$$\nabla \times \mathbf{B} = \mu_0 \mathbf{J}, \tag{5.2}$$

$$\nabla \cdot \mathbf{B} = 0, \tag{5.3}$$

where $\mathbf{J}$ is the current, $\mathbf{B}$ is the magnetic field, μ_0 is the vacuum permeability, and $\mathbf{P}$ is the anisotropic thermal pressure tensor that can be represented as $P_\perp \mathbf{I} - (P_\perp - P_\parallel)\hat{b}\hat{b}$, where $\mathbf{I}$ is the unit tensor, $\hat{b} = \mathbf{B}/B$ is the unit vector of the magnetic field, and $P_\perp$ and $P_\parallel$ are the perpendicular and parallel pressure components. The magnetic field $\mathbf{B}$ is divergence-free according to Equation (5.3) and can be expressed in terms of two Euler potential ψ and α as $\mathbf{B} = \nabla\psi \times \nabla\alpha$. Thus, $\mathbf{B}$ is perpendicular to both $\nabla\psi$ and $\nabla\alpha$ and the intersections of

constant ψ and constant α surfaces correspond to magnetic field lines. In our model, we choose the magnetic flux as ψ and the azimuthal angle as α for the axisymmetric fields.

The computation coordinates are curvilinear flux coordinates corresponding to ψ (radial direction), α (azimuthal direction), and the length along field line (field line direction), which had been introduced in Xia et al. [2017]. Eventually, Equation (5.1) can be reduced to the form to be solved for ψ in the meridian $(X - Z)$ plane:

$$\mu_0 \mathbf{J} \cdot \nabla\alpha = \nabla \cdot [(\nabla\alpha \cdot \nabla\psi)\nabla\alpha - (\nabla\alpha)^2 \nabla\psi] = -\frac{\mathbf{B} \times \nabla\alpha}{\sigma_P B^2} \cdot \left[\mu_0 \nabla P_\perp + (1 - \sigma_P)\nabla(\frac{B^2}{2})\right], \quad (5.4)$$

where $\sigma_P = 1 + \mu_0(P_\perp - P_\parallel)/B^2$.

The pressure along the field line at an arbitrary location, including the perpendicular component $P_\perp$ and parallel component $P_\parallel$, can be obtained from the equatorial value of the anisotropic pressure through the assumption of Maxwellian plasma distribution [Tsyganenko, 2000; Xiao and Feng, 2006]:

$$P_\perp = \frac{P_{\perp e}}{[1 + A_e(1 - S)]^2}, \quad (5.5)$$

$$P_\parallel = \frac{P_{\parallel e}}{1 + A_e(1 - S)}, \quad (5.6)$$

$$A = \frac{1}{1 + A_e(1 - S)} - 1, \quad (5.7)$$

where $S = B_e/B$ is the ratio between the magnitudes of the equatorial magnetic field B_e and the magnetic field at the location of interest B, $A = P_\perp/P_\parallel - 1$ is the anisotropy, the subscript "e" denotes the value in the equatorial plane. A Gaussian distribution $P_e(x) = P_0 \exp[-(x - L_0)^2/2\sigma_0^2]$ is used to approximate the thermal pressure of the symmetric ring current, where $P_e = (2P_{\perp e} + P_{\parallel e})/3$ is the average pressure in the equatorial plane, P_0, L_0, and σ_0 are the peak pressure, the location of the pressure peak, and the width of the half pressure peak respectively. The value of P_0 is set to be $\beta_0 P_{mag}$, where P_{mag} is the magnetic pressure at L_0, and β_0 is the constant β at L_0. Thus, the equatorial distribution of plasma

pressure in our model can be determined by these four parameters: L_0, σ_0, β_0 and A_e. The case of $\beta_0 = 0$ represents the cold plasma case (the dipole field) and the $A_e = 0$ case represents the isotropic pressure case.

After iteratively solving Equation (5.4) for the distribution of ψ and the corresponding $\mathbf{B}$ in the meridian plane, we can finally reach a equilibrium state, which satisfies the convergence condition $\Delta = \Sigma_{i,j}|[\psi_{i,j}(n) - \psi_{i,j}(n-1)]/\psi_{i,j}(n-1)| < 2 \times 10^{-5}$, where i and j are the grid indices for the radial and field line directions respectively, n is the iteration number of the calculation, and Δ measures the relative difference between the current step n and the previous step $(n-1)$. The domain of our equilibrium model is set to be $[3R_E, 9R_E]$, which is large enough to make sure the plasma pressures at the boundaries are nearly zero. The numbers of grids are 151 in the radial direction and 181 in the field line direction to ensure sufficient accuracy. The magnetic field for the initial step of the iterative method and the boundary magnetic field at the inner, outer, north, and south boundaries are set to be the Earth's dipole field. As the magnetic field is updated at each iteration step, the value of P_0 is also adjusted so that the value of β_0 can keep constant.

5.2.2 Example of the SCB Model

Figure 5.1 shows an example of model result for the case with $\beta_0 = 0.8$, $\sigma_0 = 0.4R_E$, $L_0 = 5$ and $A_e = 0$. Figure 5.1a shows the average pressure distribution in the meridional plane, and Figure 5.1b shows the corresponding topology of equilibrium magnetic field lines (the red solid lines), with the dipole field lines (the black dashed lines) also shown as a comparison. As the force equilibrium develops, the magnetic field lines expand from the peak pressure location ($L_0 = 5$) inward and outward due to the thermal pressure, leading to weakened magnetic field strength there. In Figure 5.1c, the variations of β (the black line) and of the normalized pressure (the blue line, normalized by the pressure peak) at the equator are shown as functions of x. The peak of β is slightly outside the peak of the normalized

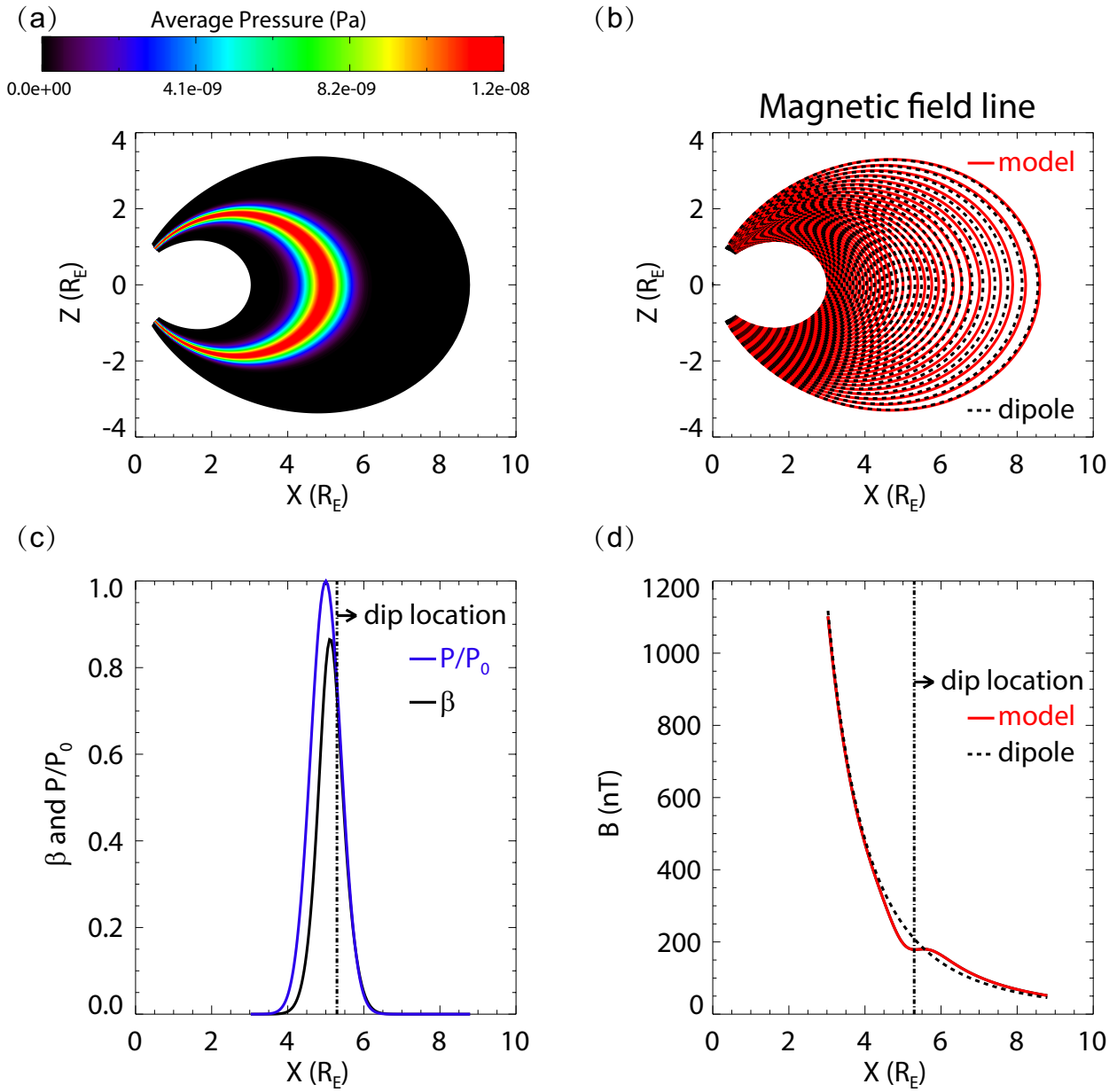

Figure 5.1. Model result for case with $\beta_0 = 0.8$, $\sigma_0 = 0.4R_E$, $L_0 = 5$ and $A_e = 0$. (a) The pressure distribution in the meridional plane. (b) The topologies of the modeled magnetic field lines (red solid lines) and dipole field lines (black dashed lines). (c) The variation of β versus x in the equator (black line) and the variation of normalized pressure versus x (blue line). (d) The variation of modeled magnetic field strength versus x in the equator (red solid line) and the variation of dipole field strength versus x (black dashed line).

pressure at L_0, because the magnetic field strength decreases as x increases. In Figure 5.1d, the variations of modeled (the red solid line) and dipole (the black dashed line) magnetic field strength at the equator are compared. Unlike monotonically decreasing dipole magnetic field, the modeled magnetic field exhibits a local minimum at about $x = 5.3R_E$ (labeled by the vertical dash-dotted lines in Figures 5.1c and 5.1d), outward of the peaks of plasma pressure and β (Figure 5.1c). The absolute value of difference between the modeled and dipole magnetic field strength $|\Delta B|$ at the local minimum is about 50 nT, comparable to the Tsyganeko empirical model results noted by Ukhorskiy et al. [2006].

5.3 Results of the SCB Model

5.3.1 Parametric Dependence of Magnetic Configuration

Here we study the effects of β_0, L_0, σ_0 and A_e on the magnetic field configuration, by changing one of the four parameters at a time while keeping the rest three fixed as the nominal case shown in Figure 5.2. Figures 5.2a and 5.2b show the variations of modeled equatorial magnetic field strength (B) versus x for cases with varying $\sigma_0 = 0.2, 0.3, 0.4, 0.5, 0.6R_E$ (Figure 5.2a) and for cases with varying $L_0 = 4.0, 4.5, 5.0, 5.5, 6.0$ (Figure 5.2b). Figures 5.2c and 5.2d show the corresponding normalized differences between modeled and dipole magnetic fields ($\Delta B/B_{dipole}$, where $\Delta B = B - B_{dipole}$ and the subscript dipole represents the dipole field). One can see that magnetic dip structure occurs for small values of σ_0 (0.2-0.4 R_E) from Figure 5.2a, and for almost all cases with different L_0 values from Figure 5.2b. The detailed effects of σ_0 and L_0 on the magnetic dip formation will be discussed in section 5.3.3 later. Figure 5.2c shows that for the same L_0, a smaller value of σ_0 leads to a narrower magnetic dip but with similar perturbation of $\Delta B/B_{dipole}$ at the dip location. The effect of L_0 on $\Delta B/B_{dipole}$ is less significant (Figure 5.2d), and the minimum value of $\Delta B/B_{dipole}$ remains nearly constant except different dip locations. The dominant factor determining the minimum value of $\Delta B/B_{dipole}$ should be β as noted in Xia et al. [2017].

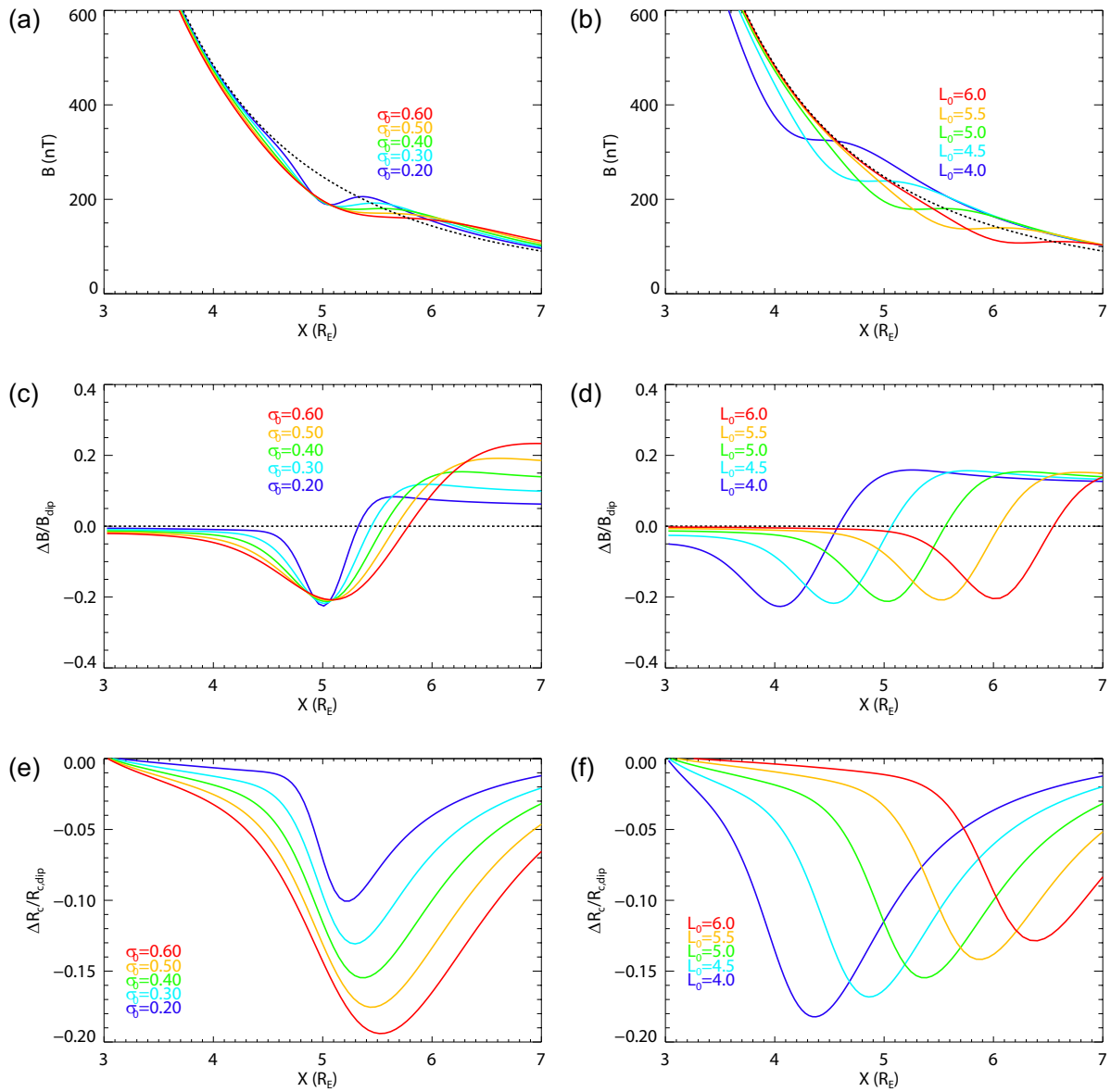

Figure 5.2. The effects of σ_0 and L_0 on the magnetic field topology.
The variations of modeled magnetic field strength versus x in the equator for cases with (a) $\beta_0 = 0.8, A_e = 0, L_0 = 5,\ \sigma_0 = 0.2, 0.3, 0.4, 0.5, 0.6 \quad R_E$ (b) $\beta_0 = 0.8, A_e = 0, \sigma_0 = 0.2R_E, L_0 = 4.0, 4.5, 5.0, 5.5, 6.0.$ (c and d) The variations of the normalized difference between modeled and dipole magnetic fields $\Delta B/B_{dipole}$ versus x for the same cases in (a) and (b), respectively. (e and f) The variations of the normalized difference between the radius of curvature of modeled and dipole magnetic field $\Delta R_c/R_{c,dip}$ versus x for the same cases in (a) and (b) respectively.

Besides the magnetic field strength, the curvature of magnetic field line is also changed due to the presence of thermal pressure. We plot normalized difference of the radius of curvature $\Delta R_c/R_{c,dip} = (R_c - R_{c,dip})/R_{c,dip}$, in Figures 5.2e and 5.2f. The value of $R_{c,dip}$ equals to $L/3$ for dipole field, where L is the L shell value. The value of R_c can be calculated from the model results by $R_c = 1/|\mathbf{b} \cdot \nabla \mathbf{b}|$, where $\mathbf{b} = \mathbf{B}/B$ is the magnetic field unit vector. The results show that R_c decreases by up to about 20% at the region outside L_0, and a larger value of σ_0 and a smaller value of L_0 favor enlarging the perturbation of the curvature.

After learning the dependence on σ_0 and L_0, we now focus on the role of the equatorial anisotropy A_e. The variations of B, $\Delta B/B_{dipole}$ and $\Delta R_c/R_{c,dip}$ for varying $A_e = -0.4, 0.0, 1.0, 2.0, 3.0, 4.0$ are shown in Figures 5.3a-5.3c, respectively. As A_e increases, the normalized magnetic perturbation ($\Delta B/B_{dipole}$) varies only slightly. This can be explained by that the magnetic perturbation is mainly controlled by the gradient of the perpendicular thermal pressure ($P_\perp$) instead of the anisotropy [Xia et al., 2017]. The effect of A_e on the field line curvature, however, is much more significant. For a large value of $A_e = 4.0$, $\Delta R_c/R_{c,dip}$ can even change its sign and reach a positive value up to about 0.3 inside the pressure peak. Outside the pressure peak, the relative change in curvature radius becomes more negative as A_e increases.

For the effect of β on the change of magnetic field strength and magnetic field line curvature, we make model runs for 3,000 combinations of four parameters, 5 values of L_0 ranging from 4 to 6, 24 values of β_0 ranging from 0.01 to 1.0, 5 values of σ_0 ranging from 0.2 to 0.6 R_E, and 5 values of A_e ranging from -0.4 to 0.4. For each run, we make scatter plots of minimum $\Delta B/B_{dipole}$ versus peak β value β_{peak} and minimum $\Delta R_c/R_{c,dip}$ versus β_{peak}, shown by Figures 5.4a and 5.4b, respectively. The figures show that the magnitudes of both minimum $\Delta B/B_{dipole}$ and minimum $\Delta R_c/R_{c,dip}$ increase as β_{peak} increases. For $\Delta B/B_{dipole}$, we make a polynomial fit for all the points, which is $(\Delta B/B_{dipole})_{min} = -0.339\beta_{peak} + 0.112\beta_{peak}^2$ and plotted as the solid line in Figure 5.4a. For $\Delta R_c/R_{c,dip}$, we also obtained a linear fitted line with slope of about -0.214 and plot it as the solid line in Figure 5.4b.

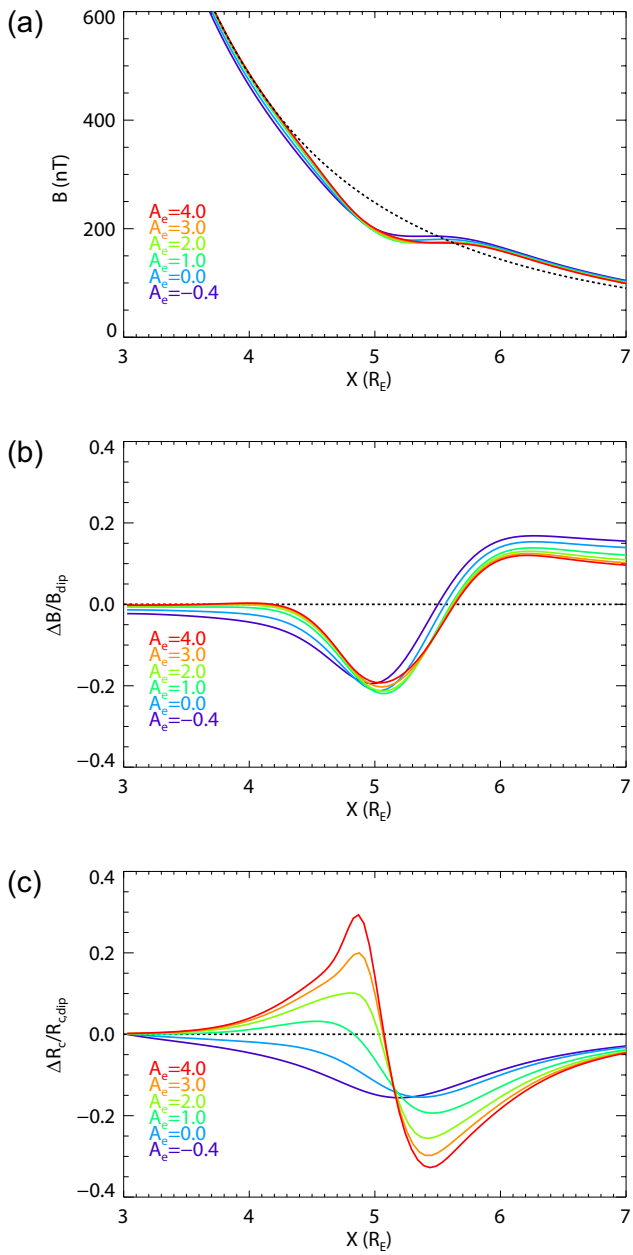

Figure 5.3. The effects of A_e on the magnetic field topology.
The variations of (a) B, (b) $\Delta B/B_{dipole}$, and (c) $\Delta R_c/R_{c,dip}$ versus x for cases with $L_0 = 5$, $\beta_0 = 0.8$, $\sigma_0 = 0.4 \quad R_E$, and $A_e = -0.4, 0.0, 1.0, 2.0, 3.0, 4.0$.

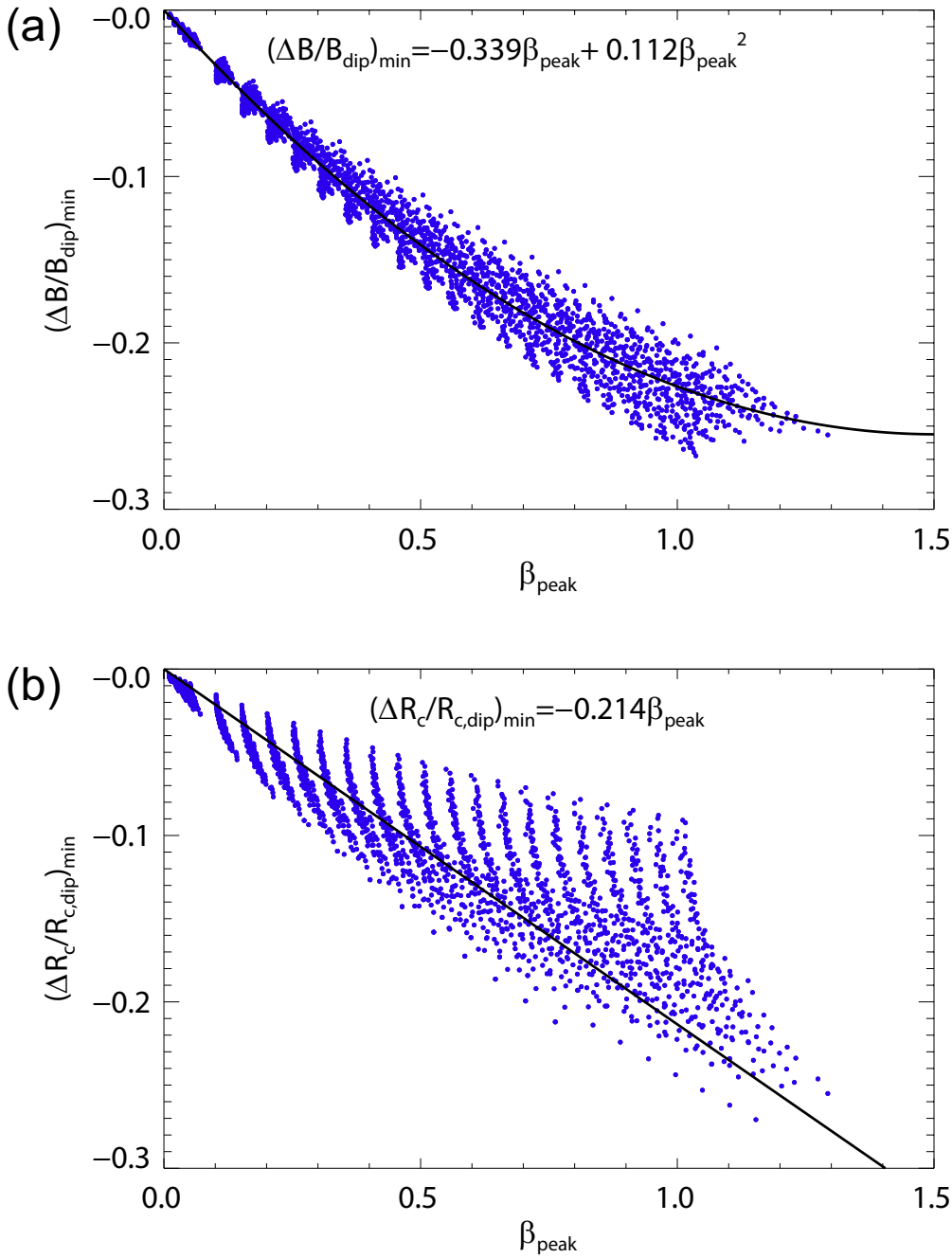

Figure 5.4. The effects of β on the magnetic field topology.
Scatter plots of (a) minimum $\Delta B/B_{dip}$ versus β_{peak} and (b) minimum $\Delta R_c/R_{c0}$ versus β_{peak}. The dots in the figure represent all the cases with L_0 from 4 to 6, β_0 from 0.01 to 1.0, σ_0 from 0.2 to 0.6 R_E and A_e from -0.4 to 0.4.

5.3.2 The Effects of Magnetic Perturbation on Gradient and Curvature Drifts

At the presence of spatially varying magnetic field, charged particles experience magnetic gradient and curvature drift across field lines, due to the gradient of magnetic field strength and the curvature of magnetic field line, respectively. The drift velocities of gradient and curvature drifts for a relativistic particle can be expressed, respectively, as

$$\mathbf{v}_g = \frac{\gamma m v_\perp^2}{2qB} \frac{\mathbf{B} \times \nabla B}{B^2} \tag{5.8}$$

and

$$\mathbf{v}_c = \frac{\gamma m v_\parallel^2}{qB} \frac{\mathbf{R}_c \times \mathbf{B}}{R_c^2 B}, \tag{5.9}$$

where $\gamma = (1 - v^2/c^2)^{-(1/2)}$ is the relativistic factor, v is the particle speed, and $v_\perp$ and $v_\parallel$ are the speed components perpendicular and parallel to the background magnetic field. The direction of $\mathbf{R_c}$ is opposite to the direction of $\mathbf{b} \cdot \nabla \mathbf{b}$. The ring current thermal pressure leads to the change of the magnetic field configuration and thus introduces additional gradient and curvature drift motions. From Equations (5.8) and (5.9), for the gradient drift and curvature drift velocities, particle-independent terms that are related to only the magnetic field configuration are $D_g = \mathbf{B} \times \nabla B / B^3$ and $D_c = \mathbf{R}_c \times \mathbf{B}/(R_c^2 B^2)$, respectively. The relative changes of the two terms at the equator to those for the dipole field are shown by Figures 5.5a and 5.5b respectively, for cases with $\beta_0 = 0.8, A_e = 0, L_0 = 5$, and varying $\sigma_0 = 0.2, 0.3, 0.4, 0.5, 0.6 R_E$. The largest $\Delta D_c / D_{c,dip}$ can be up to 0.5 for $\sigma_0 = 0.2 \quad R_E$ case, while the variation of the gradient drift term is more significant. For the $\sigma_0 = 0.2 \quad R_E$ case as an example, the relative change of the gradient drift term varies from ~ 2 inside the pressure peak to ~ -2 outside the pressure peak. The value less than -1 means the drift direction reverses.

We also evaluate the bounce-averaged magnetic gradient and curvature drift velocity, which depends on particle's equatorial pitch angle. Figure 5.5c shows the relative change

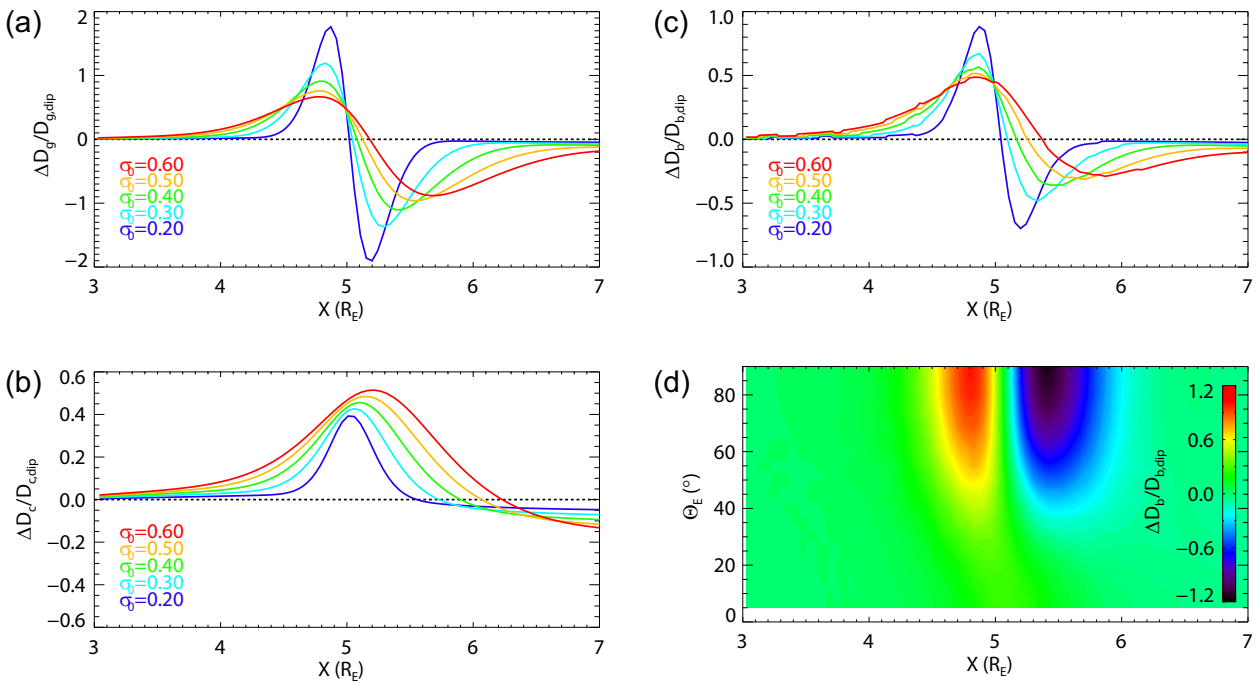

Figure 5.5. The effects on the magnetic drift motions.
(a) The variations of normalized difference of D_g $((D_g - D_{g,dip})/D_{g,dip})$ versus x for cases with $\beta_0 = 0.8, A_e = 0, L_0 = 5$, $\sigma_0 = 0.2, 0.3, 0.4, 0.5, 0.6 \quad R_E$; (b) the variations of normalized difference of D_c versus x for the same cases. (c) The variations of normalized difference of bounce-averaged total drift velocity $\Delta D_b/D_{b,dip} = (D_b - D_{b,dip})/D_{b,dip}$ versus x for the same cases. (d) The variations of bounce-averaged total drift velocity $\Delta D_b/D_{b,dip} = (D_b - D_{b,dip})/D_{b,dip}$ versus x and equatorial pitch angle θ_E for case with $\beta_0 = 0.8, \sigma_0 = 0.4 \quad R_E, A_e = 0, L_0 = 5$.

of the bounce-averaged drift velocity to the dipole case $\Delta D_b/D_{b,dip} = (D_b - D_{b,dip})/D_{b,dip}$, where D_b is the sum of the bounce-averaged gradient and curvature drift velocities. The equatorial pitch angle θ_E is set to be 45°. One can see that the change of bounce-averaged total drift velocity is also significant, up to ~ 1 inside the peak and ~ -1 outside the peak. The change of the bounce-averaged drift is less than the change of the gradient drift term shown in Figure 5.5a, because the magnetic perturbation induced by the plasma pressure occurs predominately near the equator. Moreover, we also calculate the relative change of the bounce-averaged drift velocity for equatorial pitch angles from 5°to 90°by using the self-consistent magnetic field with $\sigma_0 = 0.4 \quad R_E, \beta_0 = 0.8, A_e = 0$ and $L_0 = 5$, which are

shown by Figure 5.5d. The result shows that the change of the bounce-averaged drift is more significant for higher equatorial pitch angles because of dominant gradient drift over curvature drift and dominant magnetic perturbation near the equator over higher latitudes.

5.3.3 The Critical Condition for Magnetic Dip Formation

To examine the magnetic dip formation, we analyze the relationship between the normalized dip depth ($|\Delta B/B_{dipole}|$ at the dip, if magnetic dip exists, and β_0 for cases with different L_0 and σ_0 values. The modeled results are shown in colored solid lines with dot symbols of Figure 5.6 for $\sigma_0 = 0.2, 0.4, 0.6 \quad R_E$, respectively. One can see that when β_0 is small, there is no magnetic dip, represented by zero values of the normalized dip depth. When β_0 increases to a critical value, the dip structure may form. For cases with same σ_0, the critical value of β_0 decreases and the normalized dip depth increases as L_0 increases. Comparing among the three panels of Figure 5.6, for the same L_0 values, a smaller σ_0 results in a smaller critical β_0, and a larger normalized dip depth. When β_0 is sufficiently large, the normalized dip depth becomes independent of L_0.

The dependence of the critical β_0 on σ_0 and L_0 to form magnetic dips is also shown in Figure 5.7. As σ_0 increases or L_0 decreases, the critical β_0 tends to increase. The effect of σ_0 on the critical β_0 can be explained by comparing gradients of the background dipole field B_{dipole} and the perturbation magnetic field ΔB. If the gradient of ΔB (positive) balances that of B_{dipole} (negative), then the gradient of total magnetic field becomes 0, meaning the formation of magnetic dip. For the same L_0, a smaller σ_0 results in a larger gradient of ΔB (Figure 5.2c), which requires a smaller value of the critical β_0. The effect of L_0 on the critical β_0 can be understood as follows. Because $\Delta B/B_{dipole}$ is independent of L_0 (Figure 5.2d), and the gradient of B_{dipole} is larger for smaller L_0, zero gradient of the total magnetic field requires a larger value of critical β_0 for smaller L_0. In summary, the model results indicate that the formation of magnetic dip needs a considerable pressure gradient, which is

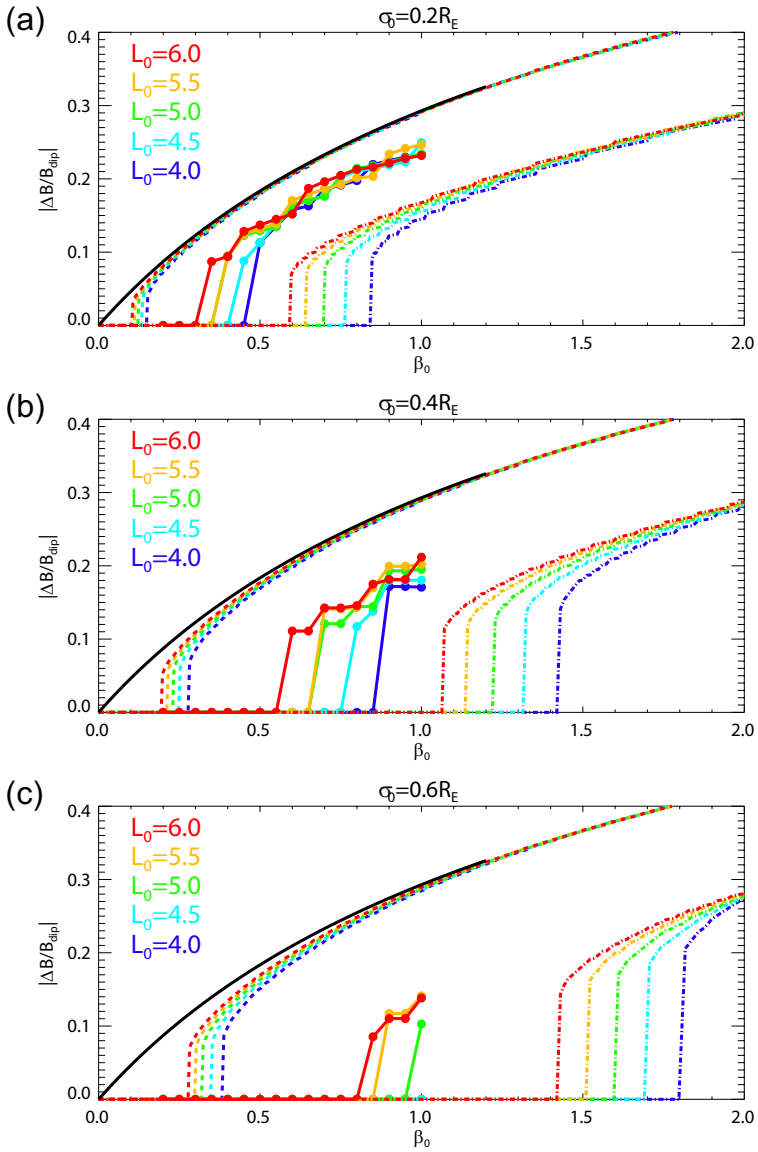

Figure 5.6. The relationship between the normalized dip depth ($|\Delta B/B_{dipole}|$) and β_0 for cases with different L_0 and σ_0 values.
The x-axis is β_0 and the y axis is the normalized dip depth. Panels (a)-(c) stand for $\sigma_0 = 0.2, 0.4, 0.6 \quad R_E$, respectively. The colored solid lines with circle symbols are model results. The black solid line is the analytical solution for uniform magnetic field. The colored dashed lines are analytical solution for circle magnetic field. The colored dash-dotted lines are analytical solution for dipole field with the assumption that the curvature keeps unchanged.

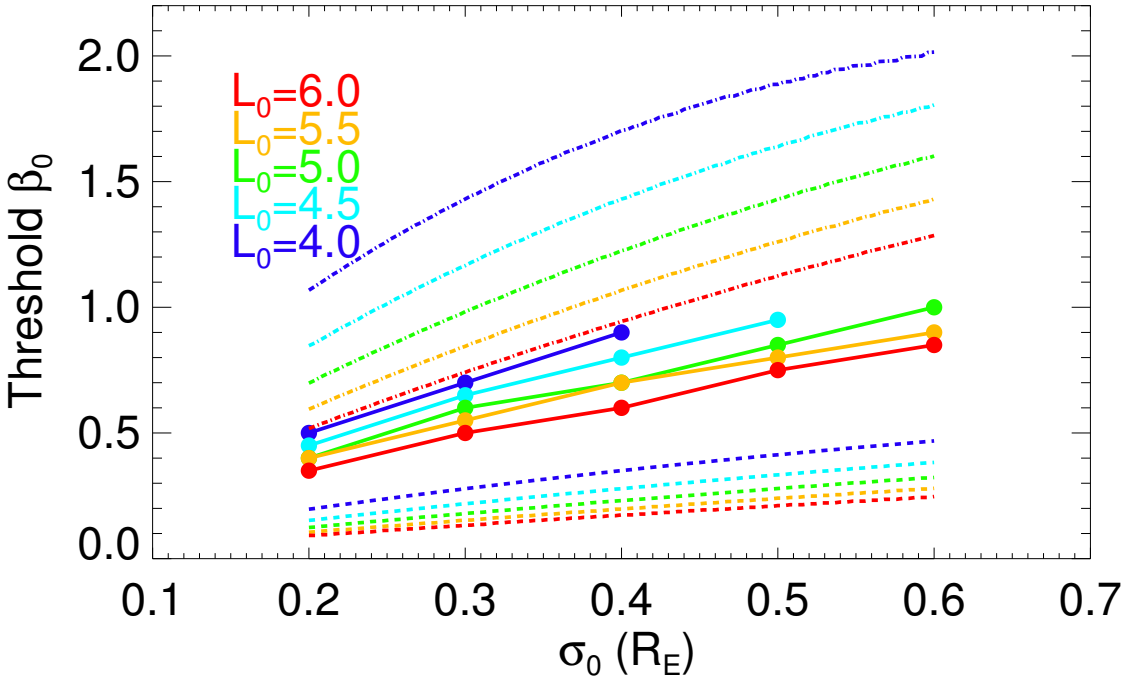

Figure 5.7. The critical β_0 to form the magnetic dip for cases with different L_0 and σ_0 values. The solid lines with circle symbols are results of our model. The dashed lines are results of analytic solution for circle magnetic field and the dash-dotted lines are results of analytic solution for dipole field with the assumption that the curvature keeps unchanged.

controlled by both the pressure peak value (corresponding to β_0) and the spatial scale of the pressure distribution (corresponding to σ_0). For smaller L shell region (closer to the Earth), since the gradient of background dipole field is larger, a larger thermal pressure gradient (corresponding to larger β_0 and smaller σ_0) is needed to produce magnetic field reduction that is large enough to form the magnetic dip.

Because simultaneous changes in magnetic field strength and magnetic field line curvature occur on top of dipolar fields, the solution to Equation (5.4) of equilibrium magnetic field can only be obtained numerically. Assumptions can be made, however, to simplify the problem and to obtain approximate analytical solution to make sense of the behavior of

magnetic dip. We consider the following three situations. The first and the simplest approximation to be considered is the presence of the localized plasma pressure in an initially uniform magnetic field B_0. In equilibrium, a magnetic dip forms whenever there is localized pressure distribution, and the normalized dip depth $|\Delta B/B_0|$ increases with β_0 according to $|\Delta B/B_0| = 1 - \sqrt{1/(1+\beta_0)}$ (Appendix E.1), which is overplotted as the black solid line in Figure 5.6. The critical β_0 to form a dip is essentially zero.

The second approximation is circular and planar magnetic fields, which can be generated by an infinitely long current wire. When embedded with radially Gaussian pressure distribution $P = P_0 \exp\left[-(r-L_0)^2/(2\sigma_0^2)\right]$, the force balance equation yields an analytical solution (Equation (E.3) of Appendix E.2). The analytical solution can be used to obtain the normalized dip depth, when the dip exists, as a function of β_0, L_0 and σ_0, which is overplotted as the colored dashed lines in Figures 5.6 and 5.7. Further analysis in Appendix E.2 demonstrates that the critical β_0 for the dip formation scales as σ_0/L_0. Such analytic results reveal similar behaviors of the modeled results of Equation (5.4), including (1) the critical β_0 increases with increasing σ_0 and decreasing L_0 (comparing the threshold β_0 values in Figure 5.7), (2) magnetic dip depth increases with decreasing σ_0, increasing L_0, and increasing β_0 (comparing the $|\Delta B/B_{dipole}|$ values in Figure 5.6), and (3) the magnetic dip tends to be independent of L_0 for larger β_0 (dashed lines with different colors merge together when β_0 is large in Figure 5.6).

The third approximation is to ignore the change of the curvature of the dipole field, for which an analytic solution of the magnetic field radial profile can be obtained as shown in Appendix E.3. The result using the analytic solution (Appendix E.3) is overplotted as the colored dash-dotted lines in Figures 5.6 and 5.7. Similar behaviors of the magnetic dip are also obtained when the curvature change is ignored. The approximation, however, yields a smaller magnetic dip depth, compared with the solution of Equation (5.4), which suggests the induced curvature change by the plasma pressure enhances the dip structure.

5.3.4 Comparison With 3-D SCB Model

Our 2-D axisymmetric magnetic field results are compared with 3-D RAM-SCB model [Jordanova et al., 2010] to study the effect of the azimuthal pressure distribution. We introduce a Gaussian distribution of the pressure in the azimuthal direction to represent the asymmetric ring current pressure. The pressure distribution in the equatorial plane is expressed as

$P = \beta_0 P_B(L_0) \exp\left[-(x - L_0)^2/(2\sigma_0^2)\right] \exp\left[-(MLT - MLT_0)^2/(2\sigma_{MLT}^2)\right]$,

where σ_{MLT} (in unit of MLT hour) denotes the width of half pressure peak in the azimuthal direction. The pressure peak is located at L_0 in the meridian plane corresponding to MLT_0 (set to 0 without loss of generality) and decays in the azimuthal direction with σ_{MLT} and in the radial direction with σ_0. Figure 5.8 shows the results of this 3-D model. Figures 5.8a and 5.8b show the distributions of thermal pressure and the resulting ΔB in the equatorial plane for the case with $\beta_0 = 0.65$, $L_0 = 4$, $\sigma_0 = 0.4 \quad R_E$, $A_e = 0$, and $\sigma_{MLT} = 1.0$. One can see that both the thermal pressure and ΔB magnitude maximize in the MLT_0 sector and decrease in the azimuthal direction, as expected. Figure 5.8c shows the variations of B versus x in the equator in the MLT_0 sector for cases with varying σ_{MLT} values, including the case of infinite σ_{MLT} denoting the azimuthally symmetric magnetic field. One can see that the magnetic field topology in the meridional plane at MLT_0 is independent of the value of σ_{MLT}, which is expected because partial derivative of the pressure with respect to MLT is zero there. However, σ_{MLT} determines the azimuthal pressure distribution and thus the azimuthal magnetic field variation. Smaller σ_{MLT} would result in larger azimuthal pressure and magnetic field gradient. The radial drift motion of energetic particles (and therefore the formation of the butterfly distribution of energetic electrons) is also affected by σ_{MLT}.

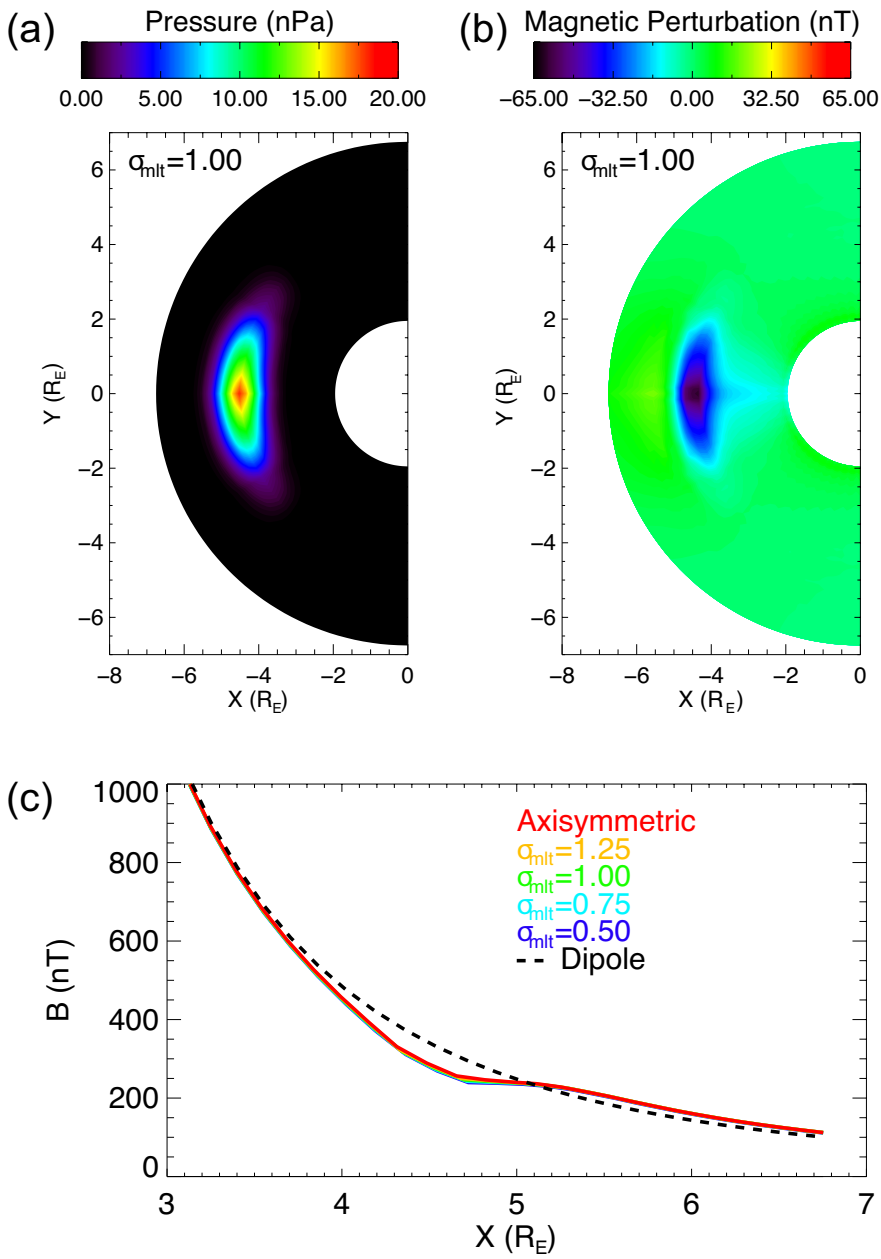

Figure 5.8. Three-dimensional ring current-atmosphere interactions model self-consistent magnetic field model results.
(a and b) The distributions of thermal pressure and magnetic perturbation in the equatorial plane for cases with $\beta_0 = 0.65$, $L_0 = 4$, $\sigma_0 = 0.4 \quad R_E$ and $\sigma_{MLT} = 1.0$. (c) The variations of B versus x in the equator of MLT_0 sector for cases with different σ_{MLT} values.

5.4 Conclusions and Discussion

In this chapter, we use axisymmetric equilibrium model to calculate SCB under a Gaussian thermal pressure distribution with four parameters: the ratio between plasma pressure and magnetic pressure at the pressure peak β_0, the radial location of the pressure peak L_0, the width of the half peak pressure σ_0 and the equatorial pressure anisotropy A_e. Then we analyze the effects of these parameters on the change of magnetic field configuration and the change of particle drifts. The main conclusions are summarized below:

1. The magnetic field perturbation $|\Delta B/B_{dipole}|$ increases with increasing β_0 and decreasing σ_0 and is weakly dependent of L_0 and A_e. The magnetic curvature perturbation $|\Delta R_c/R_{c,dip}|$ increases with increasing A_e, increasing β_0, increasing σ_0, and decreasing L_0.

2. The thermal pressure induces a change of gradient and curvature drift velocities. The induced change in the gradient drift is much greater than that in the curvature drift. The total drift change is more pronounced for larger equatorial pitch angles.

3. The magnetic dip structure forms when β reaches a critical value (0.5-1). Such critical value tends to increase with increasing σ_0 and decreasing L_0 values. When the dip forms, the dip depth tends to increase with decreasing σ_0, increasing β_0 and increasing L_0 values.

In this study, we use a symmetric Gaussian distribution to approximate the radial profile of the ring current pressure distribution. The following five points are worth noting regarding the realism of the symmetric Gaussian distribution used and the realistic pressure distribution profiles that may have different width at the inner and outer edges. First, the formation of the magnetic dip (that is, the existence of a positive radial slope of the equatorial magnetic field strength) requires a strong negative radial slope of plasma β (as mentioned in Section 5.3.3), and therefore depends on the plasma β peak and the radial width of the outer edge (instead of the inner edge). One can see from Figure 5.2a that the magnetic dip structure (the positive slope of the magnetic field) becomes weaker as the outer width increases. The increasing inner edge width slightly decreases the magnetic field inside the pressure peak

but does not affect the magnetic field strength at the pressure peak and beyond. The use of the symmetric Gaussian distribution is to help reduce the number of free parameters in the pressure distribution, and the effect of the width parameter reflects the effect of the outer edge when it comes to the formation of the magnetic dip. Second, ring current during quiet times and even moderate storms may not be able to provide a sufficiently negative radial plasma β slope and therefore the magnetic dip structures are not common in the inner magnetosphere during those times. We checked a statistical distribution of the proton pressure at midnight sector from De Michelis et al. [1999] under quiet geomagnetic condition (the top left panel in their Figure 1), which has two different radial edges with the outer edge width being slightly larger. Nonetheless the distribution near the pressure peak can be fairly well fitted by a Gaussian distribution of a radial width of $\sim$1.1 R_E. The use of such profile in our SCB model yields no magnetic dip, even when the pressure peak increases to a value so that $\beta = 1$. This is because the statistical pressure distribution smooths out any sharp edges in the plasma pressure and has a width too large to form a dip in the magnetic field. No dip is available in the inner magnetosphere for empirical magnetic field models (except storm time magnetic field from the TS05 model as seen in Figure 1a of Ukhorskiy et al. [2006]). Third, we also check a radial distribution of plasma pressure for a specific event observed by the Arase satellite, which is shown by the black line in Figure 9e of Imajo et al. [2018]. In this individual case, the Gaussian fitting approximates the observed radial pressure distribution very well of a width of about 0.5 R_E, which is narrower than that for the statistical distribution above. The plasma β for this event is also not sufficient to produce a dip, which is consistent with no dip observation for this event. Fourth, the strong connection between high plasma β and the appearance of magnetic dip has been established based on Van Allen Probes observation as shown by Figure 2 of Xiong et al. [2017] and Figure 2 of He et al. [2017]. After examination of these two events, the Van Allen Probes were moving mostly in the azimuthal direction unfortunately. Therefore, the estimation of radial width of

the outer edge is not available for simulating the equilibrium magnetic field profile. Finally, the plasma pressure distribution observations in the existing literature, unfortunately, may not be ideal for checking the theoretical relation between magnetic dip and plasma pressure. One of the reasons for such unfortunateness is that this theoretical relation was not revealed before. The establishment of radial profiles of plasma pressure in the inner magnetosphere, especially for individual events, may be resolved using the observation of THEMIS satellites, which can transverse the center of ring current radially. Our theoretical relations between the radial profiles of the plasma pressure and the equilibrium magnetic field can then be checked. We leave this effort as our future investigation.

CHAPTER 6

STATISTICAL CHARACTERISTICS OF IONOSPHERIC HISS WAVES[1]

The work shown in this chapter has been published as "**Xia, Z.**, Chen, L., Zhima, Z., Santolík, O., Horne, R. B., and Parrot, M. (2019). **Statistical characteristics of ionospheric hiss waves**. *Geophysical Research Letters*, 46. https://doi.org/10.1029/2019GL083275".

6.1 Introduction

Plasmaspheric hiss is a broadband, incoherent whistler mode wave with a typical frequency range from ∼100 Hz to ∼2 kHz [Thorne et al., 1973; Meredith et al., 2004], which is typically observed in the high-density regions of the plasmasphere [Dunckel and Helliwell, 1969; Russell et al., 1969; Thorne et al., 1973] and in plasmaspheric plumes [Chan and Holzer, 1976; Summers et al., 2008]. It has been proposed that an embryonic source for plasmaspheric hiss is chorus waves generated outside the plasmasphere, which has been verified by both ray tracing simulations [Chum and Santolík, 2005; Santolík et al., 2006a; Bortnik et al., 2008] and observations [Bortnik et al., 2009; Li et al., 2015a]. Lightning-generated whistler is another potential embryonic source of plasmaspheric hiss [Sonwalkar and Inan, 1989; Green et al., 2005]. Another generation mechanism of plasmaspheric hiss near the magnetic equator in the plasmasphere has been suggested to be linear or nonlinear wave growth theory [Li et al., 2013; Chen et al., 2014; Omura et al., 2015; Nakamura et al., 2016]. Previous statistical studies have illustrated that the occurrence and the intensity of plasmaspheric hiss significantly depend on the magnetic local time and geomagnetic activity, that is, both the occurrence and the intensity are higher on the dayside and during higher levels of geomagnetic activity [Golden et al., 2012; Kim et al., 2015; Li et al., 2015b; Hartley et al., 2018].

[1]©2019 Amercian Geophysical Union. Portions Adapted, with permission from, Z. Xia, "Statistical characteristics of ionospheric hiss waves," Xia, Z., Chen, L., Zhima, Z., Santolík, O., Horne, R. B., and Parrot, M., Geophysical Research Letters, 46.

A portion of plasmaspheric hiss (and magnetospheric chorus waves) can propagate nearly along the magnetic field lines and penetrate into the topside ionosphere as low-altitude ionospheric hiss with frequency range from 100 Hz to 1 kHz [Santolík and Parrot, 1999; Santolík et al., 2006a; Chen et al., 2017], which in turn is ionospheric manifestation of magnetospheric whistler mode emissions. This serves as a mechanism to remove whistler wave field energy of plasmaspheric hiss, in addition to two other potential mechanisms, heating electrons via Landau resonance and escaping out of the plasmasphere into exohiss. The propagation features of ionospheric hiss have been studied previously. Zhima et al. [2017] reported a conjugate observation of ionospheric hiss by Detection of Electromagnetic Emissions Transmitted from Earthquake Regions (DEMETER) and plasmaspheric hiss by THEMIS, both having similar spectral properties. Case studies showed that a portion of plasmaspheric hiss emissions can propagate vertically downward in both northern and southern hemispheres to the topside ionosphere and then turns equatorward [Santolík and Parrot, 1999, 2000; Santolík et al., 2006a]. The mechanism of the equatorward propagation has been explained as a waveguide formed by the magnetic field and plasma density dependence of whistler mode refractive index [Chen et al., 2017]. The refractive index decreases when wave frequency approaches to the multi-ion cutoff frequency f_{cutoff} in the oxygen-rich plasma at lower altitudes (corresponding to increasing magnetic field strength) and decreases with decreasing density at higher altitude away from the topside of ionospheric density peak, which results in refractive index maximum near a few hundreds of kilometers altitude and therefore the formation of a whistler waveguide. This waveguide mechanism in the ionosphere, when at work, may result in the redistribution of the ionospheric hiss wave power in the asymmetric magnetic field in the ionosphere, especially near the South Atlantic Anomaly (SAA) region. The SAA is a weak geomagnetic field region over the south Atlantic, which is caused by the asymmetry of Earth's magnetic field with respect to the Earth's rotational axis (see Appendix F). The inner radiation belt penetrates into the ionosphere in the SAA region and leads to the

enhancement of energetic particle flux in this region. Studying wave activities in the SAA region may be potentially important for inner radiation belt dynamics [Abdu et al., 1981, 2005; Benbrook et al., 1983]. The relation between ionospheric hiss and SAA will be checked in this study.

In this study, we use about 6 years of DEMETER satellite observations of waves to investigate propagation characteristics and statistical properties of ionospheric hiss emissions. In Section 6.2, we present a case study to reveal the propagation characteristics of ionospheric hiss near the SAA region. In Section 6.3, we analyze the dependence of ionospheric hiss wave power on location, magnetic local time, geomagnetic activity, and season. Finally, we use a ray tracing simulation to explain the observed features.

6.2 Ionospheric Hiss Near SAA

DEMETER was a French satellite operated by Centre National des Etudes Spatiales. It was launched in June 2004 and its mission ended in December 2010 (about 6.5 years of operating time) with a low altitude nearly Sun-synchronous circular orbit (∼10:30 and ∼22:30 LT). The altitude of the spacecraft was initially 710 km and decreased to 660 km in December 2005 [Parrot et al., 2006]. The Instrument Champ Electrique [Berthelier et al., 2006] consists of four sensors, which are spherical aluminum electrodes with a 60-mm diameter and deployed by stacer booms at approximately 4 m from the satellite. It can provide measurements of three components of electric field waveforms in Burst mode for the extremely low frequency (ELF) frequency channel (15-1,250 Hz), which covers the frequency range of low-altitude hiss of interest to our study. The Instrument Magnetic Search Coil [Parrot et al., 2006] can provide the Burst mode measurements of three-component magnetic field waveforms in the ELF channel. These two instruments provide the waveform measurements of six components of the electromagnetic fields to analyze the propagation and polarization properties of the observed electromagnetic waves [Santolík et al., 2006b].

Figure 6.1 shows an event of low-altitude electromagnetic hiss emissions observed by DEMETER satellite on 15 April 2005 on the dayside (magnetic local time around 10.2) when it passed by the SAA region and triggered the Burst mode observation. This event started from ∼16:14 UT and ended at ∼16:34 UT (lasting about 20 min), and DEMETER was flying over the geomagnetic (dipolar) latitude λ_m from approximately 50°to -24°and the geomagnetic longitude ϕ_m from ∼347°to ∼334°(shown by the magenta solid line in Figure 6.1m). The black square, triangle, and circle symbols overplotted on the magenta line denote the start time, the end time, and the time of reaching the location of minimum background magnetic field, respectively. The colored contours in Figure 6.1m exhibit the variation of the local proton cyclotron frequency (f_{CH}), which is proportional to the local magnetic field strength. The local magnetic field is obtained from the International Geomagnetic Reference Field (IGRF) model. The f_{CH} contour of 300 Hz encloses the SAA region.

Using the observed six components electromagnetic waveforms and applying fast Fourier transformation, we can obtain multicomponent 6×6 spectra matrices and then determine the wave power spectral density, the ellipticity of the magnetic field polarization, the wave vector, and the Poynting vector [Santolík et al., 2010, and references within]. Figures 6.1a and 6.1b show the power spectral density of the wave magnetic and electric field, respectively (the portion of electric power less than $5 \times 10^{-6}(mV/m)^2/Hz$) is not shown). From Figures 6.1a and 6.1b, we can see that at the high latitude (greater than ∼46°), there is a strong broadband emission above ∼600 Hz. At the lower latitude, the emission becomes narrower, and the central frequency, closely following the local f_{CH} value (shown as the black dash-dot lines), decreases with decreasing latitude. After the satellite reaches the location of the minimum background magnetic field strength (marked by the black vertical dashed line), the central frequency variation starts to reverse. Figures 6.1c and 6.1d exhibit the polar angle (θ_k) of wave vector **k** with respect to background magnetic field and the azimuthal angle (ϕ_k) of **k** (0°corresponds to radially outward direction from the Earth). The **k** vector can

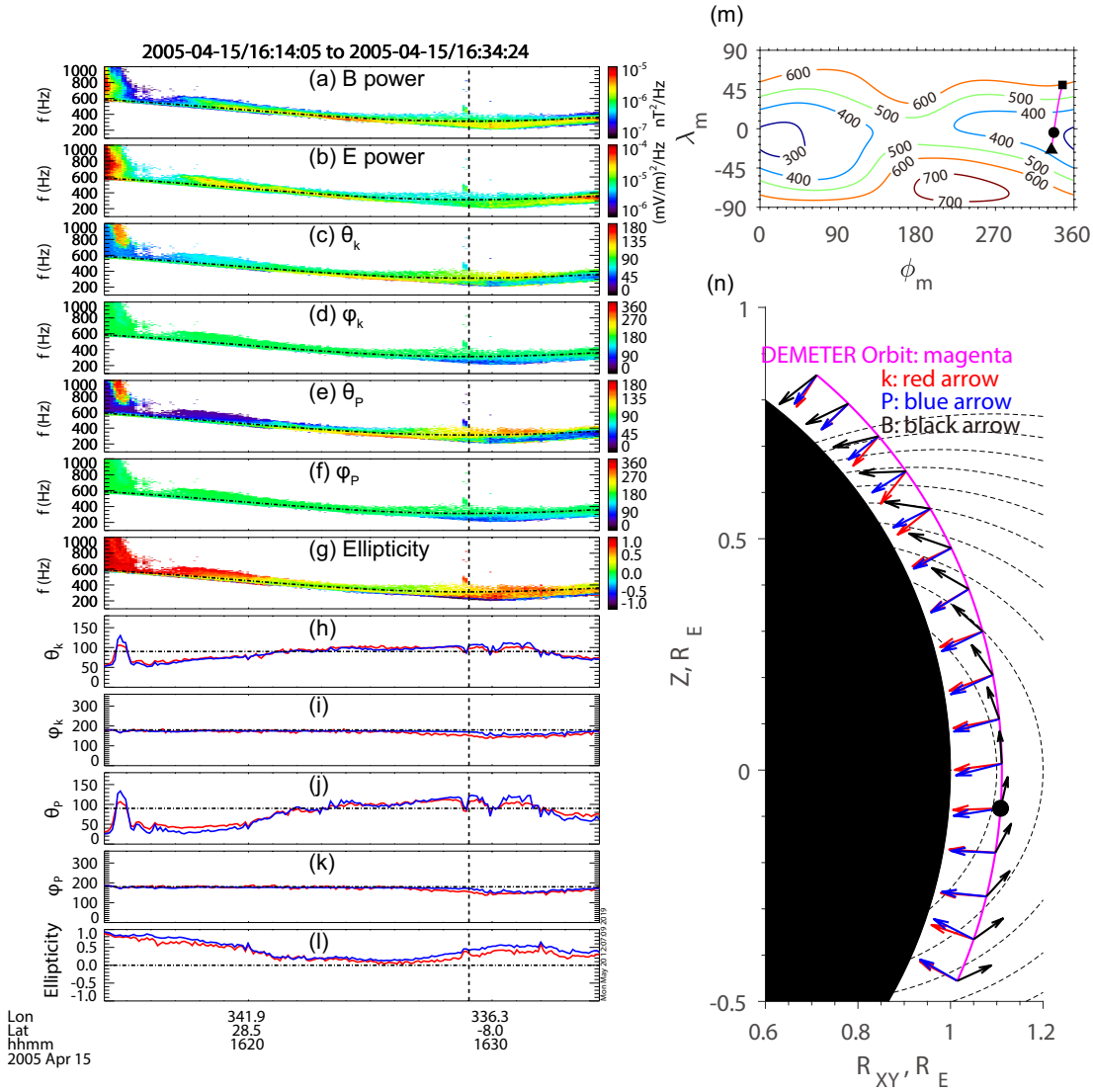

Figure 6.1. Ionospheric hiss event in April 15th, 2005 observed by DEMETER. (a) and (b) are the wave power spectra of magnetic field and electric field. (c)-(g) are the spectra of normal angle of wave vector **k**, azimuthal angle of **k**, normal angle of Poynting vector **P**, azimuthal angle of **P** and ellipticity, respectively. (h)-(l) are the mean (red) and median (blue) values of the parameters shown in (c)-(g). (m) shows the orbit of the DEMETER (magenta line) and the contours of local f_{CH}in unit of Hz. (n) is the meridional view of the DEMETER orbit (magenta line) with the directions of **k** (red arrows), **P** (blue arrows), and background magnetic field **B** (black arrows). The black dashed lines in (a)-(l) and the black circular dots in (m) and (n) represent the minimum background magnetic field point. R_{XY} denotes $(X^2 + Y^2)^{1/2}$ in the Solar magnetic coordinate system (X, Y, Z).

be determined by applying singular value decomposition methods combining with Gauss's law for magnetism and Faraday's law to the electromagnetic filed waveform data [Santolík et al., 2003b]. Figures 6.1e and 6.1f show the polar angle (θ_P) and the azimuthal angle (ϕ_P) for the Poynting vector **P**. The polar angles of **k** and **P** both change from about 50°at the high latitude region to about 90°near the equator, while both the azimuthal angles of **k** and **P** remain around 180°(pointing toward the Earth) throughout this event. The calculated ellipticity of the magnetic field polarization (Figure 6.1g) shows the right-handed polarization in the high latitude region and nearly linear polarization near the equator. To show the variations of wave propagation parameters more clearly, we add the line plots of the mean (red) and median (blue) values of the polar angle of **k**, azimuthal angle of **k**, polar angle of **P**, azimuthal angle of **P**, and ellipticity in Figures 6.1h-6.1l, respectively.

Using the mean values in Figures 6.1h and 6.1k, we plot the **k** and **P** vectors projected onto the meridional plane in the Solar magnetic coordinate system (Figure 6.1n). In Figure 6.1n, the magenta solid line denotes the orbit of the satellite with a black solid dot marking the location of the minimum magnetic field strength. The red, blue, and black arrows represent **k**, **P**, and the background magnetic field (**B**) direction vectors, respectively. The black dashed lines show the direction of background magnetic field. One can see that both **k** and **P** vectors point downward toward the Earth. They have southward (northward) component in the region north (south) of the minimum magnetic field location. Such latitudinal dependence of the **k** and **P** vector directions shows that the ionospheric hiss can propagate toward lower latitude region where the magnetic field strength is minimized.

6.3 Statistical Study of Hiss Power Distribution

Using about 6 years of observation from DEMETER, we perform a statistical analysis of the ionospheric hiss wave power distribution on location (geomagnetic latitude and longitude), magnetic local time, geomagnetic activity, and season. The observations of electromagnetic

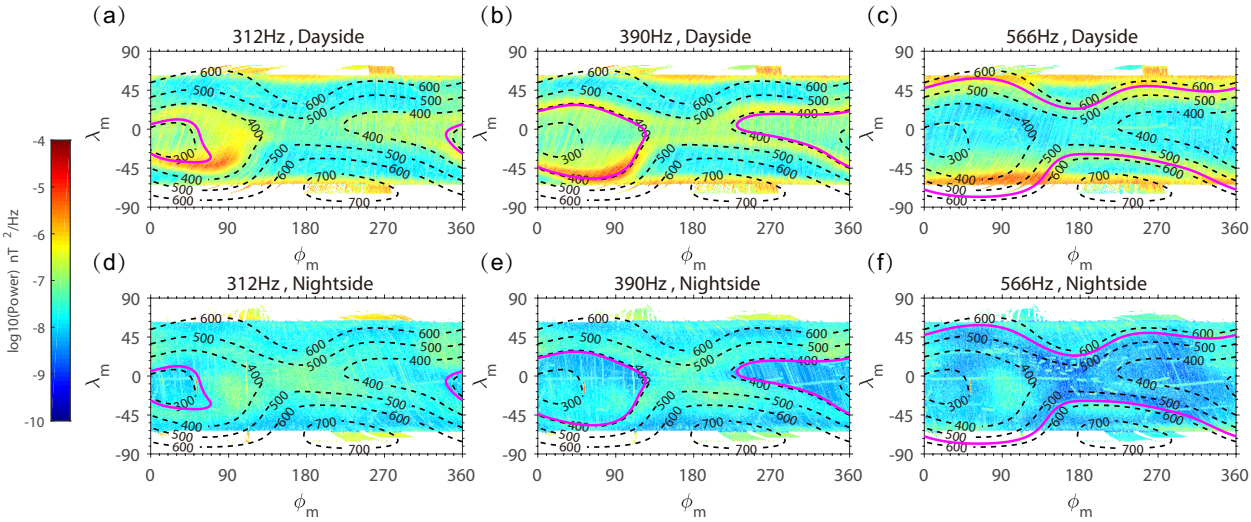

Figure 6.2. The global distributions of the mean value of wave magnetic field power (filled color) in geomagnetic coordinates at the DEMETER altitude for three frequency bands: 312, 390, 566 Hz.
The upper panels are for dayside, and the bottom panels are for nightside. The dashed contours stand for the distribution of the local f_{CH} at the DEMETER altitude, while the magenta lines stand for the contours where the local f_{CH} equals to the corresponding wave frequency.

wave power are divided into 360 bins in geomagnetic longitude, 181 bins in geomagnetic latitude, two magnetic local times (dayside and nightside), three geomagnetic activity levels (characterized by auroral electrojet (AE) index, including $AE \leq 100$, $100 < AE \leq 300$, $AE > 300$), and four boreal seasons (spring over a range of day of year from 35 to 125, summer from 126 to 217, autumn from 218 to 308, and winter from 309 to 34 of next year). The statistical results are shown by Figures 6.2-6.4.

Figure 6.2 shows the global distribution of the logarithm of the average wave magnetic field power in geomagnetic longitude ϕ_m (x axis) and latitude λ_m (y axis) for two magnetic local times (dayside and nightside in upper and bottom panels, respectively) and three wave frequencies (312, 390, and 566 Hz from the left to the right). The dashed black contours represent the spatial variation of local f_{CH}, which is obtained from the IGRF model. The

f_{CH} contours of values equal to the three wave frequencies are also plotted as the magenta solid contours for reference, from the left to right panels.

Comparing the wave power between the upper and lower panels, we can see that the ionospheric hiss at all the three frequencies is 2-3 orders of magnitude more intense on the dayside than nightside. This day-night distribution feature of ionospheric hiss is similar to that of the plasmaspheric hiss [Golden et al., 2012; Kim et al., 2015; Li et al., 2015b; Hartley et al., 2018], which is consistent with the proposed idea [Chen et al., 2017] that the ionospheric hiss originates primarily from the whistler mode plasmaspheric hiss. Such local time distribution of the ionospheric hiss with weaker intensity at nightside also excludes the possibility of electromagnetic sources below the ionosphere (such as lightning activities), because the collisional damping of whistler mode is stronger on the dayside than nightside.

By examining wave power distribution on the dayside (Figure 6.2, upper panels), one can see a strong dependence of the spatial distribution on wave frequency. The wave power at 312 Hz has the strongest power just outside the region where local proton cyclotron frequency is close to that frequency and around the SAA region (Figure 6.2a). As wave frequency increases, the region with strong wave power moves toward the higher latitude region. It should be noted that, for all three frequencies, there is a secondary band of intense wave power at relatively high latitude near 60°. For smaller frequencies (Figures 6.2a and 6.2b), the low-latitude band tracks f_{CH} fairly well and is separated from the high-latitude band. For higher frequency (Figure 6.2c), the two bands merge near the magnetic longitude of SAA, while remain separated away the SAA (over the range of ϕ_m from ∼150°to ∼250°), where the proximity of the low-latitude band frequency near f_{CH} is still noticeable. We will explain this frequency dependence in next section.

Figure 6.3 shows the distribution of average power spectral density on the dayside for the same three different frequencies as Figure 6.2 under three different geomagnetic activity levels (top: $AE \leq 100$, middle: $100 < AE \leq 300$, and bottom: $AE > 300$). One can see that the

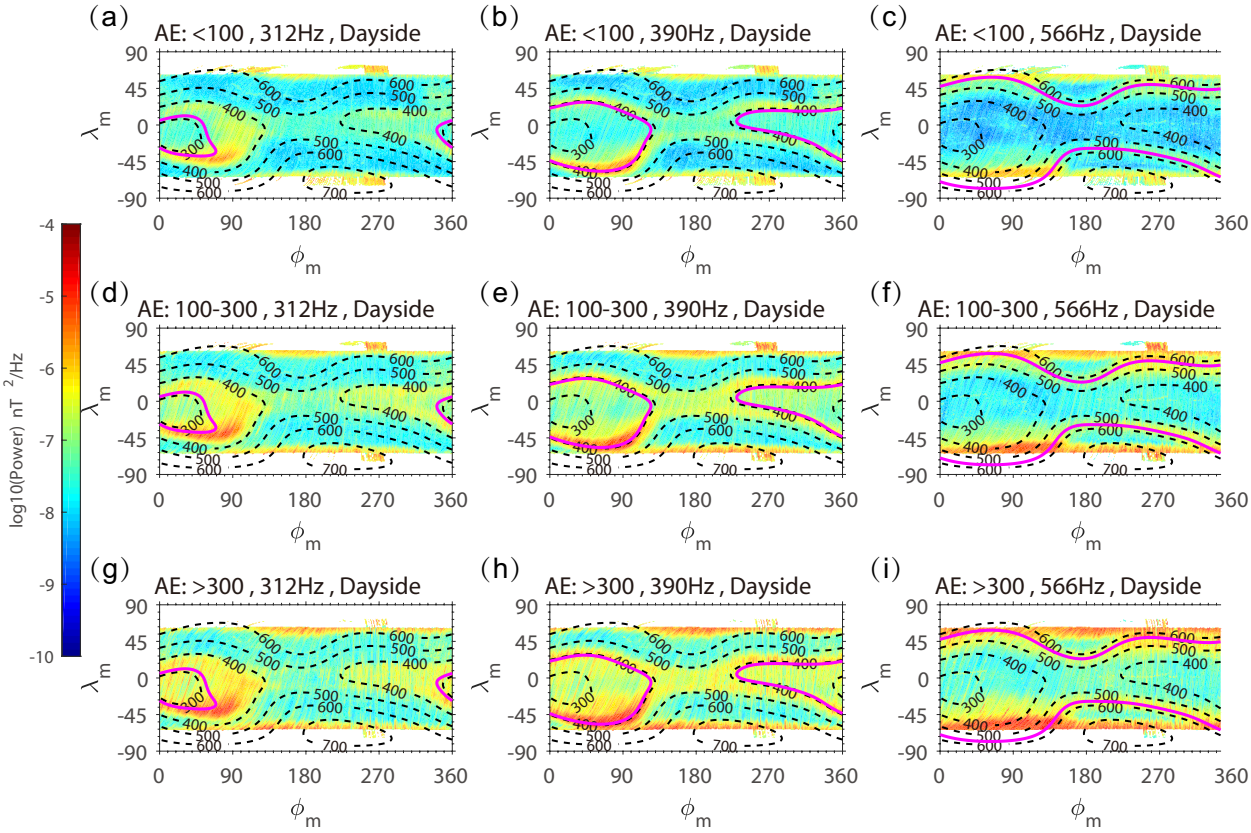

Figure 6.3. Wave power distribution in geomagnetic coordinates on the dayside for the same frequencies as Figure 6.2 and under three different geomagnetic activity levels: $AE < 100$ (top), 100≤AE≤300 (middle), and $AE > 300$ (bottom).

ionospheric hiss power shows significant dependence on the geomagnetic activity level. Power spectral density at all the frequencies of both lower and upper latitude bands is enhanced under higher AE index condition. Such geomagnetic activity dependence of ionospheric hiss is consistent with the idea of plasmaspheric hiss as its source, since plasmaspheric hiss wave amplitude increases under higher geomagnetic activity levels [Golden et al., 2012; Kim et al., 2015; Li et al., 2015b; Hartley et al., 2018].

The seasonal dependence of ionospheric wave power is shown by Figure 6.4. Figures 6.4a-6.4d show the distributions of ionospheric wave power spectral densities at 312 Hz on the dayside for the four seasons. Since the season is determined by geographic location,

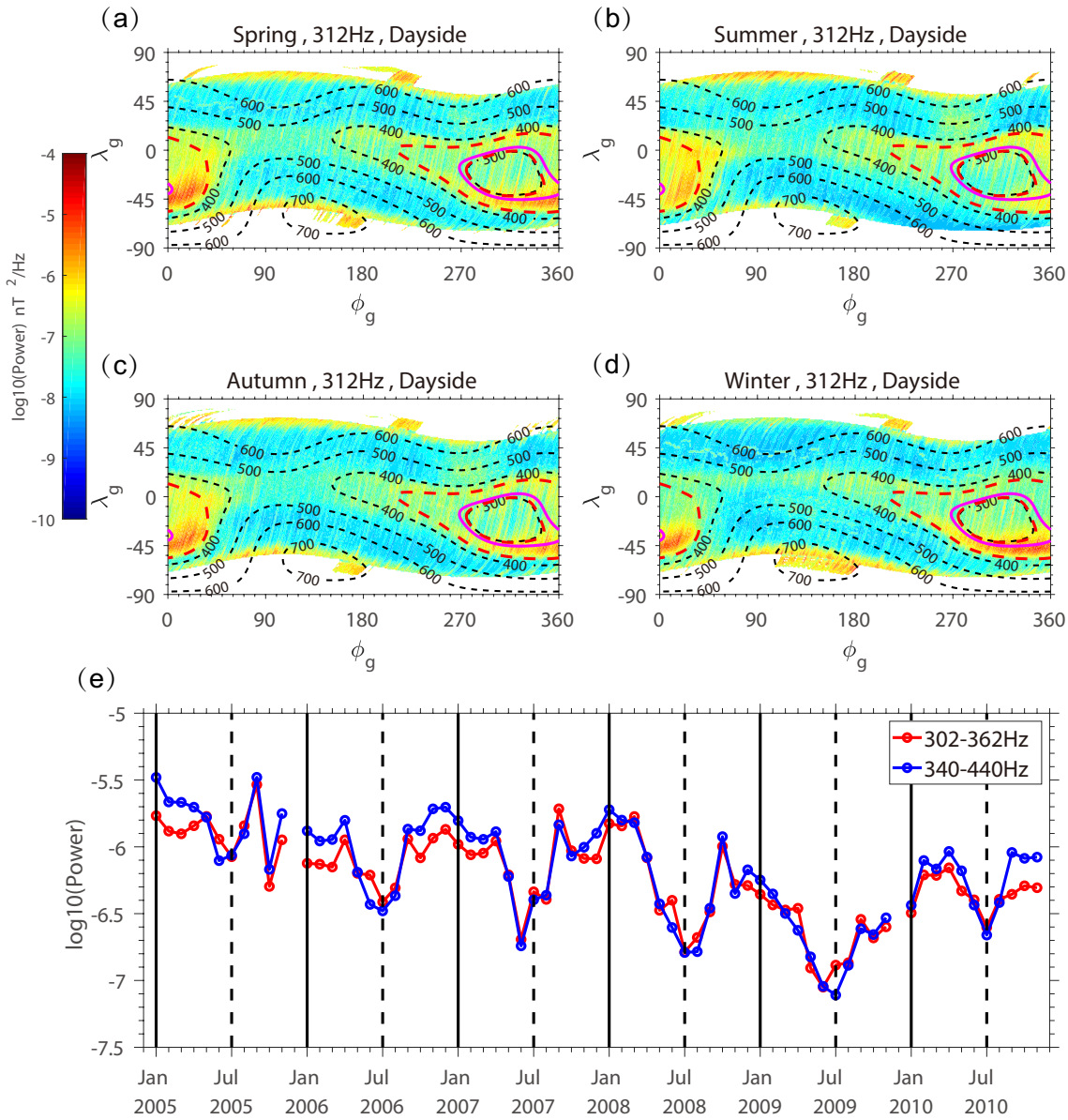

Figure 6.4. Wave power distribution in geographic coordinates on the dayside for 312-Hz frequency and four boreal seasons.
(a) Spring (day of year [doy]: 35 to 125), (b) Summer (doy: 126 to 217), (c) Autumn (doy: 218 to 308), and (d) Winter (doy: 309 to 34). (e) shows the annual variations of the mean values of 312-Hz wave power inside the region with local $f_C H$ between 302 and 362 Hz (red line) and 390-Hz wave power inside the region with local $f_C H$ between 340 and 440 Hz (blue line). The gaps in December in 2005 and 2009 are due to lack of data.

this distribution is mapped in the geographic coordinates. Two red dashed contours corresponding to local f_{CH} equaling to 302 and 362 Hz are added. The wave power in the region enclosed by the two red dashed contours in the southern hemisphere is strong and shows significant seasonal dependence with strongest intensity in local summer (Figure 6.4d, boreal winter) and weakest intensity in local winter (Figure 6.4b, boreal summer). To confirm this seasonal dependence, we calculate the mean wave power in the region between the two red dashed contours in the southern hemisphere and plot its annual variation as the red solid line in Figure 6.4e. The result indicates that the mean wave power varies periodically with minimum values near July (local winter) and maximum values near January (local summer), where the maximum to the minimum ratio is on the order of $10^{1/2}$ - 10^{1}. We also check the mean power for 390-Hz wave in the region with local f_{CH} between 340 and 440 Hz in the southern hemisphere and plot its variation as the blue line in Figure 6.4e. The mean power of 390-Hz wave shows similar annual variation as that of the 312-Hz wave. Thus, we conclude that the power of ionospheric hiss wave is stronger in local summer than in local winter. Meredith et al. [2006], however, have indicated that the intensity of low frequency (<2 kHz) plasmaspheric hiss is strongest at equinoxes. Possible explanation for the seasonal dependence of the ionospheric hiss intensity is through the seasonal variation of the f_{cutoff}, which is determined by the local ion composition. In local summer, the ion composition is dominated by O^+ around the altitude of DEMETER orbit and f_{cutoff} nearly equals to f_{CH}. In local winter, O^+ concentration decreases significantly (refer to the International Reference Ionosphere model; [Bilitza, 2018]) and leads f_{cutoff} significantly smaller than f_{CH}. Thus, for a given wave frequency, wave reflection (where wave frequency is near f_{cutoff}) takes place at lower altitudes in local winter than in local summer, leading to more attenuation because of longer propagation path and enhanced damping rate. It is also interesting to point out, from Figure 6.4e, that ionospheric hiss wave intensity reached a minimum in 2009, which is the year of solar minimum in solar cycle 23. This solar cycle dependence is also consistent with that of plasmaspheric hiss [Golden et al., 2011].

6.4 Ray Tracing Model Analysis

In Section 6.3, we have demonstrated the dependence of ionospheric hiss wave power on magnetic local time and geomagnetic activity. This dependence is consistent with the theory that the ionospheric hiss originates primarily from the plasmaspheric hiss, as discussed above. The frequency dependence of spatial distribution of ionospheric hiss wave power can also be explained by propagation mechanism of whistler-mode emission from the magnetosphere into the ionosphere and inside the ionosphere. This propagation mechanism has been demonstrated by Chen et al. [2017]. A portion of broadband plasmaspheric hiss waves can propagate nearly along magnetic field lines into the topside ionosphere at high latitude regions as type I ionospheric hiss with broadband spectra. Then the type I ionospheric hiss turns equatorward and evolves into type II ionospheric hiss with a narrow frequency band near local proton cyclotron frequency (as the event shown in Figure 6.1). The narrowband type II emission was explained as waveguide, as demonstrated below.

We use the same HOTRAY ray tracing code [Horne, 1989] as that used in Chen et al. [2017] with a dipole magnetic field and a diffusive equilibrium plasma density model [Bortnik et al., 2011, and references within]. We adopt as our source plasmaspheric hiss waves located at the equator of $L = 3$. The source wave frequency varies from 300 to 700 Hz, and the initial wave normal angle varies from 9°to 90°. Ray tracing is terminated when the wavelength is comparable to spatial scale of background field and plasma variations. Only ray paths of those waves that penetrate into the ionospheric altitude (∼700 km) are shown in Figure 6.5a. A zoom-in view near the ionosphere is shown in Figure 6.5b. Different colored solid lines represent the wave paths for different frequencies, and the colored dashed lines denote the contours of local f_{cutoff} equaling to corresponding wave frequencies. The black dashed lines show the topology of dipole field lines, and the magenta solid line indicates the altitude of DEMETER satellite. Figure 6.5c shows the directions of $\mathbf{k}$ (red arrow), $\mathbf{P}$ (blue arrow), and $\mathbf{B}$ (black arrow) at several selected points of a ray with 400-Hz wave frequency. Both $\mathbf{k}$ and $\mathbf{P}$

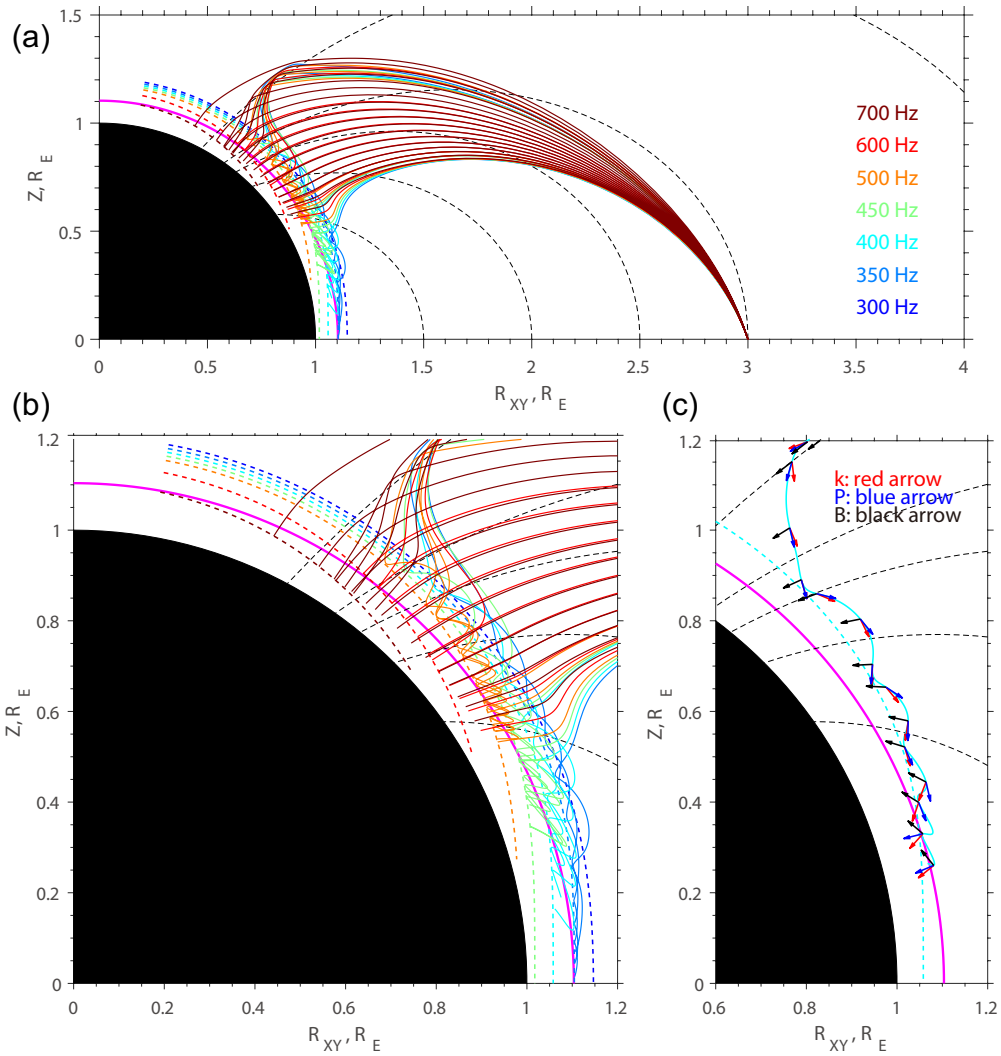

Figure 6.5. Ray tracing model results of waves originating at $L = 3$ for different frequencies (300-700 Hz) and initial wave normal angles (9°to 90°) shown in a meridional plane. Only ray paths that reach the ionospheric altitude are shown. Colored solid lines represent the wave propagation paths, and the colored dashed lines stand for the locations where local f_{cutoff} equaling to the corresponding wave frequency (color-coded). The magenta solid line shows the orbit of the DEMETER satellite, and the black dashed lines are the background magnetic field lines. (b) is the zoom-in plot of (a) in the ionospheric region. (c) shows the directions of $\mathbf{k}$, $\mathbf{P}$, and $\mathbf{B}$ at several selected points of a ray with 400-Hz wave frequency.

vectors are directed downward and equatorward at low latitudes and are nearly perpendicular to the background magnetic field, which is consistent with the observational results in Figure 6.1. From Figure 6.5, we can see that the hiss waves penetrate into the ionosphere at high latitudes ($\sim$25°to $\sim$60°) almost vertically downward along the magnetic field lines. When reaching the corresponding f_{cutoff} lines at the ionospheric altitude, ray paths of different frequencies start to separate. The waves with lower frequencies reflect upward at higher altitude region and are trapped inside the waveguide to propagate equatorward, while the higher frequency waves enter the waveguide at lower altitude. Because waveguide places lower and upper altitude limits for those waves, the waves can be only seen over a limited range of latitude at a fixed altitude. Therefore, such frequency-dependent waveguide propagation not only explains why the ionospheric hiss at low latitude region is observed by DEMETER (e.g., Figure 6.1) with a narrow frequency band but also explains why this band is near local proton cyclotron frequency (which is close to f_{cutoff} at DEMETER altitude) and why the central frequency tends to decrease with decreasing latitude.

For more realistic IGRF geomagnetic field, the minimum magnetic field surface is not necessarily the magnetic equator, especially around the SAA region. For the individual event shown Figure in 6.1, the minimum magnetic field exists in the SAA region, and the hiss waves from both northern and southern hemispheres eventually propagate into the SAA region. The statistical results in Section 6.3 support that SAA region is favorable to trap ionospheric hiss waves of 400 Hz and below (Figure 6.3, the left and middle columns), while the waves at higher frequencies can be trapped at all magnetic longitudes.

6.5 Conclusions and Discussion

In this chapter, we present a case study from DEMETER satellite observations near the SAA region to understand wave propagation features of ionospheric hiss. Then we use about 6 years of observations of DEMETER satellite to undertake a statistical study of the wave

power distribution of ionospheric hiss on location (geomagnetic latitude and longitude), magnetic local time (day and night), geomagnetic activity, and season. A ray tracing model simulation is also applied to explain the latitudinal dependence of wave frequency band. The main conclusions of this study are summarized as the following.

1. In the case study, the intense hiss wave power concentrates over a narrow frequency band that decreases from about ∼600 Hz at the high latitude region to ∼300 Hz near the equator, which coincides to the variation of local proton cyclotron frequency f_{CH}. The waveform measurement shows that the wave propagates obliquely to the background magnetic field and equatorward from high latitude region.

2. The low-altitude ionospheric hiss power tends to be stronger on the dayside than nightside, and under higher geomagnetic activity conditions. Those characteristics are consistent with the distribution of plasmaspheric hiss. The ionospheric hiss power shows seasonal variation with stronger power in local summer than in local winter.

3. The wave power is confined near the region where the local proton cyclotron frequency f_{CH} is near the wave frequency. This is caused by the propagation within a waveguide structure formed by the variation of plasma density and cutoff frequency.

4. A ray tracing simulation demonstrates that waveguide can explain the latitudinal dependence and narrowness of the ionospheric hiss frequency band.

Emissions that can reach the ionospheric altitude will redistribute the wave energy according to wave frequency through frequency-dependent waveguide in the topside ionosphere, resulting in that the waves at low latitude region are found with wave frequency near local proton cyclotron frequency. Our statistical analysis not only reveals such frequency-dependent characteristics but also demonstrates the dependence of ionospheric hiss wave power on local time, geomagnetic activity, and season. All those statistical results support the proposed idea that those emissions originate primarily from the plasmaspheric hiss.

Because of frequency-dependent propagation, the lower frequency waves (below 400 Hz) are trapped only near SAA region, while the upper frequency waves are trapped at all magnetic longitudes. How important these waves near SAA are in facilitating the precipitation loss remains to be found out.

CHAPTER 7

SUMMARY AND WORK PROPOSAL

7.1 Summary

This dissertation mainly focuses on the study of VLF whistler mode waves modulated by ULF waves. Background information about the Earth's magnetosphere, as well as the VLF whistler waves, ULF waves and their modulation effect, is introduced in Chapter 1. The main results of this dissertation are summarized as follows:

In Chapter 2, we present Van Allen Probes observation of ULF wave modulating chorus wave intensity, which occurred deep in the magnetosphere. The ULF wave shows fundamental poloidal mode signature and mirror mode compressional nature. The observed ULF wave can modulate not only the chorus wave intensity but also the distribution of both protons and electrons. Linear growth rate analysis shows consistency with observed chorus intensity variation at low frequency ($f <\sim 0.3 f_{\mathrm{ce}}$), but cannot account for the observed higher-frequency chorus waves, including the upper band chorus waves. This suggests the chorus waves at higher-frequency ranges require nonlinear mechanisms. In addition, we use combined observations of Radiation Belt Storm Probes (RBSP) A and B to verify that the ULF wave event is spatially local and does not last long.

In Chapter 3, we simulate a self-consistent magnetic field that satisfies force balance with a model ring current that is radially localized, axisymmetric, and has anisotropic plasma pressure. We find that the magnetic field dip forms near the high plasma pressure region with plasma $\beta >\sim 0.6$, and the formed magnetic dip becomes deeper for larger plasma β and also slightly deeper for larger anisotropy. We perform linear analysis on a pool of self-consistent equilibria for second harmonic compressional poloidal modes of sufficiently high azimuthal wave number. We investigate the effect of anisotropic pressure on the eigenfrequency of the poloidal modes and the characteristics of the compressional magnetic field component. We

find that the eigenfrequency is reduced at the outer edge of the thermal pressure peak and increased at the inner edge. The compressional magnetic field component occurs primarily within 10°of the equator on both the inner and outer edges, with stronger compressional magnetic field component on the outer edge. Larger β and smaller anisotropy can increase the change of eigenfrequency and the strength of the compressional magnetic field component. The critical condition on plasma β and pressure anisotropy of an Alfvén ballooning instability is also identified.

In Chapter 4, we use nearly 2 years' observations of three THEMIS satellites (A, D, E) and over 5.5 years' observations of two Van Allen Probes (A, B) to statistically study the modulations of chorus emissions by the background magnetic field and plasma density. The modulation events are identified automatically by calculating the correlation coefficients between the magnetic field strength (or plasma density) and the chorus emission intensity (calculated by integrating the magnetic wave power spectrum density through 0.1 to 0.8 electron cyclotron frequency f_{ce}). The modulation events are divided into three types according to whether the chorus intensity is highly correlated to the variations of magnetic field strength (Type B), plasma density (Type N) or both (Type NB). The three types are also sorted to eight subtypes according to the signs of correlation coefficients. The proportions of the types B and N are almost equal ($\sim 1/3$) and slightly larger than that of type NB ($\sim 1/5$) for the THEMIS observations while for the Van Allen Probes observations most events are Type N. The chorus intensity is mostly correlated to the magnetic field strength negatively and plasma density positively. The spatial distribution of modulation events matches that of the chorus emissions very well, which is the number of modulation events is largest at the dawn sector for all the three types. Finally, we analyze the relationships between chorus intensity and amplitudes of perturbations of the magnetic field and plasma density. The results indicate that the chorus intensity is larger when the amplitude of the magnetic field perturbation is larger but has little dependence on the amplitude of plasma density perturbation.

Besides the above studies, two corresponding studies are also included in this dissertation. In Chapter 5, we use the 2-D axisymmetric equilibrium model to calculate self-consistent magnetic field in force balance with a Gaussian thermal pressure distribution characterized by four input parameters: the ratio between plasma pressure and magnetic pressure (β) at the pressure peak β_0, the radial location of the pressure peak L_0, the width of the half peak pressure σ_0, and the equatorial pressure anisotropy A_e. Using the modeled magnetic field, we find that the magnetic field perturbation increases with increasing β_0 and decreasing σ_0 while the magnetic curvature perturbation increases with increasing A_e, β_0, σ_0 and decreasing L_0. For energetic particles the change of magnetic gradient drift motion is much greater than that of curvature drift motion. The magnetic dip structure formation requires a critical β value that increases with increasing σ_0 and decreasing L_0. Despite the unavailability of observations in the existing literature to check the condition of magnetic dip formation, such condition will be checked against observations as a future study. Finally, we also use 3-D ring current-atmosphere interactions model with self-consistent magnetic field model to illustrate the effect of azimuthal pressure distribution, which is relevant to asymmetric ring current.

In Chapter 6, we use the observations of electromagnetic waves by Detection of Electromagnetic Emissions Transmitted from Earthquake Regions satellite to investigate propagation characteristics of low-altitude ionospheric hiss. In an event study, intense hiss wave power is concentrated over a narrow frequency band with a central frequency that decreases as latitude decreases, which coincides to the variation of local proton cyclotron frequency f_{CH}. The wave propagates obliquely to the background magnetic field and equatorward from high latitude region. We use about $\sim$6 years of observations to statistically study the dependence of ionospheric hiss wave power on location, local time, geomagnetic activity, and season. The results demonstrate that the ionospheric hiss power is stronger on the dayside than nightside, under higher geomagnetic activity conditions, in local summer than local winter. The wave power is confined near the region where the local f_{CH} is equal to the wave

frequency. A ray tracing simulation is performed to account for the dependence of wave power on frequency and latitude.

7.2 Future Work

The future works we plan to are listed below:

1. A theoretical study can be performed combining with FLR model simulation, to investigate the underlying mechanism of the VLF whistler waves modulated by the background magnetic field and plasma density. The FLR model can output the properties of ULF waves and corresponding electron distribution perturbation, from which we can obtain the linear growth rate of whistler modes. We can also investigate the differences in VLF modulation effects due to various FLR modes (toroidal and poloidal modes at various harmonics).

2. Conjugated observations of a large scale ULF wave by multiple data set from magnetospheric spacecraft (Van Allen Probes, THEMIS, Cluster, NOAA GOES, etc.), low earth orbit satellites (DMSP, NOAA POES, etc.), and ground magnetometers (THEMIS GMAG stations) can be used to extract global properties of ULF wave observation, which can be compared against our field line resonance model.

3. Magnetic dip structure and the corresponding radial variation of plasma pressure can be extracted through in-situ observation and then can be used to verify our theoretical theory about the formation of the magnetic dip structure. THEMIS and ARASE satellites may be suitable spacecraft for this study.

4. A follow-up study of the statistic characteristics of low frequency ionospheric hiss near SAA is to search for any observational effect of such waves in facilitating precipitation loss of charged particles. DEMETER particle data may be suitable here. DEMETER wave data can be also used to obtain statistic distribution of whistler waves generated by lightning activity in the lower atmosphere and whistler waves injected by artificial ground-based VLF

transmitters [Zhang et al., 2018]. Both whistlers have imprints in the magnetosphere and contribute to energetic electron precipitation.

APPENDIX A

MODES OF ULF WAVES UNDER MHD ASSUMPTION

In a Cartesian system, consider a simple case with a uniform background magnetic field $\mathbf{B}_0 = B_0\hat{\mathbf{z}}$, constant thermal pressure p_0 and constant plasma density ρ_0. Assume the plasma is collisionless and cold with initial velocity $\mathbf{u}_0 = 0$. The MHD equations can be linearized to the first order as

$$\frac{\partial \mathbf{b}_1}{\partial t} = \nabla \times (\mathbf{u}_1 \times \mathbf{B}_0), \tag{A.1}$$

$$\rho_0 \frac{\partial \mathbf{u}_1}{\partial t} = -\nabla p_1 + \frac{1}{\mu_0}(\nabla \times \mathbf{b}_1) \times \mathbf{B}_0, \tag{A.2}$$

$$\frac{\partial \rho_1}{\partial t} = -\rho_0 \nabla \cdot \mathbf{u}_1, \tag{A.3}$$

$$\nabla \cdot \mathbf{b}_1 = 0, \tag{A.4}$$

$$\frac{\partial p_1}{\partial t} = -\gamma p_0 \nabla \cdot \mathbf{u}_1, \tag{A.5}$$

where $\mathbf{b}_1$, $\mathbf{u}_1$, p_1 and ρ_1 are the first order perturbations of magnetic field, plasma velocity, pressure and density respectively. Let the plasma wave be represented in form of $\exp\left[i(\mathbf{k} \cdot \mathbf{r} - \omega t)\right]$, the MHD equations can be derived to [e.g. Roberts, 1985]:

$$[\omega^4 - \omega^2 k^2 (c_s^2 + V_A^2) + c_s^2 V_A^2 k^4 \cos^2\theta](\mathbf{k} \cdot \mathbf{u}_1) = 0, \tag{A.6}$$

where $c_s^2 = \gamma p_0 / rho_0$ is the square of sound speed, $V_A^2 = B_0^2/\mu_0\rho_0$ is the square of the Alfvén speed and θ is the wave normal angle (angle between $\mathbf{B}_0$ and $\mathbf{k}$). If the wave vector is perpendicular to the velocity perturbation ($\mathbf{k} \cdot \mathbf{u}_1 = 0$), which can yield to the following equations:

$$\mu_0 \rho_0 \omega^2 \mathbf{u}_1 = (\mathbf{k} \cdot \mathbf{B}_0)^2 \mathbf{u}_1, \tag{A.7}$$

$$\Rightarrow \omega^2 = \frac{B_0^2}{\mu_0 \rho_0} k^2 \cos^2\theta = k_z^2 V_A^2, \tag{A.8}$$

where $k_z = k\cos\theta$ is the component of $\mathbf{k}$ parallel to $\mathbf{B_0}$. Equation (A.8) is dispersion relation of Alfvén wave and describes transverse waves with group velocity parallel to $\mathbf{B}_0$. If $(\mathbf{k}\cdot\mathbf{u}_1 \neq 0)$, the Equation (A.8) yields:

$$\omega^4 - \omega^2 k^2 (c_s^2 + V_A^2) + c_s^2 V_A^2 k^4 \cos^2\theta = 0, \tag{A.9}$$

which is the magnetoacoustic dispersion relation and corresponds to the compressional wave modes. The solutions of (A.9) are:

$$\frac{\omega^2}{k^2} = \frac{1}{2}(c_s^2 + V_A^2) \pm \frac{1}{2}\sqrt{(c_s^2 + V_A^2)^2 - 4c_s^2 V_A^2 k^4 \cos^2\theta}. \tag{A.10}$$

The positive and negative roots describe the fast and slow modes respectively. When $\theta = \pi/2$, there is no slow mode propagation, which means the slow mode can not propagate perpendicular to $\mathbf{B}_0$. The dispersion relation of fast mode is $\omega^2/k^2 = c_s^2 + V_A^2$, which is the maximum speed fast mode can reach. When $\theta = 0$, the dispersion relations of fast mode and slow mode are $\omega^2/k^2 = V_A^2$ and $\omega^2/k^2 = c_s^2$ respectively. Under the assumption of low β plasma with nearly no plasma pressure, the sound speed $c_s = 0$ and only Alfvén mode and fast mode remain, whose dispersion relations are $\omega_A/k_z = V_A$ and $\omega_f^2/k^2 = V_A^2$ respectively.

Now let's consider the field line resonance (FLR), which can couple the energy form the fast mode to the Alfvén mode. Under the low β condition, Equations (A.1) and (A.2) can be rewritten as formation for plasma displacement ξ as:

$$\frac{1}{V_A^2}\frac{\partial^2 \xi_x}{\partial t^2} - \frac{\partial^2 \xi_x}{\partial z^2} = -\frac{1}{B_0}\frac{\partial b_z}{\partial x}, \tag{A.11}$$

$$\frac{1}{V_A^2}\frac{\partial^2 \xi_y}{\partial t^2} - \frac{\partial^2 \xi_y}{\partial z^2} = -\frac{1}{B_0}\frac{\partial b_z}{\partial x}, \tag{A.12}$$

$$b_z = -B_0\left(\frac{\partial \xi_x}{\partial x} + \frac{\partial \xi_y}{\partial y}\right). \tag{A.13}$$

For the Equations (A.11) and (A.12), the left hand sides represent the simple harmonic oscillations and the right hand sides are the driving terms which are terms of the spatial gradient of the compressional fast mode disturbance b_z. Under a cartesian coordinate system with z axis parallel to $\mathbf{B}_0$ and x axis points radially away from the Earth, the transverse displacements ξ_x and ξ_y of Alfvén waves correspond to the poloidal mode and toroidal modes respectively. These equations describe the relation between fast mode waves and Alfvén waves in the FLR.

APPENDIX B

BASIC EQUATION FOR EIGENPERIOD ANALYSIS OF POLOIDAL MODE IN COLD PLASMA LIMIT

The equation to calculate the eigenperiod of poloidal mode FLR for the Earth's dipole field is:

$$H_2 \partial/\partial\mu (H_1 \partial\epsilon_\phi/\partial\mu) + (\omega^2/A^2)\epsilon_\phi = 0$$

.

where $H_1 = (\nu r^3)^{-1}$, $H_2 = \nu(1 + 3\cos^2\theta)r^{-3}$, $\epsilon_\phi = r\sin\theta E_\phi$ and $A = B/\sqrt{\mu_0\rho}$ is the Alfvén velocity. $\omega = 2\pi/T$ is the angular eigenfrequency, where T is the eigenperiod we want. θ is the magnetic colatitude and r is the radial distance from the origin of the dipole field. (ν, μ, ϕ) are orthogonal dipole coordinates defined as: $\nu = (\sin^2\theta)/r$, which is constant along a dipole field line and the unit vector $\mathbf{e}_\nu$ is in the direction of the principal normal to the field line; $\mu = (\cos\theta)/r^2$, which is constant along an orthogonal trajectory of the dipole field lines and the unit vector $\mathbf{e}_\mu$ is parallel to the field line; ϕ is the ordinary azimuthal spherical coordinate and the unit vector $\mathbf{e}_\phi$ is in the azimuthal direction (see Figure B.1). Thus E_ϕ is the azimuthal electric field component and is set to be 0 at the two ends of the field line as the boundary condition. Note that when the dependence of the magnetic field and Alfvén velocity on the field line vanishes, the above equation returns to the equation for Alfvénic mode in a uniform MHD.

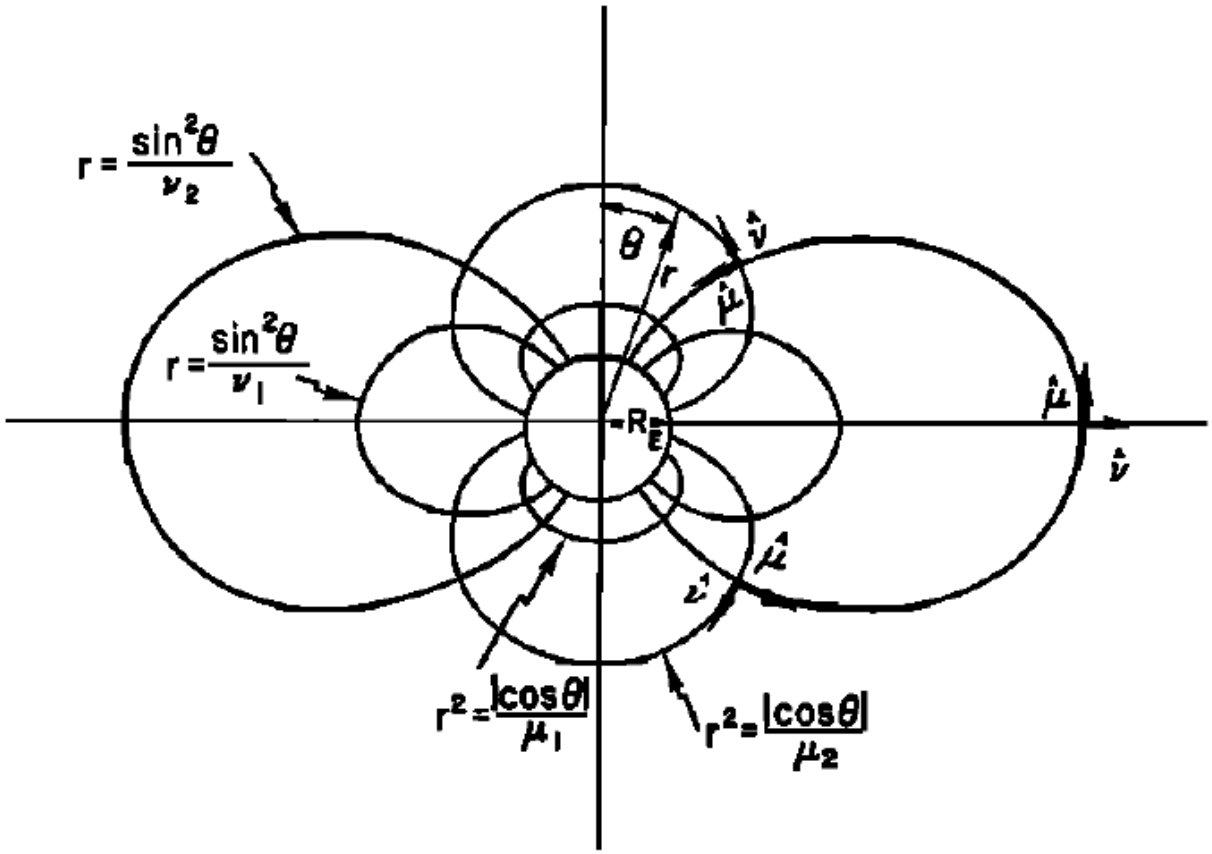

Figure B.1. An illustration of the orthogonal dipole coordinate system [Cummings et al., 1969].

APPENDIX C

LINEAR GROWTH RATE

Whenever the temporal growth rate γ is much smaller than ω, the dispersion matrix D to the first order can be expressed as [Kennel, 1966; Chen et al., 2010]

$$D = D^{(0)} + iD_i,$$

and consequently, we can approximate

$$\gamma = -\frac{D_i}{\frac{\partial D^{(0)}}{\partial \omega}},$$

where

$$\begin{aligned}
D_i = &-\frac{2\pi^2 e^2}{\varepsilon_0 m_s}\frac{1}{\omega|k_\parallel|}\int_0^\infty v_\perp dv_\perp \int_{-\infty}^{+\infty} dv_\parallel \sum_m \delta(v_\parallel - \frac{\omega - m\Omega_s}{k_\parallel}) \\
&\cdot [G_1(f_s)((P - n^2\sin^2\theta)[2(L-n^2)v_\perp J_{m+1}^2 \\
&+ 2v_\perp(R-n^2)J_{m-1}^2 + n^2\sin^2\theta v_\perp(J_{m+1}-J_{m-1})^2] \\
&- n^2\cos\theta\sin\theta[2v_\parallel J_m(J_{m+1}(R-n^2) + J_{m-1}(L-n^2)) \\
&+ n^2\cos\theta\sin\theta v_\perp(J_{m+1}-J_{m-1})^2]) \\
&+ G_2(f_s,m)(4v_\parallel J_m[(L-n^2)(R-n^2) + n^2\sin^2\theta(S-n^2)] \\
&- 2n^2\cos\theta\sin\theta[(R-n^2)v_\perp J_{m-1} + (L-n^2)v_\perp J_{m+1}])]
\end{aligned}$$

where m_s and Ω_s are the mass and cyclotron frequency of species s; J_m are bessel functions with order m and argument $x = k_\perp v_\perp/\Omega_s$; L, R, S and P are the standard Stix coefficients; ω, θ, and $n = kc/\omega$ are wave frequency, wave normal angle, and refractive index.

$$\begin{aligned}
G_1 &= \frac{\partial f_s}{\partial v_\perp} - \frac{k_\parallel}{\omega}(v_\parallel\frac{\partial f_s}{\partial v_\perp} - v_\perp\frac{\partial f_s}{\partial v_\parallel}) \\
G_2 &= J_m[\frac{\partial f_s}{\partial v_\parallel} + \frac{m\Omega}{\omega v_\perp}(v_\parallel\frac{\partial f_s}{\partial v_\perp} - v_\perp\frac{\partial f_s}{\partial v_\parallel})] \\
D^{(0)} &= 4(An^4 - Bn^2 + C),
\end{aligned}$$

where $A = S\sin^2\theta + P\cos^2\theta$, $B = RL\sin^2\theta + PS(1+\cos^2\theta)$ and $C = PRL$. $f_S(v_\perp, v_\parallel)$ is the phase space density in velocity space of species s and can be obtained from the particle flux J_s measured by the spacecraft instrument. $J_s(E_s, \alpha)$ is in energy (E_s) pitch angle (α) space and can be converted to the phase space density $f_s(E_s, \alpha)$ though the relation $f_s = J_s/(E_s \times 10^{-3}) \times H_{fac}$, where the units of f_s, J_s and E_s are s^3m^{-6}, $s^{-1}cm^{-2}keV^{-1}sr^{-1}$ and keV respectively. The H_{fac} is the conversion factor, which equals 5.449×10^{-19} for protons and 1.6163×10^{-25} for electrons. Consequently we can get the $f_s(v_\perp, v_\parallel)$ from $f_s(E_s, \alpha)$ through $m_s(v_\perp^2 + v_\parallel^2) = 2E_s$ and $v_\perp/v_\parallel = \tan\alpha$.

APPENDIX D

DERIVATIONS OF SCB MODEL

The coordinates of the model are:

$\rho \to \psi, \quad \zeta \to \phi \quad$ (azimuthal), $\quad \theta \to s \quad$ (length along field line)

$\psi = \frac{-B_d \cdot {R_e}^2}{L}, \quad L_{\text{in}}$ and $L_{\text{out}} \to \psi_{\text{in}}$ and ψ_{out}

$\psi = \psi(\rho, \zeta, \theta), \alpha = \alpha(\zeta)$

$\rho \in [0, 1], \quad \rho = \frac{\psi - \psi_{\text{in}}}{\psi_{\text{out}} - \psi_{\text{in}}}, \quad \zeta \in [0, 2\pi], \theta \in [0, \pi], \quad \theta = \frac{\pi \text{s}}{s_0} + C_\theta \sin\left(\frac{2\pi \text{s}}{s_0}\right)$

s_0 : length of field line, $\quad C_\theta$: coefficient to adjust the density of grids

Initial and Boundary set: Dipole field

For m girds for θ and n grids for ρ.Get the $x(m, n)$ and $z(m, n)$ for each grid.

Coordinate relations:

$$\mathcal{J} = \frac{\partial(X,Y,Z)}{\partial(\rho,\zeta,\theta)} = \begin{vmatrix} \frac{\partial X}{\partial \rho} & \frac{\partial X}{\partial \zeta} & \frac{\partial X}{\partial \theta} \\ \frac{\partial Y}{\partial \rho} & \frac{\partial Y}{\partial \zeta} & \frac{\partial Y}{\partial \theta} \\ \frac{\partial Z}{\partial \rho} & \frac{\partial Z}{\partial \zeta} & \frac{\partial Z}{\partial \theta} \end{vmatrix}$$

$$J = \mathcal{J}^{-1} = \nabla\rho \cdot (\nabla\zeta \times \nabla\theta) = \nabla\zeta \cdot (\nabla\theta \times \nabla\rho) = \nabla\theta \cdot (\nabla\rho \times \nabla\zeta)$$

$$\nabla \cdot \vec{A} = \frac{1}{\mathcal{J}} \left[\frac{\partial}{\partial \rho} \left(\mathcal{J} \mathrm{A}^\rho \right) + \frac{\partial}{\partial \zeta} \left(\mathcal{J} \mathrm{A}^\zeta \right) + \frac{\partial}{\partial \theta} \left(\mathcal{J} \mathrm{A}^\theta \right) \right]$$

$$\vec{e}_\rho = \frac{\partial \vec{r}}{\partial \rho}, \vec{e}^\rho = \nabla\rho, e_i \cdot e^j = \delta^j{}_i, \vec{A} = A^\rho \vec{e}_\rho + A^\zeta \vec{e}_\zeta + A^\theta \vec{e}_\theta = A_\rho \vec{e}^\rho + A_\zeta \vec{e}^\zeta + A_\theta \vec{e}^\theta$$

$$A^i = \vec{A} \cdot \vec{e}^i, A_j = \vec{A} \cdot \vec{e}_j$$

$$\vec{e}^i = \nabla u^i = \frac{\vec{e}_j \times \vec{e}_k}{\vec{e}_j \cdot \left(\vec{e}_j \times \vec{e}_k \right)}, \vec{e}_i = \frac{\nabla u^j \times \nabla u^k}{\nabla u^i \cdot \nabla u^j \times \nabla u^k}$$

$\vec{B}$ is along θ, so $\vec{B} = B^\theta \vec{e}_\theta = B\vec{b}, \quad \vec{B} = \nabla\psi \times \nabla\alpha$

$$\vec{B} = A_\rho \nabla\rho + A_\zeta \nabla\zeta + A_\theta \nabla\theta$$

$$\mathcal{J} = \frac{1}{\nabla\theta \cdot \nabla\rho \times \nabla\zeta} = \frac{(\mathrm{d}\psi/\mathrm{d}\rho)(\mathrm{d}\alpha/\mathrm{d}\zeta)}{B}$$

$$\vec{B} = \mathcal{J} \left(\vec{B} \cdot \nabla\zeta \times \nabla\theta \right) \nabla\rho + \mathcal{J} \left(\vec{B} \cdot \nabla\theta \times \nabla\rho \right) \nabla\zeta + \mathcal{J} \left(\vec{B} \cdot \nabla\rho \times \nabla\zeta \right) \nabla\theta$$

$$= \frac{(\mathrm{d}\psi/\mathrm{d}\rho)(\mathrm{d}\alpha/\mathrm{d}\zeta)}{B} \left(\vec{B} \cdot \nabla\zeta \times \nabla\theta \right) \nabla\rho +$$

$$\frac{(\mathrm{d}\psi/\mathrm{d}\rho)(\mathrm{d}\alpha/\mathrm{d}\zeta)}{B} \left(\vec{B} \cdot \nabla\theta \times \nabla\rho \right) \nabla\zeta +$$

$$\frac{(\mathrm{d}\psi/\mathrm{d}\rho)(\mathrm{d}\alpha/\mathrm{d}\zeta)}{B} \left(\vec{B} \cdot \nabla\rho \times \nabla\zeta \right) \nabla\theta$$

Basic equations:

$\vec{J} \times \vec{B} = \nabla P (*)$

$\vec{B} = \nabla\psi \times \nabla\alpha$

Dotting $\vec{B} \times \nabla\psi$ and $\vec{B} \times \nabla\alpha$ to both sides of Equation $*$ and using $\left(\vec{a} \times \vec{b}\right) \cdot \left(\vec{c} \times \vec{d}\right) = (\vec{a} \cdot \vec{c}) \left(\vec{b} \cdot \vec{d}\right) - \left(\vec{a} \cdot \vec{d}\right) \left(\vec{b} \cdot \vec{c}\right)$,

we have

$$\left(\vec{J} \cdot \vec{B}\right) \left(\vec{B} \cdot \nabla\psi\right) - \left(\vec{J} \cdot \nabla\psi\right) B^2 = \left(\frac{\partial P}{\partial \psi}\nabla\psi + \frac{\partial P}{\partial \alpha}\nabla\alpha\right) \cdot \left(\vec{B} \times \nabla\psi\right)$$
$$\left(\vec{J} \cdot \vec{B}\right) \left(\vec{B} \cdot \nabla\alpha\right) - \left(\vec{J} \cdot \nabla\alpha\right) B^2 = \left(\frac{\partial P}{\partial \psi}\nabla\psi + \frac{\partial P}{\partial \alpha}\nabla\alpha\right) \cdot \left(\vec{B} \times \nabla\alpha\right)$$

So,

$$\vec{J} \cdot \nabla\psi = -\frac{1}{B^2}\frac{\partial P}{\partial \alpha}\nabla\alpha \cdot \vec{B} \times \nabla\psi \ = -\frac{\partial P}{\partial \alpha}$$
$$\vec{J} \cdot \nabla\alpha = -\frac{1}{B^2}\frac{\partial P}{\partial \psi}\nabla\psi \cdot \vec{B} \times \nabla\alpha \ = \ \frac{\partial P}{\partial \psi}$$

Because

$$\vec{J} = \frac{1}{\mu_0}\nabla \times \vec{B} \text{and} \nabla \cdot \left(\vec{a} \times \vec{b}\right) = \vec{b} \cdot (\nabla \times \vec{a}) - \vec{a} \cdot \left(\nabla \times \vec{b}\right)$$

so

$$\vec{J} \cdot \nabla\psi = \frac{1}{\mu_0}\nabla \cdot \left(\vec{B} \times \nabla\psi\right) \text{ and } \vec{J} \cdot \nabla\alpha = \frac{1}{\mu_0}\nabla \cdot \left(\vec{B} \times \nabla\alpha\right)$$

Then,

$-\frac{\partial P}{\partial \alpha} = \frac{1}{\mu_0}\nabla \cdot (\nabla\psi \times \nabla\alpha \times \nabla\psi) = \frac{1}{\mu_0}\nabla \cdot \left[(\nabla\psi)^2\nabla\alpha - (\nabla\alpha \cdot \nabla\psi)\nabla\psi\right]$, (because $\vec{a} \times \vec{b} \times \vec{c} = (\vec{c} \cdot \vec{a})\,\vec{b} - \left(\vec{c} \cdot \vec{b}\right)\vec{a}$)

$$\frac{\partial P}{\partial \psi} = \frac{1}{\mu_0}\nabla \cdot \left[(\nabla\alpha \cdot \nabla\psi)\nabla\alpha - (\nabla\alpha)^2\nabla\psi\right]$$

Let

$$\vec{A} = (\nabla\alpha \cdot \nabla\psi)\nabla\alpha - (\nabla\alpha)^2\nabla\psi \text{then} \nabla \cdot \vec{A} = \mu_0\frac{\partial P}{\partial \psi}$$

$$A^\rho = \vec{A} \cdot \nabla\rho = (\nabla\psi \cdot \nabla\alpha)(\nabla\alpha \cdot \nabla\rho) - (\nabla\alpha)^2\nabla\psi \cdot \nabla\rho$$
$$= \left[\frac{\partial \psi}{\partial \rho}(\nabla\rho \cdot \nabla\zeta) + \frac{\partial \psi}{\partial \zeta}(\nabla\zeta)^2 + \frac{\partial \psi}{\partial \theta}(\nabla\theta \cdot \nabla\zeta)\right](\nabla\zeta \cdot \nabla\rho)\left(\frac{\mathrm{d}\alpha}{\mathrm{d}\zeta}\right)^2 -$$
$$\left[\frac{\partial \psi}{\partial \rho}(\nabla\rho)^2 + \frac{\partial \psi}{\partial \zeta}(\nabla\zeta \cdot \nabla\rho) + \frac{\partial \psi}{\partial \theta}(\nabla\theta \cdot \nabla\rho)\right](\nabla\zeta)^2\left(\frac{\mathrm{d}\alpha}{\mathrm{d}\zeta}\right)^2$$
$$= \left(\frac{\mathrm{d}\alpha}{\mathrm{d}\zeta}\right)^2\left\{\frac{\partial \psi}{\partial \rho}\left[(\nabla\rho \cdot \nabla\zeta)^2 - (\nabla\rho)^2(\nabla\zeta)^2\right] + \frac{\partial \psi}{\partial \theta}\left[(\nabla\zeta \cdot \nabla\theta)(\nabla\rho \cdot \nabla\zeta) - (\nabla\rho \cdot \nabla\theta)(\nabla\zeta)^2\right]\right\}$$

$A^\zeta = 0$

$A^\theta = \left(\frac{\mathrm{d}\alpha}{\mathrm{d}\zeta}\right)^2 \left\{\frac{\partial\psi}{\partial\rho}\left[(\nabla\rho\cdot\nabla\zeta)(\nabla\zeta\cdot\nabla\theta) - (\nabla\rho\cdot\nabla\theta)(\nabla\zeta)^2\right] + \frac{\partial\psi}{\partial\theta}\left[(\nabla\zeta\cdot\nabla\theta)^2 - (\nabla\zeta)^2(\nabla\theta)^2\right]\right\}$

Using $\nabla\cdot\vec{A} = \frac{1}{\mathcal{J}}\left[\frac{\partial}{\partial\rho}\left(\mathcal{J}\mathrm{A}^\rho\right) + \frac{\partial}{\partial\zeta}\left(\mathcal{J}\mathrm{A}^\zeta\right) + \frac{\partial}{\partial\theta}\left(\mathcal{J}\mathrm{A}^\theta\right)\right]$,

we have

$\nabla\cdot\vec{A} =$

$\left(\frac{\mathrm{d}\alpha}{\mathrm{d}\zeta}\right)^2 \frac{1}{\mathcal{J}}\left\{\frac{\partial}{\partial\rho}\mathcal{J}\left\{\frac{\partial\psi}{\partial\rho}\left[(\nabla\rho\cdot\nabla\zeta)^2 - (\nabla\rho)^2(\nabla\zeta)^2\right] + \frac{\partial\psi}{\partial\theta}\left[(\nabla\zeta\cdot\nabla\theta)(\nabla\rho\cdot\nabla\zeta) - (\nabla\rho\cdot\nabla\theta)(\nabla\zeta)^2\right]\right\} + \right.$
$\left.\frac{\partial}{\partial\rho}\mathcal{J}\left\{\frac{\partial\psi}{\partial\rho}\left[(\nabla\rho\cdot\nabla\zeta)(\nabla\zeta\cdot\nabla\theta) - (\nabla\rho\cdot\nabla\theta)(\nabla\zeta)^2\right] + \frac{\partial\psi}{\partial\theta}\left[(\nabla\zeta\cdot\nabla\theta)^2 - (\nabla\zeta)^2(\nabla\theta)^2\right]\right\}\right\}$

Let

$\mathcal{A} = (\nabla\zeta\cdot\nabla\theta)^2 - (\nabla\zeta)^2(\nabla\theta)^2, \mathcal{C} = (\nabla\rho\cdot\nabla\zeta)^2 - (\nabla\rho)^2(\nabla\zeta)^2,$

$\mathcal{B} = (\nabla\zeta\cdot\nabla\theta)(\nabla\rho\cdot\nabla\zeta) - (\nabla\rho\cdot\nabla\theta)(\nabla\zeta)^2$

then

$\frac{\nabla\cdot\vec{A}}{\left(\frac{\mathrm{d}\alpha}{\mathrm{d}\zeta}\right)^2} = \frac{1}{\mathcal{J}}\frac{\partial}{\partial\rho}\left(\mathcal{C}\frac{\partial\psi}{\partial\rho} + \mathcal{B}\frac{\partial\psi}{\partial\theta}\right) + \frac{1}{\mathcal{J}}\frac{\partial}{\partial\theta}\left(\mathcal{B}\frac{\partial\psi}{\partial\rho} + \mathcal{A}\frac{\partial\psi}{\partial\theta}\right)$

Finally,

$\frac{\partial}{\partial\theta}\left(\mathcal{A}\frac{\partial\psi}{\partial\theta} + \mathcal{B}\frac{\partial\psi}{\partial\rho}\right) + \frac{\partial}{\partial\rho}\left(\mathcal{B}\frac{\partial\psi}{\partial\theta} + \mathcal{C}\frac{\partial\psi}{\partial\rho}\right) = \mathcal{J}\frac{\nabla\cdot\vec{A}}{\left(\frac{\mathrm{d}\alpha}{\mathrm{d}\zeta}\right)^2} = \frac{\mu_0\mathcal{J}}{\left(\frac{\mathrm{d}\alpha}{\mathrm{d}\zeta}\right)^2}\frac{\partial P}{\partial\psi}$

Equation coefficients:

$1 = (\nabla X\times\nabla Y)\cdot\nabla Z = [$

$\left(\frac{\partial X}{\partial\rho}\nabla\rho + \frac{\partial X}{\partial\zeta}\nabla\zeta + \frac{\partial X}{\partial\theta}\nabla\theta\right)\times\left(\frac{\partial Y}{\partial\rho}\nabla\rho + \frac{\partial Y}{\partial\zeta}\nabla\zeta + \frac{\partial Y}{\partial\theta}\nabla\theta\right)\Big]\cdot\left(\frac{\partial Z}{\partial\rho}\nabla\rho + \frac{\partial Z}{\partial\zeta}\nabla\zeta + \frac{\partial Z}{\partial\theta}\nabla\theta\right)$

$= \left[\frac{\partial X}{\partial\rho}\left(\frac{\partial Y}{\partial\zeta}\frac{\partial Z}{\partial\theta} - \frac{\partial Y}{\partial\theta}\frac{\partial Z}{\partial\zeta}\right) + \frac{\partial X}{\partial\zeta}\left(\frac{\partial Y}{\partial\theta}\frac{\partial Z}{\partial\rho} - \frac{\partial Y}{\partial\rho}\frac{\partial Z}{\partial\theta}\right) + \frac{\partial X}{\partial\theta}\left(\frac{\partial Y}{\partial\rho}\frac{\partial Z}{\partial\zeta} - \frac{\partial Y}{\partial\zeta}\frac{\partial Z}{\partial\rho}\right)\right]\cdot[\nabla\theta\cdot(\nabla\rho\times\nabla\zeta)]$

$\mathcal{J} = \frac{1}{[\nabla\theta\cdot(\nabla\rho\times\nabla\zeta)]} = \frac{\partial X}{\partial\rho}\left(\frac{\partial Y}{\partial\zeta}\frac{\partial Z}{\partial\theta} - \frac{\partial Y}{\partial\theta}\frac{\partial Z}{\partial\zeta}\right) + \frac{\partial X}{\partial\zeta}\left(\frac{\partial Y}{\partial\theta}\frac{\partial Z}{\partial\rho} - \frac{\partial Y}{\partial\rho}\frac{\partial Z}{\partial\theta}\right) + \frac{\partial X}{\partial\theta}\left(\frac{\partial Y}{\partial\rho}\frac{\partial Z}{\partial\zeta} - \frac{\partial Y}{\partial\zeta}\frac{\partial Z}{\partial\rho}\right)$

$\nabla\rho = \frac{\partial\rho}{\partial X}\nabla X + \frac{\partial\rho}{\partial Y}\nabla Y + \frac{\partial\rho}{\partial Z}\nabla Z = \frac{\partial(\rho,Y,Z)}{\partial(X,Y,Z)}\nabla X + \frac{\partial(X,\rho,Z)}{\partial(X,Y,Z)}\nabla Y + \frac{\partial(X,Y,\rho)}{\partial(X,Y,Z)}\nabla Z$

$= \frac{\partial(\rho,Y,Z)}{\partial(\rho,\zeta,\theta)}\frac{\partial(\rho,\zeta,\theta)}{\partial(X,Y,Z)}\nabla X + \frac{\partial(X,\rho,Z)}{\partial(\theta,\rho,\zeta)}\frac{\partial(\theta,\rho,\zeta)}{\partial(X,Y,Z)}\nabla Y + \frac{\partial(X,Y,\rho)}{\partial(\zeta,\theta,\rho)}\frac{\partial(\zeta,\theta,\rho)}{\partial(X,Y,Z)}\nabla Z$

$\frac{\partial(\rho,\zeta,\theta)}{\partial(X,Y,Z)}, \frac{\partial(\theta,\rho,\zeta)}{\partial(X,Y,Z)}, \frac{\partial(\zeta,\theta,\rho)}{\partial(X,Y,Z)}$ are all equal to $\mathcal{J}^{-1}$

and

$\frac{\partial(\rho,Y,Z)}{\partial(\rho,\zeta,\theta)} = \frac{\partial Y}{\partial\zeta}\frac{\partial Z}{\partial\theta} - \frac{\partial Y}{\partial\theta}\frac{\partial Z}{\partial\zeta}, \frac{\partial(X,\rho,Z)}{\partial(\theta,\rho,\zeta)} = \frac{\partial X}{\partial\theta}\frac{\partial Z}{\partial\zeta} - \frac{\partial X}{\partial\zeta}\frac{\partial Z}{\partial\theta}, \frac{\partial(X,Y,\rho)}{\partial(\zeta,\theta,\rho)} = \frac{\partial X}{\partial\zeta}\frac{\partial Y}{\partial\theta} - \frac{\partial X}{\partial\theta}\frac{\partial Y}{\partial\zeta}$

So,

$\nabla\rho = \mathcal{J}^{-1}\left[\left(\frac{\partial Y}{\partial\zeta}\frac{\partial Z}{\partial\theta} - \frac{\partial Y}{\partial\theta}\frac{\partial Z}{\partial\zeta}\right)\nabla X + \left(\frac{\partial X}{\partial\theta}\frac{\partial Z}{\partial\zeta} - \frac{\partial X}{\partial\zeta}\frac{\partial Z}{\partial\theta}\right)\nabla Y + \left(\frac{\partial X}{\partial\zeta}\frac{\partial Y}{\partial\theta} - \frac{\partial X}{\partial\theta}\frac{\partial Y}{\partial\zeta}\right)\nabla Z\right]$

The same way,

$$\nabla\zeta = \mathcal{J}^{-1}\left[\left(\frac{\partial Y}{\partial\theta}\frac{\partial Z}{\partial\rho} - \frac{\partial Y}{\partial\rho}\frac{\partial Z}{\partial\theta}\right)\nabla X + \left(\frac{\partial X}{\partial\rho}\frac{\partial Z}{\partial\theta} - \frac{\partial X}{\partial\theta}\frac{\partial Z}{\partial\rho}\right)\nabla Y + \left(\frac{\partial X}{\partial\theta}\frac{\partial Y}{\partial\rho} - \frac{\partial X}{\partial\rho}\frac{\partial Y}{\partial\theta}\right)\nabla Z\right]$$

$$\nabla\theta = \mathcal{J}^{-1}\left[\left(\frac{\partial Y}{\partial\rho}\frac{\partial Z}{\partial\zeta} - \frac{\partial Y}{\partial\zeta}\frac{\partial Z}{\partial\rho}\right)\nabla X + \left(\frac{\partial X}{\partial\zeta}\frac{\partial Z}{\partial\rho} - \frac{\partial X}{\partial\rho}\frac{\partial Z}{\partial\zeta}\right)\nabla Y + \left(\frac{\partial X}{\partial\rho}\frac{\partial Y}{\partial\zeta} - \frac{\partial X}{\partial\zeta}\frac{\partial Y}{\partial\rho}\right)\nabla Z\right]$$

then we can get $\mathcal{A}, \mathcal{B}$ and $\mathcal{C}$.

Discretization:

We have got

$$\mathcal{A}\frac{\partial^2\psi}{\partial\theta^2} + 2\mathcal{B}\frac{\partial^2\psi}{\partial\theta\partial\rho} + \mathcal{C}\frac{\partial^2\psi}{\partial\rho^2} + \left(\frac{\partial\mathcal{A}}{\partial\theta} + \frac{\partial\mathcal{B}}{\partial\rho}\right)\frac{\partial\psi}{\partial\theta} + \left(\frac{\partial\mathcal{B}}{\partial\theta} + \frac{\partial\mathcal{C}}{\partial\rho}\right)\frac{\partial\psi}{\partial\rho} = \frac{\mu_0\mathcal{J}}{\left(\frac{\mathrm{d}\alpha}{\mathrm{d}\zeta}\right)^2}\frac{\partial P}{\partial\psi}$$

For $\psi_{i,j}$

$$\frac{\partial^2\psi}{\partial\theta^2} = \frac{\psi_{i+1,j}+\psi_{i-1,j}-2\psi_{i,j}}{(\Delta\theta)^2}$$

$$\frac{\partial^2\psi}{\partial\rho^2} = \frac{\psi_{i,j+1}+\psi_{i,j-1}-2\psi_{i,j}}{(\Delta\rho)^2}$$

$$\frac{\partial^2\psi}{\partial\rho\partial\theta} = \frac{\psi_{i+1,j+1}-\psi_{i-1,j+1}-\psi_{i+1,j-1}+\psi_{i-1,j-1}}{4\Delta\rho\Delta\theta}$$

$$\frac{\partial\psi}{\partial\theta} = \frac{\psi_{i+1,j}-\psi_{i-1,j}}{2\Delta\theta}$$

$$\frac{\partial\psi}{\partial\rho} = \frac{\psi_{i,j+1}-\psi_{i,j-1}}{2\Delta\rho}$$

Finally,

$$a_{\mathrm{ij}}\psi_{i,j} + b_{\mathrm{ij}}\psi_{i-1,j-1} + c_{\mathrm{ij}}\psi_{i+1,j-1} + d_{\mathrm{ij}}\psi_{i-1,j} +$$

$$e_{\mathrm{ij}}\psi_{i-1,j+1} + f_{\mathrm{ij}}\psi_{i+1,j} + g_{\mathrm{ij}}\psi_{i+1,j+1} + h_{\mathrm{ij}}\psi_{i,j-1} + k_{\mathrm{ij}}\psi_{i,j+1} = l_{\mathrm{ij}}$$

$$a_{\mathrm{ij}} = -2\left[\frac{\mathcal{A}}{(\Delta\theta)^2} + \frac{\mathcal{C}}{(\Delta\rho)^2}\right]_{\mathrm{ij}}$$

$$b_{\mathrm{ij}} = \frac{\mathcal{B}_{\mathrm{ij}}}{2\Delta\theta\Delta\rho}$$

$$c_{\mathrm{ij}} = \frac{\mathcal{B}_{\mathrm{ij}}}{2\Delta\theta\Delta\rho}$$

$$d_{\mathrm{ij}} = \frac{\mathcal{A}_{\mathrm{ij}}}{(\Delta\theta)^2} - \frac{\left(\frac{\partial\mathcal{A}}{\partial\theta}+\frac{\partial\mathcal{B}}{\partial\rho}\right)_{\mathrm{ij}}}{2\Delta\theta}$$

$$e_{\mathrm{ij}} = c_{\mathrm{ij}}$$

$$f_{\mathrm{ij}} = \frac{\mathcal{A}_{\mathrm{ij}}}{(\Delta\theta)^2} + \frac{\left(\frac{\partial\mathcal{A}}{\partial\theta}+\frac{\partial\mathcal{B}}{\partial\rho}\right)_{\mathrm{ij}}}{2\Delta\theta}$$

$$g_{\mathrm{ij}} = c_{\mathrm{ij}}$$

$$h_{\mathrm{ij}} = \frac{\mathcal{C}_{\mathrm{ij}}}{(\Delta\rho)^2} - \frac{\left(\frac{\partial\mathcal{B}}{\partial\theta}+\frac{\partial\mathcal{C}}{\partial\rho}\right)_{\mathrm{ij}}}{2\Delta\rho}$$

$$k_{\mathrm{ij}} = \frac{\mathcal{C}_{\mathrm{ij}}}{(\Delta\rho)^2} + \frac{\left(\frac{\partial\mathcal{B}}{\partial\theta}+\frac{\partial\mathcal{C}}{\partial\rho}\right)_{\mathrm{ij}}}{2\Delta\rho}$$

$$l_{\mathrm{ij}} = \mu_0\left(\frac{\mathrm{d}\alpha}{\mathrm{d}\zeta}\right)^{-2}\mathcal{J}_{\mathrm{ij}}\left(\frac{\partial P}{\partial\psi}\right)_{\mathrm{ij}}$$

For anisotropic pressure

$$\overrightarrow{\overrightarrow{P}} = \begin{pmatrix} P_\perp & 0 & 0 \\ 0 & P_\perp & 0 \\ 0 & 0 & P_\parallel \end{pmatrix}$$

$$\vec{J} \times \vec{B} = \nabla \cdot \overrightarrow{\overrightarrow{P}} = \nabla P_\perp - \nabla \cdot \left[\left(P_\perp - P_\parallel \right) \hat{b}\hat{b} \right]$$

$$\mu_0 \sigma \left(\vec{J} \times \vec{B} \right) = \nabla \mu_0 P_\perp - \left(\vec{B} \cdot \nabla \sigma \right) \vec{B} + (1-\sigma) \nabla \left(\frac{B^2}{2} \right),$$

$\sigma = 1 + \mu_0 \left(P_\perp - P_\parallel \right) / B^2$ (the derivation is shown in the Appendix below.)

Dot $\left(\vec{B} \times \nabla \psi \right)$ and $\left(\vec{B} \times \nabla \alpha \right)$, we have

$$\mu_0 \vec{J} \cdot \nabla \psi = \nabla \cdot \left[(\nabla \psi)^2 \nabla \alpha - (\nabla \alpha \cdot \nabla \psi) \nabla \psi \right] = -\frac{\vec{B} \times \nabla \psi}{\sigma \mathrm{B}^2} \cdot \left[\nabla \mu_0 P_\perp + (1-\sigma) \nabla \left(\frac{B^2}{2} \right) \right]$$

$$\mu_0 \vec{J} \cdot \nabla \alpha = \nabla \cdot \left[(\nabla \alpha \cdot \nabla \psi) \nabla \alpha - (\nabla \alpha)^2 \nabla \psi \right] = -\frac{\vec{B} \times \nabla \alpha}{\sigma \mathrm{B}^2} \cdot \left[\nabla \mu_0 P_\perp + (1-\sigma) \nabla \left(\frac{B^2}{2} \right) \right] = \nabla \cdot \vec{A}$$

$$P_\perp = \frac{P_{\perp e}}{[1 + A_e(R)(1-S)]^2}, P_\parallel = \frac{P_{\parallel e}}{1 + A_e(R)(1-S)}$$

$S = \frac{B_e}{B}, A_e(R) = P_{\perp e}/P_{\parallel e} - 1$ (equatorial anisotropy)

Appendix

$$\nabla \cdot \overrightarrow{\overrightarrow{P}} = \nabla P_\perp - \nabla \cdot \left[\left(P_\perp - P_\parallel \right) \hat{b}\hat{b} \right] =$$

$$\nabla P_\perp - \nabla \cdot \left[\frac{\left(P_\perp - P_\parallel \right) \vec{B}\vec{B}}{B^2} \right] = \nabla P_\perp - \nabla \frac{\left(P_\perp - P_\parallel \right)}{B^2} \cdot \vec{B}\vec{B} - \frac{\left(P_\perp - P_\parallel \right)}{B^2} \nabla \cdot \vec{B}\vec{B} = \vec{J} \times \vec{B}$$

$$\left(\nabla \cdot \vec{B}\vec{B} \right)_i = \partial_i \hat{e}_i \left(B_i B_j \right) \hat{e}_i \hat{e}_j = B_j \partial_i B_i \hat{e}_j + B_i \partial_i B_j \hat{e}_j = \left(\nabla \cdot \vec{B} \right) \vec{B} + B_i \partial_i B_j \hat{e}_j = 0 + B_j \partial_j B_i \hat{e}_i$$

$$\left[\vec{B} \times \left(\nabla \times \vec{B} \right) \right]_i =_{\mathrm{ijk}} B_j \left(\nabla \times \vec{B} \right)_k = \varepsilon_{\mathrm{ijk}} B_j \varepsilon_{\mathrm{kpq}} \partial_p B_q = \varepsilon_{\mathrm{kij}} \varepsilon_{\mathrm{kpq}} B_j \partial_p B_q$$

$$= \left(\delta_{\mathrm{ip}} \delta_{\mathrm{jq}} - \delta_{\mathrm{iq}} \delta_{\mathrm{jp}} \right) B_j \partial_p B_q = B_j \partial_i B_j - B_j \partial_j B_i$$

and

$$\left[\nabla \left(\frac{B^2}{2} \right) \right]_i = \partial_i \left(\frac{{B_j}^2}{2} \right) = B_j \partial_i B_j$$

So,

$$\left[\vec{B} \times \left(\nabla \times \vec{B} \right) \right]_i = \left[\nabla \left(\frac{B^2}{2} \right) \right]_i - \left(\nabla \cdot \vec{B}\vec{B} \right)_i$$

$$\nabla \cdot \vec{B}\vec{B} = \nabla \left(\frac{B^2}{2} \right) - \vec{B} \times \left(\nabla \times \vec{B} \right)$$

Then,

$$\nabla \cdot \overrightarrow{\overrightarrow{P}} - \vec{J} \times \vec{B}$$
$$= \nabla P_\perp - \left[\nabla \frac{\left(P_\perp - P_\parallel\right)}{B^2} \cdot \vec{B}\right] \vec{B} - \frac{\left(P_\perp - P_\parallel\right)}{B^2} \left[\nabla \left(\frac{B^2}{2}\right) - \vec{B} \times \left(\nabla \times \vec{B}\right)\right] - \frac{1}{\mu_0} \left(\nabla \times \vec{B}\right) \times \overrightarrow{B}$$
$$= \nabla P_\perp - \left[\nabla \frac{\left(P_\perp - P_\parallel\right)}{B^2} \cdot \vec{B}\right] \vec{B} - \frac{1}{\mu_0} \left(\nabla \times \vec{B}\right) \times \overrightarrow{B} \left[1 + \frac{\mu_0 \left(P_\perp - P_\parallel\right)}{B^2}\right] - \frac{\left(P_\perp - P_\parallel\right)}{B^2} \nabla \left(\frac{B^2}{2}\right)$$
$$= \nabla P_\perp - \left[\nabla \frac{\sigma}{\mu_0} \cdot \vec{B}\right] \vec{B} - \sigma \vec{J} \times \vec{B} - \frac{1-\sigma}{\mu_0} \nabla \left(\frac{B^2}{2}\right) = 0$$

Finally,

$$\mu_0 \sigma \left(\vec{J} \times \vec{B}\right) = \nabla \mu_0 P_\perp - \left(\vec{B} \cdot \nabla \sigma\right) \vec{B} + (1-\sigma) \nabla \left(\frac{B^2}{2}\right) = \sigma \left(\nabla \times \vec{B}\right) \times \overrightarrow{B}$$

APPENDIX E

ANALYTICAL SOLUTIONS FOR THE THREE APPROXIMATIONS

E.1 Uniform Magnetic Fields

Consider the presence of localized plasma pressure in an initially uniform magnetic field B_0. The analytic solution of magnetic pressure equilibrium for a uniform background magnetic field can be derived directly through the condition of uniform total pressure (that is, the sum of the magnetic pressure and the thermal pressure), $P_{B0} = P + P_B$, where P_{B0} is the magnetic pressure at the finite boundary (or the initial magnetic field pressure), P and P_B are the thermal pressure and magnetic pressure in equilibrium respectively. Thus $|\Delta B/B_0|$ can be written as $(B_0 - B)/B_0 = 1 - B/B_0 = 1 - \sqrt{P_B/P_{B0}} = 1 - \sqrt{P_B/(P + P_B)} = 1 - \sqrt{1/(\beta + 1)}$, where $\beta = P/P_B$. In equilibrium, a magnetic dip forms whenever there is localized pressure distribution. The critical β to form a dip is essentially zero.

E.2 Circular and Planar Magnetic Fields

An infinitely long straight line current can generate a circular and planar magnetic field surrounding the line current. The magnetic field strength B_0 decreases with r as:

$$B_0 = \frac{\mu_0 I}{2\pi r} \tag{E.1}$$

, where I is the current, r is the distance to the current, and μ_0 is the vacuum permeability.

Consider localized plasma pressure in such an initially circular and planar magnetic field. The localized pressure is introduced as $P = P_0 \exp\left[-(r - L_0)^2/(2\sigma_0^2)\right]$, with pressure peak P_0 at L_0 and half pressure peak width σ_0. In equilibrium, the force balance equation can be expressed as a 1D nonlinear ordinary differential equation for $B(r)$:

$$\frac{1}{r}\left(\frac{d}{dr}(rB)\right)B = -\mu_0 \frac{dP}{dr}. \tag{E.2}$$

The corresponding analytic solution is obtained as:

$$B^2(r) = -2\mu_0 P_0 \exp\left[\frac{-(r-L_0)^2}{(2\sigma_0^2)}\right] - \frac{4\sigma_0^2\mu_0 P_0 \exp\left[\frac{-(r-L_0)^2}{(2\sigma_0^2)}\right]}{r^2} + \frac{2L_0\sigma_0\mu_0 P_0\sqrt{2\pi}\mathrm{Erf}(\frac{r-L_0}{\sqrt{2}\sigma_0})}{r^2} + \frac{C_1}{r^2} \tag{E.3}$$

, where C_1 is a constant which controls the intensity of the background magnetic field. The term C_1/r^2 is the square of background magnetic field and the other terms are the perturbations caused by the thermal pressure. The pressure peak P_0 can be set as $\beta_0 P_{B0}(L_0)$, where $P_{B0}(L_0)$ is the background magnetic pressure at L_0 and equals to $C_1/2\mu_0 L_0^2$.

There are four terms on the right hand side, and the second and the third terms can be neglected approximately due to small value of σ_0/r and $r > 1$. The remaining two terms are the first term which is contributed from thermal pressure and the last term which corresponds to the background circular magnetic field.

The condition for the existence of a magnetic dip is that there exists a local minimum, that is, $\frac{dB}{dr} = 0$. Considering only the first and last terms in Equation (E.3), the condition yields:

$$\beta^* = \frac{2\sigma_0^2}{r_d(r_d - L_0)} = \frac{2\sigma_0^2}{(L_0 + \Delta L)\Delta L} \tag{E.4}$$

, where the r_d denotes the location of the magnetic dip, $\Delta L = r_d - L_0$ is the distance between the magnetic dip and the pressure peak, and $\beta^* = 2\mu_0 P_0 \exp\left[\frac{-(r_d-L_0)^2}{(2\sigma_0^2)}\right]/(C_1/r_d^2)$ is the ratio between thermal pressure and the initial magnetic pressure at the dip. The value of ΔL scales as σ_0. Considering $L_0 + \Delta L \approx L_0$ because $L_0 \gg \Delta L$, a simplified relation can be obtained as $\beta^* \sim \sigma_0/L_0$. In other words, the critical β for the dip formation in the background circular magnetic field tends to increase for larger σ_0 and smaller L_0.

E.3 Dipole Fields Ignoring the Change of Magnetic Field Curvature

Consider the presence of isotropic thermal pressure in the background dipole field, the field line strength and curvature change in equilibrium. The force balance equation can be rewritten as:

$$-\nabla_{\perp} P_B + 2P_B \hat{b} \cdot \nabla \hat{b} = \nabla P \tag{E.5}$$

, where $P_B = \frac{B^2}{2\mu_0}$ is the magnetic pressure, and $\hat{b}$ is the unit magnetic field vector. Near the equatorial plane, the curvature term $\hat{b} \cdot \nabla \hat{b}$ can be express as $-\frac{\hat{e_r}}{R_c}$ and the perpendicular gradient $\nabla_{\perp}$ equals to $\frac{\partial}{\partial r}\hat{e_r}$, where R_c is radius of the curvature, and $\hat{e_r}$ is the unit vector in the radial direction. For dipole field, $R_c = r/3$. When we assume that the curvature of the magnetic field line remains unchanged, the equilibrium equation at the equator becomes:

$$-\frac{\partial}{\partial r} P_B - \frac{6P_B}{r} = \frac{\partial}{\partial r} P \tag{E.6}$$

. For the case that $P = 0$, the solution of the equation is $P_B = \frac{B^2}{2\mu_0} = Cr^{-6}$, where C is a constant. Thus we have $B = B_0 r^{-3}$, where $B_0 = \sqrt{2\mu_0 C}$, and this is the solution of the Earth's dipole field.

For the case of a radially Gaussian pressure distribution in the equator, $P = P_0 \exp[-(r - L_0)^2/(2\sigma_0^2)]$, with pressure peak P_0 at L_0 and half pressure peak width σ_0, the analytical solution to Equation (E.6) is

$$\begin{aligned} P_B =& \frac{C_2}{r^6} - \frac{P_0}{r^6} \exp\left[\frac{-(r-L_0)^2}{2\sigma_0^2}\right]\{48\sigma_0^6 + r^6 + 6\sigma_0^4(4r^2 + 7r\sigma_0 + 9\sigma_0^2) + 6\sigma_0^2(r^4 + r^3\sigma_0 + r^2\sigma_0^2 \\ &+ r\sigma_0^3 + \sigma_0^4) - 3\sigma_0 \exp\left[\frac{(r-L_0)^2}{2\sigma_0^2}\right]\sqrt{2\pi} L_0 (15\sigma_0^4 + 10\sigma_0^2 L_0^2 + \sigma_0^4)\mathrm{Erf}\left(\frac{r-L_0}{\sqrt{2}\sigma_0}\right)\} \end{aligned} \tag{E.7}$$

, where C_2 is a constant that controls the intensity of the background magnetic pressure. The term C_2/r^6 is the background dipolar magnetic pressure and the other terms are the

contributions of the thermal pressure to the perturbation of magnetic pressure. The pressure peak P_0 can be set as $\beta_0 P_{B0}(L_0)$, where $P_{B0}(L_0) = C_2/L_0^6$ is the background magnetic pressure at L_0. The magnetic strength can be obtained by $B = \sqrt{2\mu_0 P_B}$.

APPENDIX F

SOUTH ATLANTIC ANOMALY

The South Atlantic Anomaly (SAA) is a near-Earth region with the weakest Earth's magnetic field relative to the idealized Earth's dipole field, which is located above the south Atlantic Ocean. The formation of SAA involves the inner radiation belts and the asymmetry between the Earth's rotation axis and the magnetic axis. The inner radiation belt is symmetrical about the Earth's magnetic axis but not the Earth's rotational axis. The angle between the two axes is about 11° and the intersection between the two axes is located not at the Earth's center, but about 450 to 500 km (280 to 310 mi) away north of the Earth's equator. Thus the inner radiation belt becomes closer to the Earth's surface and penetrates the Earth's ionosphere to about 200 km (120 mi) in altitude, which occurs near the south Atlantic region. The relation between the Earth's rotation axis and the magnetic axis as well as the radiation belts are shown in Figure F.1. The energetic electrons in the inner belts can decrease the magnetic field strength due to the diamagnetic effect and result in the anomaly of magnetic strength. Figure F.2 shows the global distribution of geomagnetic field strength and the outline of SAA.

The SAA is slowly drifting north and west at rates of 0.16 °/year and 0.36 °/year, respectively. Currently, it is most intense over a broad region centered on Sao Paulo, Brazil, including much of Paraguay, Uruguay, and northern Argentina. It also exhibits a seasonal variation: on average, the SAA is most intense in February and again in September-October. The SAA is of great significance to satellites and other spacecraft orbiting the Earth at altitudes of several hundred kilometers. These satellites travel through the SAA periodically and are exposed to several minutes of strong radiation caused by the trapped energetic particles in the inner radiation belt.

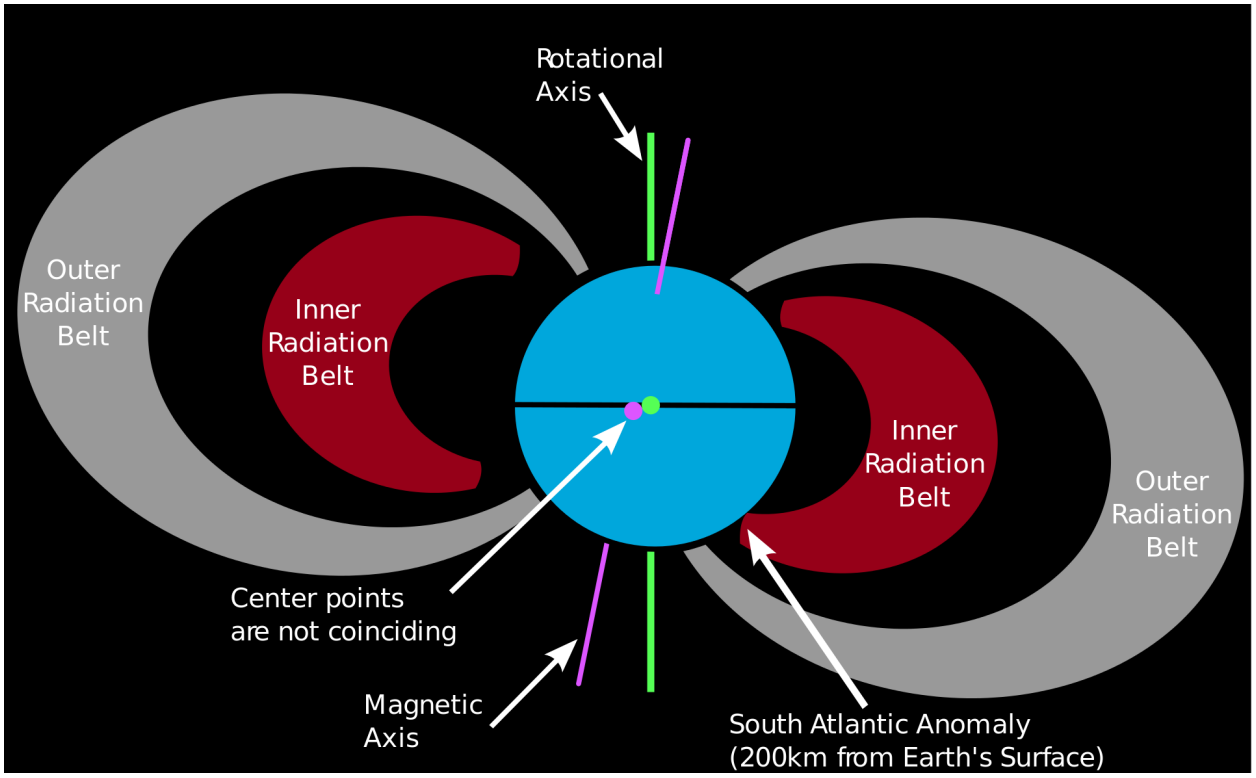

Figure F.1. A view of the Earth's rotation axis, magnetic axis and the Van Allen radiation belts [Wikipedia, https://en.wikipedia.org/wiki/South_Atlantic_Anomaly].

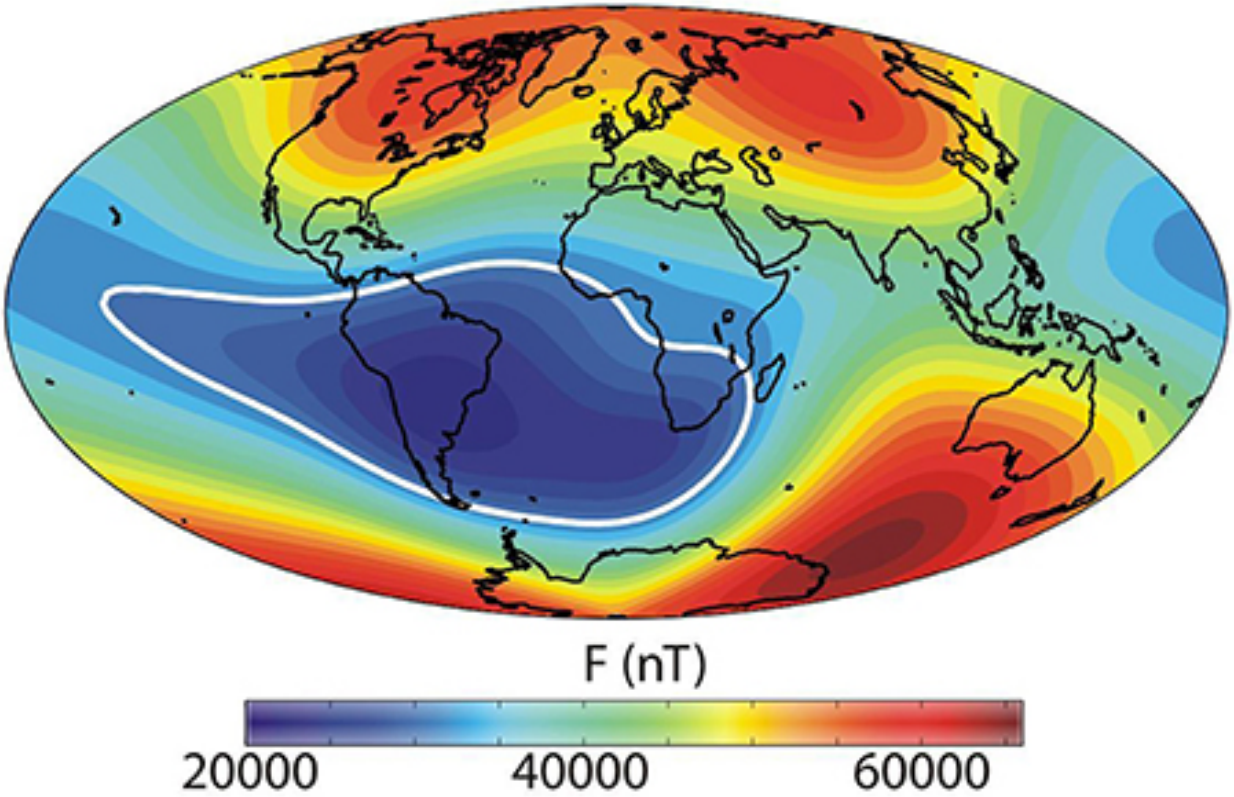

Figure F.2. The intensity geomagnetic field map at 2015 that indicates the SAA region [Pavón-Carrasco and De Santis, 2016].

REFERENCES

Abdu, M. A., I. S. Batista, A. J. Carrasco, and C. G. M. Brum (2005). South Atlantic magnetic anomaly ionization: A review and a new focus on electrodynamic effects in the equatorial ionosphere. *Journal of Atmospheric and Solar-Terrestrial Physics 67*(17), 1643–1657.

Abdu, M. A., I. S. Batista, L. R. Piazza, and O. Massambani (1981). Magnetic storm associated enhanced particle precipitation in the South Atlantic Anomaly: Evidence from VLF phase measurements. *Journal of Geophysical Research: Space Physics 86*(A9), 7533–7542.

Abel, B. and R. M. Thorne (1998a). Electron scattering loss in earth's inner magnetosphere: 1. dominant physical processes. *Journal of Geophysical Research: Space Physics 103*(A2), 2385–2396.

Abel, B. and R. M. Thorne (1998b). Electron scattering loss in earth's inner magnetosphere: 2. sensitivity to model parameters. *Journal of Geophysical Research: Space Physics 103*(A2), 2397–2407.

Agapitov, O., A. Artemyev, V. Krasnoselskikh, Y. V. Khotyaintsev, D. Mourenas, H. Breuillard, M. Balikhin, and G. Rolland (2013). Statistics of whistler mode waves in the outer radiation belt: Cluster staff-sa measurements. *Journal of Geophysical Research: Space Physics 118*(6), 3407–3420.

Akasofu, S.-I. (1964). The development of the auroral substorm. *Planetary and Space Science 12*, 273–282.

Aryan, H., K. Yearby, M. Balikhin, O. Agapitov, V. Krasnoselskikh, and R. Boynton (2014). Statistical study of chorus wave distributions in the inner magnetosphere using ae and solar wind parameters. *Journal of Geophysical Research: Space Physics 119*(8), 6131–6144.

Auster, H. U., K. H. Glassmeier, W. Magnes, O. Aydogar, W. Baumjohann, D. Constantinescu, D. Fischer, K. H. Fornacon, E. Georgescu, P. Harvey, O. Hillenmaier, R. Kroth, M. Ludlam, Y. Narita, R. Nakamura, K. Okrafka, F. Plaschke, I. Richter, H. Schwarzl, B. Stoll, A. Valavanoglou, and M. Wiedemann (2008). The themis fluxgate magnetometer. *Space Science Reviews 141*(1), 235–264.

Baker, D. and Others (2013). The Relativistic Electron-Proton Telescope (REPT) Instrument on Board the Radiation Belt Storm Probes (RBSP) Spacecraft: Characterization of Earth's Radiation Belt High-Energy Particle Populations. *Space Science Reviews 179*, 337–381.

Benbrook, J. R., E. A. Bering III, H. Leverenz, J. L. Roeder, and W. R. Sheldon (1983). Quiet-time electron precipitation at L = 4 in the South Atlantic Anomaly. *Journal of Geophysical Research: Space Physics 88*(A1), 189–199.

Berthelier, J. J., M. Godefroy, F. Leblanc, M. Malingre, M. Menvielle, D. Lagoutte, J. Y. Brochot, F. Colin, F. Elie, C. Legendre, P. Zamora, D. Benoist, Y. Chapuis, J. Artru, and R. Pfaff (2006). ICE, the electric field experiment on DEMETER. *Planetary and Space Science 54*(5), 456–471.

Bilitza, D. (2018). IRI the International Standard for the Ionosphere. *Advances in Radio Science 16*, 1–11.

Blake, J. and Others (2013). The Magnetic Electron Ion Spectrometer (MagEIS) Instruments Aboard the Radiation Belt Storm Probes (RBSP) Spacecraft. *Space Science Reviews 179*, 383–421.

Bonnell, J. W., F. S. Mozer, G. T. Delory, A. J. Hull, R. E. Ergun, C. M. Cully, V. Angelopoulos, and P. R. Harvey (2008). The electric field instrument (efi) for themis. *Space Science Reviews 141*(1), 303–341.

Bortnik, J., L. Chen, W. Li, R. M. Thorne, and R. B. Horne (2011). Modeling the evolution of chorus waves into plasmaspheric hiss. *Journal of Geophysical Research: Space Physics 116*(A8).

Bortnik, J., W. Li, R. M. Thorne, V. Angelopoulos, C. Cully, J. Bonnell, O. Le Contel, and A. Roux (2009). An Observation Linking the Origin of Plasmaspheric Hiss to Discrete Chorus Emissions. *Science 324*(5928), 775–778.

Bortnik, J., R. M Thorne, and N. Meredith (2008). The unexpected origin of plasmaspheric hiss from discrete chorus waves. *Nature 452*, 62–66.

Bortnik, J. and R. Thorne (2007b). The dual role of elf/vlf chorus waves in the acceleration and precipitation of radiation belt electrons. *Journal of Atmospheric and Solar-Terrestrial Physics 69*(3), 378 – 386. Global Aspects of Magnetosphere-Ionosphere Coupling.

Bortnik, J., R. M. Thorne, and N. P. Meredith (2007a). Modeling the propagation characteristics of chorus using crres suprathermal electron fluxes. *Journal of Geophysical Research: Space Physics 112*(A8).

Breneman, A. and Others (2015). Global-scale coherence modulation of radiation-belt electron loss from plasmaspheric hiss. *Nature 523*, 193–195.

Burtis, W. and R. Helliwell (1969). Banded chorus: A new type of VLF radiation observed in the magnetosphere by OGO 1 and OGO 3. *J. Geophys. Res. 74*, 3002.

Burtis, W. and R. Helliwell (1976). Magnetospheric chorus - Occurrence patterns and normalized frequency. *Planetary and Space Science 24*, 1007–1024.

C. Brandt, P., D. G. Mitchell, E. C. Roelof, S. M. Krimigis, C. P. Paranicas, B. H. Mauk, J. Saur, and R. DeMajistre (2005). Ena imaging: Seeing the invisible. *Johns Hopkins APL Technical Digest (Applied Physics Laboratory) 26*, 143–154.

Chan, A., M. Xia, and L. Chen (1994). Anisotropic Alfven-ballooning modes in Earth's magnetosphere. *J. Geophys. Res. 99*, 17.

Chan, K.-W. and R. E. Holzer (1976). ELF hiss associated with plasma density enhancements in the outer magnetosphere. *Journal of Geophysical Research 81*(13), 2267–2274.

Chen, L. and A. Hasegawa (1991). Kinetic theory of geomagnetic pulsations. I - Internal excitations by energetic particles. *J. Geophys. Res. 96*, 1503–1512.

Chen, L., W. Li, J. Bortnik, and R. M. Thorne (2012). Amplification of whistler-mode hiss inside the plasmasphere. *Geophysical Research Letters 39*(8).

Chen, L., O. Santolík, M. Hajoš, L. Zheng, Z. Zhima, R. Heelis, M. Hanzelka, R. B. Horne, and M. Parrot (2017). Source of the low-altitude hiss in the ionosphere. *Geophysical Research Letters 44*(5), 2060–2069.

Chen, L., R. Thorne, V. Jordanova, C.-P. Wang, M. Gkioulidou, L. Lyons, and R. Horne (2010). Global simulation of EMIC wave excitation during the 21 April 2001 storm from coupled RCM-RAM-HOTRAY modeling. *Journal of Geophysical Research (Space Physics) 115*, A07209.

Chen, L., R. M. Thorne, J. Bortnik, W. Li, R. B. Horne, G. D. Reeves, C. A. Kletzing, W. S. Kurth, G. B. Hospodarsky, H. E. Spence, J. B. Blake, and J. F. Fennell (2014). Generation of unusually low frequency plasmaspheric hiss. *Geophysical Research Letters 41*(16), 5702–5709.

Cheng, C. (1992). Magnetospheric equilibrium with anisotropic pressure. *J. Geophys. Res. 97*, 1497–1510.

Cheng, C. and C. Lin (1987). Eigenmode analysis of compressional waves in the magnetosphere. *J. Geophys. Res. 14*, 884–887.

Cheremnykh, O., D. Klimushkin, and D. Kostarev (2014). On the structure of azimuthally small-scale ULF oscillations of hot space plasma in a curved magnetic field. Modes with continuous spectrum. *Kinematics and Physics of Celestial Bodies 30*, 209–222.

Cheremnykh, O., D. Klimushkin, and P. Mager (2016). On the structure of azimuthally small-scale ulf oscillations of a hot space plasma in a curved magnetic field: Modes with discrete spectra. *Kinematics and Physics of Celestial Bodies 32*, 120–128.

Chum, J. and O. Santolík (2005). Propagation of whistler-mode chorus to low altitudes: divergent ray trajectories and ground accessibility. *Annales Geophysicae 23*(12), 3727–3738.

Claudepierre, S. and Others (2013). Van Allen Probes observation of localized drift resonance between poloidal mode ultra-low frequency waves and 60 keV electrons. *Geophys. Res. Lett. 40*, 4491–4497.

Contel, O. L., A. Retinò, H. Breuillard, L. Mirioni, P. Robert, A. Chasapis, B. Lavraud, T. Chust, L. Rezeau, F. D. Wilder, D. B. Graham, M. R. Argall, D. J. Gershman, P.-A. Lindqvist, Y. V. Khotyaintsev, G. Marklund, R. E. Ergun, K. A. Goodrich, J. L. Burch, R. B. Torbert, J. Needell, M. Chutter, D. Rau, I. Dors, C. T. Russell, W. Magnes, R. J. Strangeway, K. R. Bromund, H. K. Leinweber, F. Plaschke, D. Fischer, B. J. Anderson, G. Le, T. E. Moore, C. J. Pollock, B. L. Giles, J. C. Dorelli, L. Avanov, and Y. Saito (2016). Whistler mode waves and hall fields detected by mms during a dayside magnetopause crossing. *Geophysical Research Letters 43*(12), 5943–5952.

Cully, C. M., R. E. Ergun, K. Stevens, A. Nammari, and J. Westfall (2008). The themis digital fields board. *Space Science Reviews 141*(1), 343–355.

Cummings, W., R. O'Sullivan, and P. Coleman Jr. (1969). Standing Alfvén waves in the magnetosphere. *J. Geophys. Res. 74*, 778.

Dai, L. and Others (2013). Excitation of poloidal standing Alfvén waves through drift resonance wave-particle interaction. *J. Geophys. Res. 40*, 4127–4132.

Dai, L. and Others (2015). Storm time occurrence and spatial distribution of Pc4 poloidal ULF waves in the inner magnetosphere: A Van Allen Probes statistical study. *J. Geophys. Res. 120*, 4748–4762.

Davidson, G. T. (1990). Pitch-angle diffusion and the origin of temporal and spatial structures in morningside aurorae. *Space Science Reviews 53*(1), 45–82.

De Michelis, P., I. A. Daglis, and G. Consolini (1999). An average image of proton plasma pressure and of current systems in the equatorial plane derived from AMPTE/CCE-CHEM measurements. *Journal of Geophysical Research: Space Physics 104*(A12), 28615–28624.

Dunckel, N. and R. Helliwell (1969). Whistler-mode emissions on the OGO 1 satellite. *J. Geophys. Res. 74*, 6371–6385.

Dungey, J. (1963). Hydromagnetic Waves. In C. DeWitt, J. Hieblot, and A. Lebeau (Eds.), *Geophysics the Earth's Environment*, pp. 537. New York: Gordon and Breach, Science Publisher.

Dungey, J. W. (1961). Interplanetary magnetic field and the auroral zones. *Phys. Rev. Lett. 6*, 47–48.

Elkington, S. R., M. K. Hudson, and A. A. Chan (1999). Acceleration of relativistic electrons via drift-resonant interaction with toroidal-mode Pc-5 ULF oscillations. *Geophysical Research Letters 26*(21), 3273–3276.

Fu, X., M. M. Cowee, R. H. Friedel, H. O. Funsten, S. P. Gary, G. B. Hospodarsky, C. Kletzing, W. Kurth, B. A. Larsen, K. Liu, E. A. MacDonald, K. Min, G. D. Reeves, R. M. Skoug, and D. Winske (2014). Whistler anisotropy instabilities as the source of banded chorus: Van allen probes observations and particle-in-cell simulations. *Journal of Geophysical Research: Space Physics 119*(10), 8288–8298.

Fukushima, N. and Y. Kamide (1973). Partial ring current models for worldwide geomagnetic disturbances. *Reviews of Geophysics and Space Physics 11*, 795–853.

Funsten, H. and Others (2013). Helium, Oxygen, Proton, and Electron (HOPE) Mass Spectrometer for the Radiation Belt Storm Probes Mission. *Space Science Reviews 179*, 423–484.

Gao, X., W. Li, R. M. Thorne, J. Bortnik, V. Angelopoulos, Q. Lu, X. Tao, and S. Wang (2014). New evidence for generation mechanisms of discrete and hiss-like whistler mode waves. *Geophysical Research Letters 41*(14), 4805–4811.

Godinez, H. C., Y. Yu, E. Lawrence, M. G. Henderson, B. Larsen, and V. K. Jordanova (2016). Ring current pressure estimation with RAM-SCB using data assimilation and Van Allen Probe flux data. *Geophysical Research Letters 43*(23), 11,911–948,956.

Golden, D. I., M. Spasojevic, and U. S. Inan (2011). Determination of solar cycle variations of midlatitude ELF/VLF chorus and hiss via automated signal detection. *Journal of Geophysical Research: Space Physics 116*(A3).

Golden, D. I., M. Spasojevic, W. Li, and Y. Nishimura (2012). Statistical modeling of plasmaspheric hiss amplitude using solar wind measurements and geomagnetic indices. *Geophysical Research Letters 39*(6).

Goldstein, J., S. G. Kanekal, D. N. Baker, and B. R. Sandel (2005). Dynamic relationship between the outer radiation belt and the plasmapause during marchmay 2001. *Geophysical Research Letters 32*(15).

Green, J. L., S. Boardsen, L. Garcia, W. W. L. Taylor, S. F. Fung, and B. W. Reinisch (2005). On the origin of whistler mode radiation in the plasmasphere. *Journal of Geophysical Research: Space Physics 110*(A3).

Hao, Y. X., Q.-G. Zong, Y. F. Wang, X.-Z. Zhou, H. Zhang, S. Y. Fu, Z. Y. Pu, H. E. Spence, J. B. Blake, J. Bonnell, J. R. Wygant, and C. A. Kletzing (2014). Interactions of energetic electrons with ulf waves triggered by interplanetary shock: Van allen probes observations in the magnetotail. *Journal of Geophysical Research: Space Physics 119*(10), 8262–8273.

Hartley, D. P., C. A. Kletzing, O. Santolík, L. Chen, and R. B. Horne (2018). Statistical Properties of Plasmaspheric Hiss From Van Allen Probes Observations. *Journal of Geophysical Research: Space Physics 123*(4), 2605–2619.

Hasegawa, A. (1969). Drift mirror instability of the magnetosphere. *Physics of Fluids 12*, 2642–2650.

He, Z., L. Chen, H. Zhu, Z. Xia, G. Reeves, Y. Xiong, L. Xie, and Y. Cao (2017). Multiple-Satellite Observation of Magnetic Dip Event During the Substorm on 10 October 2013. *Geophys. Res. Lett. 44*, 9167–9175.

Horne, R. and Others (2005). Timescale for radiation belt electron acceleration by whistler mode chorus waves. *J. Geophys. Res. 110*, 3225.

Horne, R. B. (1989). Path-integrated growth of electrostatic waves: The generation of terrestrial myriametric radiation. *Journal of Geophysical Research: Space Physics 94*(A7), 8895–8909.

Horne, R. B. and R. M. Thorne (1998). Potential waves for relativistic electron scattering and stochastic acceleration during magnetic storms. *Geophysical Research Letters 25*(15), 3011–3014.

Horne, R. B., R. M. Thorne, N. P. Meredith, and R. R. Anderson (2003). Diffuse auroral electron scattering by electron cyclotron harmonic and whistler mode waves during an isolated substorm. *Journal of Geophysical Research: Space Physics 108*(A7).

Hughes, W. (1994). Magnetospheric ULF Waves: A Tutorial With a Historical Perspective. In M. Engebretson, K. Takahashi, and M. Scholer (Eds.), *Solar Wind Sources of Magnetospheric Ultra-Low-Frequency Waves*, pp. 1.

Hughes, W. J. and D. J. Southwood (1976). The screening of micropulsation signals by the atmosphere and ionosphere. *Journal of Geophysical Research (1896-1977) 81*(19), 3234–3240.

Imajo, S., M. Nosé, A. Matsuoka, S. Kasahara, S. Yokota, M. Teramoto, K. Keika, T. Motoba, B. Anderson, R. Nomura, A. Fujimoto, I. Shinohara, and Y. Miyoshi (2018). Magnetosphere-Ionosphere Connection of Storm-Time Region-2 Field-Aligned Current and Ring Current: Arase and AMPERE Observations. *Journal of Geophysical Research: Space Physics 123*(11), 9545–9559.

Jaynes, A. and Others (2015). Correlated Pc4-5 ULF waves, whistler-mode chorus, and pulsating aurora observed by the Van Allen Probes and ground-based systems. *J. Geophys. Res. 120*, 8749–8761.

Jaynes, A. N., M. R. Lessard, J. V. Rodriguez, E. Donovan, T. M. Loto'aniu, and K. Rychert (2013). Pulsating auroral electron flux modulations in the equatorial magnetosphere. *Journal of Geophysical Research: Space Physics 118*(8), 4884–4894.

Jordanova, V., S. Zaharia, and D. Welling (2010). Comparative study of ring current development using empirical, dipolar, and self-consistent magnetic field simulations. *Journal of Geophysical Research (Space Physics) 115*, A00J11.

Katoh, Y. (2014). A simulation study of the propagation of whistler-mode chorus in the Earth's inner magnetosphere. *Earth, Planets, and Space 66*, 6.

Katoh, Y. and Y. Omura (2011). Amplitude dependence of frequency sweep rates of whistler mode chorus emissions. *J. Geophys. Res. 116*, A07201.

Kennel, C. (1966). Low-Frequency Whistler Mode. *Physics of Fluids 9*, 2190–2202.

Kennel, C. and H. Petschek (1966). Limit on Stably Trapped Particle Fluxes. *J. Geophys. Res. 71*, 1.

Kessel, R. (2008). Solar wind excitation of Pc5 fluctuations in the magnetosphere and on the ground. *J. Geophys. Res. 113*, 4202.

Kim, K.-C., D.-Y. Lee, and Y. Shprits (2015). Dependence of plasmaspheric hiss on solar wind parameters and geomagnetic activity and modeling of its global distribution. *Journal of Geophysical Research: Space Physics 120*(2), 1153–1167.

Kimura, I. (1974). Interrelation between vlf and ulf emissions. *Space Science Reviews 16*(3), 389–411.

Kletzing, C. and Others (2013). The Electric and Magnetic Field Instrument Suite and Integrated Science (EMFISIS) on RBSP. *Space Science Reviews 179*, 127–181.

Klimushkin, D. and P. Mager (2015). The Alfvén mode gyrokinetic equation in finite-pressure magnetospheric plasma. *Journal of Geophysical Research (Space Physics) 120*, 4465–4474.

Koons, H. and J. Roeder (1990). A survey of equatorial magnetospheric wave activity between 5 and 8 R(E). *Planetary and Space Science 38*, 1335–1341.

Lauben, D. and Others (2002). Source characteristics of ELF/VLF chorus. *J. Geophys. Res. 107*, 1429.

Le Contel, O., A. Roux, P. Robert, C. Coillot, A. Bouabdellah, B. de la Porte, D. Alison, S. Ruocco, V. Angelopoulos, K. Bromund, C. C. Chaston, C. Cully, H. U. Auster, K. H. Glassmeier, W. Baumjohann, C. W. Carlson, J. P. McFadden, and D. Larson (2008). First results of the themis search coil magnetometers. *Space Science Reviews 141*(1), 509–534.

LeDocq, M., D. Gurnett, and G. Hospodarsky (1998). Chorus Source Locations from VLF Poynting Flux Measurements with the Polar Spacecraft. *Geophys. Res. Lett. 25*, 4063.

Li, L., X.-Z. Zhou, Q.-G. Zong, R. Rankin, H. Zou, Y. Liu, X.-R. Chen, and Y.-X. Hao (2017). Charged particle behavior in localized ultralow frequency waves: Theory and observations. *Geophysical Research Letters 44*(12), 5900–5908.

Li, W., J. Bortnik, R. M. Thorne, and V. Angelopoulos (2011c). Global distribution of wave amplitudes and wave normal angles of chorus waves using themis wave observations. *Journal of Geophysical Research: Space Physics 116*(A12).

Li, W., J. Bortnik, R. M. Thorne, Y. Nishimura, V. Angelopoulos, and L. Chen (2011b). Modulation of whistler mode chorus waves: 2. role of density variations. *Journal of Geophysical Research: Space Physics 116*(A6).

Li, W., L. Chen, J. Bortnik, R. M. Thorne, V. Angelopoulos, C. A. Kletzing, W. S. Kurth, and G. B. Hospodarsky (2015a). First evidence for chorus at a large geocentric distance as a source of plasmaspheric hiss: Coordinated THEMIS and Van Allen Probes observation. *Geophysical Research Letters 42*(2), 241–248.

Li, W., Q. Ma, R. M. Thorne, J. Bortnik, C. A. Kletzing, W. S. Kurth, G. B. Hospodarsky, and Y. Nishimura (2015b). Statistical properties of plasmaspheric hiss derived from Van Allen Probes data and their effects on radiation belt electron dynamics. *Journal of Geophysical Research: Space Physics 120*(5), 3393–3405.

Li, W. and Others (2009). Evaluation of whistler-mode chorus intensification on the nightside during an injection event observed on the THEMIS spacecraft. *J. Geophys. Res. 114*, 0.

Li, W. and Others (2010). THEMIS analysis of observed equatorial electron distributions responsible for the chorus excitation. *J. Geophys. Res. 115*, 0.

Li, W., Y. Y. Shprits, and R. M. Thorne (2007). Dynamic evolution of energetic outer zone electrons due to wave-particle interactions during storms. *Journal of Geophysical Research: Space Physics 112*(A10).

Li, W., R. M. Thorne, J. Bortnik, Y. Nishimura, and V. Angelopoulos (2011a). Modulation of whistler mode chorus waves: 1. role of compressional pc4-5 pulsations. *Journal of Geophysical Research: Space Physics 116*(A6).

Li, W., R. M. Thorne, J. Bortnik, G. D. Reeves, C. A. Kletzing, W. S. Kurth, G. B. Hospodarsky, H. E. Spence, J. B. Blake, J. F. Fennell, S. G. Claudepierre, J. R. Wygant, and S. A. Thaller (2013). An unusual enhancement of low-frequency plasmaspheric hiss in the outer plasmasphere associated with substorm-injected electrons. *Geophysical Research Letters 40*(15), 3798–3803.

Li, W., R. M. Thorne, N. P. Meredith, R. B. Horne, J. Bortnik, Y. Y. Shprits, and B. Ni (2008). Evaluation of whistler mode chorus amplification during an injection event observed on crres. *Journal of Geophysical Research: Space Physics 113*(A9).

Li, X., D. N. Baker, T. P. O'Brien, L. Xie, and Q. G. Zong (2006). Correlation between the inner edge of outer radiation belt electrons and the innermost plasmapause location. *Geophysical Research Letters 33*(14).

Liu, H., Q.-G. Zong, X.-Z. Zhou, S. Fu, R. Rankin, L.-H. Wang, C. Yuan, Y. Wang, D. Baker, J. Blake, and C. Kletzing (2016). Compressional ULF wave modulation of energetic particles in the inner magnetosphere. *Journal of Geophysical Research (Space Physics) 121*, 6262–6276.

Lorentzen, K. R., J. B. Blake, U. S. Inan, and J. Bortnik (2001). Observations of relativistic electron microbursts in association with vlf chorus. *Journal of Geophysical Research: Space Physics 106*(A4), 6017–6027.

Lyons, L. and Others (2005). Solar wind-magnetosphere coupling leading to relativistic electron energization during high-speed streams. *J. Geophys. Res. 110*, 11202.

Lyons, L. R. and R. M. Thorne (1973). Equilibrium structure of radiation belt electrons. *Journal of Geophysical Research (1896-1977) 78*(13), 2142–2149.

Manninen, J., N. Kleimenova, O. Kozyreva, and T. Turunen (2010). Pc5 geomagnetic pulsations, pulsating particle precipitation, and VLF chorus: Case study on 24 November 2006. *J. Geophys. Res. 115*, 0.

Mauk, B. and Others (2013). Science Objectives and Rationale for the Radiation Belt Storm Probes Mission. *Space Science Reviews 179*, 3–27.

McPherron, R. L. (1995). Magnetospheric dynamics. In M. G. Kivelson and C. T. Russell (Eds.), *Introduction to Space Physics*. Cambridge.

Meredith, N., R. Horne, and R. Anderson (2001). Substorm dependence of chorus amplitudes: Implications for the acceleration of electrons to relativistic energies. *J. Geophys. Res. 106*, 13165–13178.

Meredith, N. and Others (2003a). Evidence for chorus-driven electron acceleration to relativistic energies from a survey of geomagnetically disturbed periods. *J. Geophys. Res. 108*, 1248.

Meredith, N. and Others (2003b). Favored regions for chorus-driven electron acceleration to relativistic energies in the Earth's outer radiation belt. *Geophys. Res. Lett. 30*, 1871.

Meredith, N. P., R. B. Horne, J. Bortnik, R. M. Thorne, L. Chen, W. Li, and A. Sicard-Piet (2013). Global statistical evidence for chorus as the embryonic source of plasmaspheric hiss. *Geophysical Research Letters 40*(12), 2891–2896.

Meredith, N. P., R. B. Horne, M. A. Clilverd, D. Horsfall, R. M. Thorne, and R. R. Anderson (2006). Origins of plasmaspheric hiss. *Journal of Geophysical Research: Space Physics 111*(A9).

Meredith, N. P., R. B. Horne, R. H. A. Iles, R. M. Thorne, D. Heynderickx, and R. R. Anderson (2002). Outer zone relativistic electron acceleration associated with substorm-enhanced whistler mode chorus. *Journal of Geophysical Research: Space Physics 107*(A7), SMP 29–1–SMP 29–14.

Meredith, N. P., R. B. Horne, A. Sicard-Piet, D. Boscher, K. H. Yearby, W. Li, and R. M. Thorne (2012). Global model of lower band and upper band chorus from multiple satellite observations. *Journal of Geophysical Research: Space Physics 117*(A10).

Meredith, N. P., R. B. Horne, R. M. Thorne, D. Summers, and R. R. Anderson (2004). Substorm dependence of plasmaspheric hiss. *Journal of Geophysical Research: Space Physics 109*(A6).

Min, K., K. Takahashi, A. Y. Ukhorskiy, J. W. Manweiler, H. E. Spence, J. Singer Howard, S. G. Claudepierre, B. A. Larsen, A. R. Soto-Chavez, and R. J. Cohen (2017). Second harmonic poloidal waves observed by Van Allen Probes in the dusk-midnight sector. *Journal of Geophysical Research: Space Physics*, n/a—-n/a.

Miyoshi, Y., Y. Katoh, T. Nishiyama, T. Sakanoi, K. Asamura, and M. Hirahara (2010). Time of flight analysis of pulsating aurora electrons, considering wave-particle interactions with propagating whistler mode waves. *Journal of Geophysical Research: Space Physics 115*(A10).

Miyoshi, Y. and Others (2003). Rebuilding process of the outer radiation belt during the 3 November 1993 magnetic storm: NOAA and Exos-D observations. *J. Geophys. Res. 108*, 1004.

Nakamura, S., Y. Omura, D. Summers, and C. A. Kletzing (2016). Observational evidence of the nonlinear wave growth theory of plasmaspheric hiss. *Geophysical Research Letters 43*(19), 10,10–40,49.

Ni, B., R. M. Thorne, Y. Y. Shprits, and J. Bortnik (2008). Resonant scattering of plasma sheet electrons by whistler-mode chorus: Contribution to diffuse auroral precipitation. *Geophysical Research Letters 35*(11).

Nishimura, Y., J. Bortnik, W. Li, R. M. Thorne, L. Chen, L. R. Lyons, V. Angelopoulos, S. B. Mende, J. Bonnell, O. Le Contel, C. Cully, R. Ergun, and U. Auster (2011). Multievent study of the correlation between pulsating aurora and whistler mode chorus emissions. *Journal of Geophysical Research: Space Physics 116*(A11), n/a—-n/a.

Nishimura, Y., J. Bortnik, W. Li, R. M. Thorne, L. R. Lyons, V. Angelopoulos, S. B. Mende, J. W. Bonnell, O. Le Contel, C. Cully, R. Ergun, and U. Auster (2010). Identifying the driver of pulsating aurora. *Science 330*(6000), 81–84.

Northrop, T. G. (1963). Adiabatic charged-particle motion. *Reviews of Geophysics 1*(3), 283–304.

O'Brien, T. P., M. D. Looper, and J. B. Blake (2004). Quantification of relativistic electron microburst losses during the gem storms. *Geophysical Research Letters 31*(4).

Okpala, K. C. and C. E. Ogbonna (2018). On the mid-latitude ionospheric storm association with intense geomagnetic storms. *Advances in Space Research 61*(7), 1858 – 1872. Studies on Mesosphere, Thermosphere and Ionosphere from Equatorial to Mid Latitudes - Recent Investigations and Improvements - Part 2.

Omura, Y., S. Nakamura, C. A. Kletzing, D. Summers, and M. Hikishima (2015). Nonlinear wave growth theory of coherent hiss emissions in the plasmasphere. *Journal of Geophysical Research: Space Physics 120*(9), 7642–7657.

Parks, G. K., B. Mauk, C. Gurgiolo, and C. S. Lin (1980). Observations of plasma injection. In S.-I. Akasofu (Ed.), *Dynamics of the Magnetosphere*, Dordrecht, pp. 371–383. Springer Netherlands.

Parrot, M., D. Benoist, J. Berthelier, J. Błęcki, Y. Chapuis, F. Colin, F. Elie, P. Fergeau, D. Lagoutte, F. Lefeuvre, C. Legendre, M. Lévêque, J. Pinçon, B. Poirier, H.-C. Seran, and P. Zamora (2006). The magnetic field experiment IMSC and its data processing onboard DEMETER: Scientific objectives, description and first results. *Planetary and Space Science 54*(5), 441–455.

Pavón-Carrasco, F. J. and A. De Santis (2016). The south atlantic anomaly: The key for a possible geomagnetic reversal. *Frontiers in Earth Science 4*, 40.

Pierrard, V. and S. Benck (2012). The dynamics of the terrestrial radiation belts and its links to the plasmasphere. *AIP Conference Proceedings 1500*(1), 216–221.

Rankin, R., K. Kabin, and R. Marchand (2006). Alfvénic field line resonances in arbitrary magnetic field topology. *Advances in Space Research 38*, 1720–1729.

Regi, M. (2016). ULF power fluctuations in the solar-wind parameters and their relationship with the relativistic electron flux at the geosynchronous orbit. *Nuovo Cimento C Geophysics Space Physics C 39*, 285.

Remya, B., D. G. Sibeck, A. J. Halford, K. R. Murphy, G. D. Reeves, H. J. Singer, J. R. Wygant, G. Farinas Perez, and S. A. Thaller (2018). Ion Injection Triggered EMIC Waves in the Earth's Magnetosphere. *Journal of Geophysical Research: Space Physics 123*(6), 4921–4938.

Ren, J., Q. Zong, X. Zhou, R. Rankin, and Y. Wang (2016). Interaction of ULF waves with different ion species: Pitch angle and phase space density implications. *Journal of Geophysical Research (Space Physics) 121*, 9459–9472.

Rostoker, G. (1996). Phenomenology and physics of magnetospheric substorms. *Journal of Geophysical Research: Space Physics 101*(A6), 12955–12973.

Rostoker, G., S.-I. Akasofu, J. Foster, R. Greenwald, Y. Kamide, K. Kawasaki, A. Lui, R. McPherron, and C. Russell (1980). Magnetospheric substormsdefinition and signatures. *Journal of Geophysical Research: Space Physics 85*(A4), 1663–1668.

Roux, A., O. L Contel, C. Coillot, A. Bouabdellah, B. de la Porte, D. Alison, S. Ruocco, and M. C. Vassal (2008). The search coil magnetometer for themis. *Space Science Reviews 141*(1), 265–275.

Russell, C. T., R. E. Holzer, and E. J. Smith (1969). OGO 3 observations of ELF noise in the magnetosphere: 1. Spatial extent and frequency of occurrence. *Journal of Geophysical Research 74*(3), 755–777.

Sandholt, P. E. and C. J. Farrugia (2001). Multipoint observations of substorm intensifications: The high-latitude aurora and electron injections in the inner equatorial plasma sheet. *Geophysical Research Letters 28*(3), 483–486.

Santolík, O. (2008). New results of investigations of whistler-mode chorus emissions. *Nonlinear Processes in Geophysics 15*, 621–630.

Santolík, O., J. Chum, M. Parrot, D. A. Gurnett, J. S. Pickett, and N. Cornilleau-Wehrlin (2006a). Propagation of whistler mode chorus to low altitudes: Spacecraft observations of structured ELF hiss. *Journal of Geophysical Research: Space Physics 111*(A10).

Santolík, O., D. A. Gurnett, J. S. Pickett, M. Parrot, and N. Cornilleau-Wehrlin (2003a). Spatio-temporal structure of storm-time chorus. *Journal of Geophysical Research: Space Physics 108*(A7).

Santolík, O., F. Němec, M. Parrot, D. Lagoutte, L. Madrias, and J. J. Berthelier (2006b). Analysis methods for multi-component wave measurements on board the DEMETER spacecraft. *Planetary and Space Science 54*(5), 512–527.

Santolík, O. and M. Parrot (1999). Case studies on the wave propagation and polarization of ELF emissions observed by Freja around the local proton gyrofrequency. *Journal of Geophysical Research: Space Physics 104*(A2), 2459–2475.

Santolík, O. and M. Parrot (2000). Application of wave distribution function methods to an ELF hiss event at high latitudes. *Journal of Geophysical Research: Space Physics 105*(A8), 18885–18894.

Santolík, O., M. Parrot, and F. Lefeuvre (2003b). Singular value decomposition methods for wave propagation analysis. *Radio Science 38*(1).

Santolík, O., J. S. Pickett, D. A. Gurnett, J. D. Menietti, B. T. Tsurutani, and O. Verkhoglyadova (2010). Survey of Poynting flux of whistler mode chorus in the outer zone. *Journal of Geophysical Research: Space Physics 115*(A7).

Sato, N. and H. Fukunishi (1981). Interaction between elf-vlf emissions and magnetic pulsations: Classification of quasi-periodic elf-vlf emissions based on frequency-time spectra. *Journal of Geophysical Research: Space Physics 86*(A1), 19–29.

Sato, N., K. Hayashi, S. Kokubun, T. Oguti, and H. Fukunishi (1974). Relationships between quasi-periodic vlf emission and geomagnetic pulsation. *Journal of Atmospheric and Terrestrial Physics 36*(9), 1515 – 1526.

Selesnick, R. S., M. D. Looper, and R. A. Mewaldt (2007). A theoretical model of the inner proton radiation belt. *Space Weather 5*(4).

Shi, R., W. Li, Q. Ma, S. G. Claudepierre, C. A. Kletzing, W. S. Kurth, G. B. Hospodarsky, H. E. Spence, G. D. Reeves, J. F. Fennell, J. B. Blake, S. A. Thaller, and J. R. Wygant (2018). Van allen probes observation of plasmaspheric hiss modulated by injected energetic electrons. *Annales Geophysicae 36*(3), 781–791.

Sibeck, D. G. and V. Angelopoulos (2008). Themis science objectives and mission phases. *Space Science Reviews 141*(1), 35–59.

Smith, E. J., A. M. A. Frandsen, B. T. Tsurutani, R. M. Thorne, and K. W. Chan (1974). Plasmaspheric hiss intensity variations during magnetic storms. *Journal of Geophysical Research (1896-1977) 79*(16), 2507–2510.

Sonwalkar, V. and U. Inan (1989). Lightning as an embryonic source of VLF hiss. *J. Geophys. Res. 94*, 6986–6994.

Southwood, D. (1976). A general approach to low-frequency instability in the ring current plasma. *J. Geophys. Res. 81*, 3340–3348.

Spence, H. and Others (2013). Science Goals and Overview of the Radiation Belt Storm Probes (RBSP) Energetic Particle, Composition, and Thermal Plasma (ECT) Suite on NASA's Van Allen Probes Mission. *Space Science Reviews 179*, 311–336.

Summers, D., C. Ma, N. P. Meredith, R. B. Horne, R. M. Thorne, D. Heynderickx, and R. R. Anderson (2002). Model of the energization of outer-zone electrons by whistler-mode chorus during the october 9, 1990 geomagnetic storm. *Geophysical Research Letters 29*(24), 27–1–27–4.

Summers, D., B. Ni, N. P. Meredith, R. B. Horne, R. M. Thorne, M. B. Moldwin, and R. R. Anderson (2008). Electron scattering by whistler-mode ELF hiss in plasmaspheric plumes. *Journal of Geophysical Research: Space Physics 113*(A4).

Takahashi, K. (1988). Multisatellite studies of ULF waves. *Advances in Space Research 8*, 427–436.

Takahashi, K. and A. Ukhorskiy (2007). Solar wind control of Pc5 pulsation power at geosynchronous orbit. *J. Geophys. Res. 112*, 11205.

Tao, X. (2014). A numerical study of chorus generation and the related variation of wave intensity using the DAWN code. *J. Geophys. Res. 119*, 3362–3372.

Tenerani, A., O. Le Contel, F. Califano, P. Robert, D. Fontaine, N. Cornilleau-Wehrlin, and J.-A. Sauvaud (2013). Cluster observations of whistler waves correlated with ion-scale magnetic structures during the 17 August 2003 substorm event. *Journal of Geophysical Research (Space Physics) 118*, 6072–6089.

Thorne, R., B. Ni, X. Tao, R. Horne, and N. Meredith (2010). Scattering by chorus waves as the dominant cause of diffuse auroral precipitation. *Nature 467*, 943–946.

Thorne, R. M., E. J. Smith, R. K. Burton, and R. E. Holzer (1973). Plasmaspheric hiss. *Journal of Geophysical Research 78*(10), 1581–1596.

Tixier, M. and N. Cornilleau-Wehrlin (1986). How are the VLF quasi-periodic emissions controlled by harmonics of field line oscillations? - The results of a comparison between ground and GEOS satellites measurements. *J. Geophys. Res. 91*, 6899–6919.

Tsurutani, B. and E. Smith (1974). Postmidnight chorus: A substorm phenomenon. *J. Geophys. Res. 79*, 118–127.

Tsurutani, B. and E. Smith (1977). Two types of magnetospheric ELF chorus and their substorm dependences. *J. Geophys. Res. 82*, 5112–5128.

Tsurutani, B., O. Verkhoglyadova, G. Lakhina, and S. Yagitani (2009). Properties of dayside outer zone chorus during HILDCAA events: Loss of energetic electrons. *Journal of Geophysical Research (Space Physics) 114*, A03207.

Tsyganenko, N. (1995). Modeling the Earth's magnetospheric magnetic field confined within a realistic magnetopause. *J. Geophys. Res. 100*, 5599–5612.

Tsyganenko, N. (2000). Modeling the inner magnetosphere: The asymmetric ring current and Region 2 Birkeland currents revisited. *J. Geophys. Res. 105*, 27739–27754.

Tsyganenko, N. and M. Peredo (1994). Analytical models of the magnetic field of disk-shaped current sheets. *J. Geophys. Res. 99*, 199–205.

Tsyganenko, N. and M. Sitnov (2005). Modeling the dynamics of the inner magnetosphere during strong geomagnetic storms. *Journal of Geophysical Research (Space Physics) 110*, A03208.

Tsyganenko, N. and D. Stern (1996). Modeling the global magnetic field of the large-scale Birkeland current systems. *J. Geophys. Res. 101*, 27187–27198.

Ukhorskiy, A., B. Anderson, P. Brandt, and N. Tsyganenko (2006). Storm time evolution of the outer radiation belt: Transport and losses. *Journal of Geophysical Research (Space Physics) 111*, A11S03.

University of Calgary Website. ABOVE an Array for Broadband Observations of VLF/ELF Emissions: Whistler-mode chorus. `https://www.ucalgary.ca/above/science/chorus`.

Wikipedia. South Atlantic Anomaly. `https://en.wikipedia.org/wiki/South_Atlantic_Anomaly`.

Wilder, F. D., R. E. Ergun, D. L. Newman, K. A. Goodrich, K. J. Trattner, M. V. Goldman, S. Eriksson, A. N. Jaynes, T. Leonard, D. M. Malaspina, N. Ahmadi, S. J. Schwartz, J. L. Burch, R. B. Torbert, M. R. Argall, B. L. Giles, T. D. Phan, O. Le Contel, D. B. Graham, Y. V. Khotyaintsev, R. J. Strangeway, C. T. Russell, W. Magnes, F. Plaschke, and P.-A. Lindqvist (2017). The nonlinear behavior of whistler waves at the reconnecting dayside magnetopause as observed by the magnetospheric multiscale mission: A case study. *Journal of Geophysical Research: Space Physics 122*(5), 5487–5501.

Wu, S., R. E. Denton, and W. Li (2013), Effects of cold electron density on the whistler anisotropy instability, *Journal of Geophysical Research: Space Physics*, *118*(2), 765–773, doi:10.1029/2012JA018402.

Wygant, J. and Others (2013). The Electric Field and Waves Instruments on the Radiation Belt Storm Probes Mission. *Space Science Reviews 179*, 183–220.

Xia, Z., L. Chen, L. Dai, S. G. Claudepierre, A. A. Chan, A. R. Soto-Chavez, and G. D. Reeves (2016). Modulation of chorus intensity by ULF waves deep in the inner magnetosphere. *Geophysical Research Letters 43*(18), 9444–9452.

Xia, Z., L. Chen, L. Zheng, and A. Chan (2017). Eigenmode analysis of compressional poloidal modes in a self-consistent magnetic field. *Journal of Geophysical Research (Space Physics) 122*(A11), 10.

Xiao, F. and X. Feng (2006). Modeling Density and Anisotropy of Energetic Electrons Along Magnetic Field Lines. *Plasma Science and Technology 8*, 279–284.

Xiong, Y., L. Chen, L. Xie, S. Fu, Z. Xia, and Z. Pu (2017). Relativistic electron's butterfly pitch angle distribution modulated by localized background magnetic field perturbation driven by hot ring current ions. *Geophys. Res. Lett. 44*, 4393–4400.

Yoo, J., J. Jara-Almonte, E. Yerger, S. Wang, T. Qian, A. Le, H. Ji, M. Yamada, W. Fox, E.-H. Kim, L.-J. Chen, and D. J. Gershman (2018). Whistler wave generation by anisotropic tail electrons during asymmetric magnetic reconnection in space and laboratory. *Geophysical Research Letters 45*(16), 8054–8061.

Young, S. L., R. E. Denton, B. J. Anderson, and M. K. Hudson (2002). Empirical model for scattering caused by field line curvature in a realistic magnetosphere. *Journal of Geophysical Research: Space Physics 107*(A6), SMP 3–1–SMP 3–9.

Yu, Y., V. Jordanova, S. Zaharia, J. Koller, J. Zhang, and L. Kistler (2012). Validation study of the magnetically self-consistent inner magnetosphere model RAM-SCB. *Journal of Geophysical Research (Space Physics) 117*, A03222.

Yue, C., C.-P. Wang, L. Lyons, J. Liang, E. Donovan, S. Zaharia, and M. Henderson (2014). Current sheet scattering and ion isotropic boundary under 3-D empirical force-balanced magnetic field. *Journal of Geophysical Research (Space Physics) 119*, 8202–8211.

Yue, C., C.-P. Wang, Y. Nishimura, K. Murphy, X. Xing, L. Lyons, M. Henderson, V. Angelopoulos, A. Lui, and T. Nagai (2015). Empirical modeling of 3-D force-balanced plasma and magnetic field structures during substorm growth phase. *Journal of Geophysical Research (Space Physics) 120*, 6496–6513.

Yue, C., C.-P. Wang, S. Zaharia, X. Xing, and L. Lyons (2013). Empirical modeling of plasma sheet pressure and three-dimensional force-balanced magnetospheric magnetic field structure: 2. Modeling. *Journal of Geophysical Research (Space Physics) 118*, 6166–6175.

Zaharia, S., C. Cheng, and K. Maezawa (2004). 3-D force-balanced magnetospheric configurations. *Annales Geophysicae 22*, 251–265.

Zaharia, S., V. Jordanova, M. Thomsen, and G. Reeves (2006). Self-consistent modeling of magnetic fields and plasmas in the inner magnetosphere: Application to a geomagnetic storm. *Journal of Geophysical Research (Space Physics) 111*, A11S14.

Zhang, Z., L. Chen, X. Li, Z. Xia, R. A. Heelis, and R. B. Horne (2018). Observed propagation route of vlf transmitter signals in the magnetosphere. *Journal of Geophysical Research: Space Physics 123*(7), 5528–5537.

Zhima, Z., J. Cao, H. Fu, W. Liu, L. Chen, M. Dunlop, X. Zhang, and X. Shen (2015). Whistler mode wave generation at the edges of a magnetic dip. *Journal of Geophysical Research (Space Physics) 120*, 2469–2476.

Zhima, Z., L. Chen, Y. Xiong, J. Cao, and H. Fu (2017). On the Origin of Ionospheric Hiss: A Conjugate Observation. *Journal of Geophysical Research: Space Physics 122*(11), 11,711–784,793.

Zhou, X.-Z., Z.-H. Wang, Q.-G. Zong, S. G. Claudepierre, I. R. Mann, M. G. Kivelson, V. Angelopoulos, Y.-X. Hao, Y.-F. Wang, and Z.-Y. Pu (2015). Imprints of impulse-excited hydromagnetic waves on electrons in the van allen radiation belts. *Geophysical Research Letters 42*(15), 6199–6204.

Zhou, X.-Z., Z.-H. Wang, Q.-G. Zong, R. Rankin, M. Kivelson, X.-R. Chen, J. Blake, J. Wygant, and C. Kletzing (2016). Charged particle behavior in the growth and damping stages of ultralow frequency waves: Theory and Van Allen Probes observations. *Journal of Geophysical Research (Space Physics) 121*, 3254–3263.

BIOGRAPHICAL SKETCH

Zhiyang Xia was born in Shandong, China. After attending Tianjin Nankai High School, Zhiyang Xia enrolled in the Geophysics program at the University of Science and Technology of China in 2006. In the summer of 2010, Zhiyang Xia received his Bachelor of Science degree and pursued his graduate program in space physics at the University of Science and Technology of China. He went to the National Space Science Center, Chinese Academy of Sciences in the summer of 2011 and obtained a Master of Science degree under the direction of Dr. Chi Wang in 2013. In the summer of 2014, he attended The University of Texas at Dallas to pursue his doctoral degree in Physics focusing on Space Sciences, obtaining his another master's degree in the fall of 2015 and his PhD in the summer of 2019 under the direction of Professor Lunjin Chen.

CURRICULUM VITAE

Zhiyang Xia

July 15, 2019

Contact Information:

Department of Physics
The University of Texas at Dallas
800 W. Campbell Rd.
Richardson, TX 75080-3021, U.S.A.
Phone: (469) 360-8774
Email: `Zhiyang.xia@utdallas.edu`

Educational History:

B.S., Geophysics, University of Science and Technology of China, 2010
M.S., Geophysics, University of Science and Technology of China, 2013
Ph.D., Physics, The University of Texas at Dallas, 2019

Modulation of very low frequency whistler waves by ultra low frequency waves
Ph.D. Dissertation
Physics Department, The University of Texas at Dallas
Advisors: Lunjin Chen

Academic Experience:

Research Assistant, The University of Texas at Dallas, June 2016 – present
Teaching Assistant, The University of Texas at Dallas, August 2014 – May 2016

Professional Recognitions and Honors:

Margie Renfrow Graduate Student Support Fund, Physics, UTD, 2018
William B. Hanson Graduate Student Support Fund, William B. Hanson Center for Space Sciences, UTD, 2017
Margie Renfrow Graduate Student Support Fund, Physics, UTD, 2016

Professional Memberships:

American Geophysical Union (AGU), 2016–present

Professional Publications:

Wang, C., **Xia, Z. Y.**, Peng, Z., and Lu, Q. M. (2013), **Estimating the open magnetic flux from the interplanetary and ionospheric conditions**, *J. Geophys. Res. Space Physics*, 118, 1899-1903, doi:10.1002/jgra.50255.

Chen, L., J. Sun, Q. Lu, X. Gao, **Z. Xia**, and Z. Zhima (2016), **Generation of magnetosonic waves over a continuous spectrum**, *Journal of Geophysical Research: Space Physics*, 121, 1137-1147, doi:10.1002/2015JA022089.

Xia, Z., L. Chen, L. Dai, S. G. Claudepierre, A. A. Chan, A. R. Soto-Chavez, and G. D. Reeves (2016), **Modulation of chorus intensity by ULF waves deep in the inner magnetosphere**, *Geophys. Res. Lett.*, 43, 9444-9452, doi:10.1002/2016GL070280.

Xiong, Y., L. Chen, L. Xie, S. Fu, **Z. Xia**, and Z. Pu (2017), **Relativistic electron's butterfly pitch angle distribution modulated by localized background magnetic field perturbation driven by hot ring current ions**, *Geophys. Res. Lett.*, 44, 4393-4400, doi:10.1002/2017GL072558.

Xia, Z., L. Chen, L. Zheng, and A. A. Chan (2017), **Eigenmode analysis of compressional poloidal modes in a self-consistent magnetic field**, *Journal of Geophysical Research: Space Physics*, 122, 1-13, doi:10.1002/2017JA024376.

He, Z., Chen, L., Zhu, H., **Xia, Z.**, Reeves, G. D., Xiong, Y., Xie, L. and Cao, Y. (2017), **Multiple-satellite observation of magnetic dip event during the substorm on 10 October, 2013**, *Geophysical Research Letters*, 44, 9167- 9175. https://doi.org/10.1002/2017GL074869.

Liu, X., Chen, L., Yang, L., **Xia, Z.**, and Malaspina, D. M. (2018). **One-dimensional full wave simulation of equatorial magnetosonic wave propagation in an inhomogeneous magnetosphere**. *Journal of Geophysical Research: Space Physics*, 123, 587-599. https://doi.org/10.1002/2017JA024336.

Zhang, Z., Chen, L., Li, X., **Xia, Z.**, Heelis, R. A., and Horne, R. B. (2018). **Observed propagation route of VLF transmitter signals in the magnetosphere**. *Journal of Geophysical Research: Space Physics*, 123, 5528-5537. doi:10.1029/2018JA025637.

Xia, Z., Chen, L., Artemyev, A. V., Zhu, H., Jordanova, V. K., and Zheng, L. (2019). **The effects of localized thermal pressure on equilibrium magnetic fields and particle drifts in the inner magnetosphere**. *Journal of Geophysical Research: Space Physics*, 124. https://doi.org/10.1029/2018JA026043.

A. R. Soto-Chavez, L. J. Lanzerotti, A. Gerrard,1 R. Cohen, J. W. Manweiler, **Z. Xia**, L.Chen, and H. Kim. (2019). **Observational evidence of the drift-mirror plasma instability in Earth's inner magnetosphere**. *Physics of Plasmas* 26(4), 042110. https://doi.org/10.1063/1.5083629.

Xia, Z., Chen, L., Zhima, Z., Santolík, O., Horne, R. B., and Parrot, M. (2019). **Statistical characteristics of ionospheric hiss waves**. *Geophysical Research Letters*, 46. https://doi.org/10.1029/2019GL083275.

Liu, S., **Xia, Z.**, Chen, L., Liu, Y., Liao, Z., and Zhu, H. (2019). **Magnetospheric Multiscale Observation of quasiperiodic EMIC waves associated with enhanced solar wind pressure**. *Geophysical Research Letters*, 46. https://doi.org/10.1029/2019GL083421.

Zeren Zhima, Jianping Huang, **Zhiyang Xia**, Lunjin Chen, Yanyan Yang, Mirko Piersanti, Wei Chu, Rui Yan, Shufan Zhao, Qiao Wang, Xuhui Shen. (2019). **Simultaneous observations of ELF/VLF rising-tone quasiperiodic waves, hiss waves and electron precipitations in the high-latitude ionosphere**. *Journal of Geophysical Research: Space Physics*. (under review).

Professional Presentations:

Modulation of magnetosonic wave intensity by thermal plasma density variation, *GEM Summer Workshop 2015*, Snowmass, CO, Jun., 2015. (poster)

Modulation of chorus intensity by ulf waves deep in the inner magnetosphere, *GEM Summer Workshop 2016*, Santa Fe, NM, Jun., 2016. (poster)

Modulation of chorus intensity by ulf waves deep in the inner magnetosphere, *AGU Fall Meeting 2016*, San Francisco, CA, Dec., 2016. (poster)

2017 GEM Workshop Student Day Tutorials: Global Magnetohydrodynamic Modeling of the Magnetosphere, *GEM Summer Workshop 2017*, Portsmouth, VA, Jun., 2017. (oral)

Eigenmode analysis of compressional poloidal modes in a self-consistent magnetic field, *GEM Summer Workshop 2017*, Portsmouth, VA, Jun., 2017. (oral)

The effects of localized thermal pressure on equilibrium magnetic fields and particle drifts, *GEM Summer Workshop 2018*, Santa Fe, NM, Jun., 2018. (poster)

Propagation characteristics of ionospheric hiss waves, *USNC-URSI National Radio Science Meeting 2019*, Boulder, CO, Jan., 2019. (oral)

Statistical Characteristics of Ionospheric Hiss Waves, *GEM Summer Workshop 2019*, Santa Fe, NM, Jun., 2019. (poster)